

INVESTIGATIONS OF NOISE AND OF QUANTUM  
INTERFERENCE IN PROXIMITY EFFECT BRIDGES

Thesis by  
Stephen K. Decker

In Partial Fulfillment of the Requirements  
for the Degree of  
Doctor of Philosophy

California Institute of Technology  
Pasadena, California

1975

(Submitted February 27, 1975)

To Sue without whose help and encouragement  
I would not have finished.

To Gretchen Marie, who somehow makes it all worthwhile.

## ACKNOWLEDGMENTS

The completion of this thesis would not have been possible without the aid, direct and indirect, of many people. A complete listing is impossible to give but the following are truly deserving of thanks.

Dr. James E. Mercereau, who has patiently labored to accomplish my scientific training.

Dr. Harris A. Notarys, who was a constant teacher and collaborator in every experimental technique, and who refuses to take any credit at all.

My colleagues-in-arms, the graduate students in the weak superconductivity group, those who have gone before and those who must remain behind: Randy Kirschman, Ming Lun Yu, Run Han Wang, Dave Palmer, Tom Ganz, Jim Franson, and Bob MacNamara.

Special thanks go to David Palmer and Harris Notarys for teaching me that low temperature physics is just a giant coherent ice cream state.

The excellent typing of this thesis was done by Mrs. Kathleen Ellison, who did much of it from manuscript in my less than legible hand.

To Bill Moore, who helped with the figures and in many other ways.

Finally I would like to thank IBM, for the patience and encouragement shown to me as this thesis was tardily completed.

## ABSTRACT

This work reports investigations upon weakly superconducting proximity effect bridges. These bridges, which exhibit the Josephson effects, are produced by bisecting a superconductor with a short ( $< 1\mu$ ) region of material whose superconducting transition temperature is below that of the adjacent superconductors. These bridges are fabricated from layered refractory metal thin films whose transition temperature will depend upon the thickness ratio of the materials involved. The thickness ratio is changed in the area of the bridge to lower its transition temperature. This is done through novel photolithographic techniques described in the text, Chapter 2.

If two such proximity effect bridges are connected in parallel, they form a quantum interferometer. The maximum zero voltage current through this circuit is periodically modulated by the magnetic flux through the circuit. At a constant bias current, the modulation of the critical current produces a modulation in the dc voltage across the bridge. This change in dc voltage has been found to be the result of a change in the internal dissipation in the device. A simple model using lumped circuit theory and treating the bridges as quantum oscillators of frequency  $\omega = 2eV/\hbar$ , where  $V$  is the time average voltage across the device, has been found to adequately describe the observed voltage modulation.

The quantum interferometers have been converted to a galvanometer through the inclusion of an integral thin film current path which

couples magnetic flux through the interferometer. Thus a change in signal current produces a change in the voltage across the interferometer at a constant bias current. This work is described in Chapter 3 of the text.

The sensitivity of any device incorporating proximity effect bridges will ultimately be determined by the fluctuations in their electrical parameters. We have measured the spectral power density of the voltage fluctuations in proximity effect bridges using a room temperature electronics and a liquid helium temperature transformer to match the very low ( $\sim 0.1 \Omega$ ) impedances characteristic of these devices.

We find the voltage noise to agree quite well with that predicted by phonon noise in the normal conduction through the bridge plus a contribution from the superconducting pair current through the bridge which is proportional to the ratios of this current to the time average voltage across the bridge. The total voltage fluctuations are given by  $\langle V^2(f) \rangle = 4kTR_d^2 I/V$  where  $R_d$  is the dynamic resistance,  $I$  the total current, and  $V$  the voltage across the bridge. An additional noise source appears with a strong  $1/f^n$  dependence,  $1.5 < n < 2$ , if the bridges are fabricated upon a glass substrate. This excess noise, attributed to thermodynamic temperature fluctuations in the volume of the bridge, increases dramatically on a glass substrate due to the greatly diminished thermal diffusivity of the glass as compared to sapphire.

## TABLE OF CONTENTS

	Page
ACKNOWLEDGMENTS	iii
ABSTRACT	iv
TABLE OF CONTENTS	vi
LIST OF FIGURES	ix
LIST OF TABLES	x
INTRODUCTION	1
Chapter 1 BACKGROUND INFORMATION	3
1.1 <u>Superconductivity and Macroscopic Quantum           Mechanics</u>	3
1.2 <u>The Josephson Effects</u>	8
1.3 <u>The Josephson Effects in Non-Tunneling           Structures</u>	11
1.4 <u>Phase Slip</u>	15
1.5 <u>Proximity Effect</u>	21
Chapter 2 FABRICATION OF PROXIMITY EFFECT BRIDGES	22
2.1 <u>Introduction</u>	22
2.2 <u>Fabrication of Layered Refractory Thin Films</u>	24
2.3 <u>Fabrication of Superconducting Circuits</u>	32
2.4 <u>Microscope Projection</u>	33
2.5 <u>Anodization</u>	40
2.6 <u>Example of Fabrication</u>	47
2.7 <u>Advantages and Limitations</u>	50

	Page
Chapter 3	
APPLICATIONS OF QUANTUM INTERFERENCE AT FINITE VOLTAGES	51
3.1 <u>Quantum Interference at Zero Voltage</u>	51
3.2 <u>Quantum Interference at Finite Voltages</u>	56
3.3 <u>The Relationship of Dissipation to Quantum         Interference at Finite Voltages</u>	61
3.4 <u>Experimental Evidence</u>	70
3.5 <u>Use of Quantum Interferometer as a         Galvanometer</u>	77
3.6 <u>Inclusion of the Quantum Galvanometer into         a Superconducting Transformer</u>	88
3.7 <u>Summary</u>	94
Chapter 4	
NOISE MEASUREMENTS IN PROXIMITY EFFECT BRIDGES	96
4.1 <u>Introduction</u>	96
4.2 <u>Background</u>	98
4.3 <u>Previous Analysis</u>	100
4.4 <u>Previous Experiments</u>	103
4.5 <u>Experimental Procedure</u>	105
4.6 <u>Noise Performance</u>	114
4.7 <u>External Noise and Interference</u>	117
4.8 <u>Measurements of Noise Density Spectrum</u>	121
4.9 <u>Discussion</u>	132
4.10 <u>Effect of Substrate</u>	153

	Page
4.11 <u>Summary</u>	157
Appendix A DERIVATION OF TRANSFER IMPEDANCE AND NOISE MIXING FOR A RESISTIVELY SHUNTED PROXIMITY EFFECT BRIDGE	159
REFERENCES	166

## LIST OF FIGURES

	Page
Chapter 1	
Figure 1-1	12
Chapter 2	
Figure 2-1	26
Figure 2-2	30
Figure 2-3	31
Figure 2-4	34
Figure 2-5	37
Figure 2-6	41
Figure 2-7	44
Chapter 3	
Figure 3-1	53
Figure 3-2	57
Figure 3-3	59
Figure 3-4	62
Figure 3-5	65
Figure 3-6	71
Figure 3-7	74
Figure 3-8	78
Figure 3-9	82
Figure 3-10	86
Figure 3-11	83
Figure 3-12	89

	Page
Figure 3-13	93
Chapter 4	
Figure 4-1	106
Figure 4-2	111
Figure 4-3	115
Figure 4-4	123
Figure 4-5	125
Figure 4-6	128
Figure 4-7	129
Figure 4-8	149
Figure 4-9	138
Figure 4-10	141
Figure 4-11	144
Figure 4-12	151
Figure 4-13	155
Appendix 1	
Figure A-1	160

## LIST OF TABLES

Chapter 2	
Table 2-1	25
Table 2-2	38

## INTRODUCTION

Superconductivity has received intense study for many years as a unique and exciting state of matter. As a result of these investigations, most of the equilibrium characteristics of superconductivity are well understood and can be described in terms of the collective motion of a macroscopic quantum state for electrons. More recent ramifications of the superconducting state, represented by the phenomena of the Josephson effect and time dependent superconductivity, have in the past few years been subjected to the same intense scrutiny. These studies are now leading to an improved understanding of the dynamic and nonequilibrium properties of superconductivity.

In this thesis, some of these dynamic properties of superconductivity have been used as the basis for developing certain quantum electronic circuits. In order to carry out this work, it has been necessary to develop reliable techniques for fabricating superconducting structures which exhibit quantum interference effects (herein called "proximity effect bridges"). These bridges, fabricated from a monolithic thin film of refractory materials, offer a realization of a superconducting quantum interference element which is more reliable, reproducible, and physically robust than any of the traditional devices exhibiting these Josephson effects. For this reason, the fabrication techniques we have developed for these bridges will be given in considerable detail. They have also been used extensively in studies on the physics of nonequilibrium superconductivity.

This thesis represents some of the first attempts to systematically examine and characterize superconducting quantum electronic circuits. For example, we have combined two such bridges in parallel to form a

quantum interferometer. By considering the bridges as quantum oscillators and taking into account the ac impedance of the superconducting paths connecting them, we have been able to examine the behavior of the interferometers over a wide frequency range. Typical dimensions for these circuits are on the order of  $5 \times 10^{-5}$  m.

The fluctuation of the electrical parameters of the proximity effect bridge will ultimately limit the sensitivity of any circuit incorporating the bridges. In this thesis, we have measured the noise fluctuations across such bridges in the frequency range 20 to 2000 Hz and find the expected Johnson noise plus a contribution arising from the transitions between superconducting pair states within the bridge. The total noise power density is given quite well by  $\langle V^2(f) \rangle = 4 kTR_d^2 \frac{I}{V}$ . The difference between this expression and the Johnson noise ( $4 kTR_d^2/R$ ) is just the excess noise from the pair current.

Most of the fabrication information in Chap. 2 has appeared in: David William Palmer and S. K. Decker, Rev. Sci. Instr. 44, 1621 (1973). The information contained in Chap. 3 on quantum interferometers appeared in: S. K. Decker and J. E. Mercereau, Appl. Phys. Letters 23, 347 (1973), and S. K. Decker and J. E. Mercereau, Bull. Am. Phys. Soc. 18, 1608 (1973). The noise measurements in Chap. 4 were presented at the Applied Superconductivity Conference, Oakbrook, Illinois, Sept. 30-Oct. 1, 1974, paper R4 which will appear in IEEE Mag. Trans. in March 1975. The measurements in Chap. 4 along with the discussion and analysis sections have been submitted to Appl. Phys. Letters for publication.

## Chapter 1

## BACKGROUND INFORMATION

The material presented in this chapter constitutes introductory material for topics to be considered in the remainder of the thesis. It is an extremely brief summary of pertinent results, theoretical and experimental, and physical arguments in common circulation among research workers and published literature in the field of superconductivity.

### 1.1 Superconductivity and Macroscopic Quantum Mechanics

Most of the experimentally observed effects associated with superconductivity can be phenomenologically accounted for with an extremely simple model. The electrons of the superconductor are considered to have condensed into a single macroscopic quantum state.<sup>1,2,3</sup> The wave function for this state is given by

$$\psi = \sqrt{\rho_S} e^{i\theta} \quad , \quad (1.1)$$

where  $\rho_S$  is the density of the electrons responsible for the superconductivity.

The microscopic theory of superconductivity<sup>4</sup> offers some justification for such an approach. In this theory, electrons with equal and opposite momentum and spins experience a net attractive interaction, mediated through the lattice. These electrons then form a loosely bound pair with zero center of mass momentum. All such pairs are then

in the same state, an allowed condition for such a Bose entity. In a superconductor the pairs are much closer together than are the electrons forming the pair. That is, since the electrons are so loosely bound they encompass a volume that contains the centers of mass of many ( $10^6$ ) other pairs. This multiple pair overlap allows information regarding the quantum state of the superconducting pairs to be spread over macroscopic distances compared to the mean free path of the electrons involved in the process.<sup>5</sup>

The large separation between the component electrons of a pair also implies that superconductivity is a non-local phenomena. Information concerning changes in the electrons' environment is transmitted over the range of the attractive interaction between the electrons. This range of attractive interaction, the size of a pair, is expressed by the coherence length,  $\xi$ .  $\xi$  is also the minimum distance over which the wave function in a material may change. The coherence length is temperature dependent. For bulk Nb at 0°K  $\xi_0 \cong 400 \text{ \AA}$  and can range up to  $10^{-4}$ cm for bulk aluminum at 0°K.<sup>6</sup>

What are the consequences one may derive from the model of superconductivity as a macroscopic quantum wave function? The momentum of a quantum state is given by the operator  $\underline{P} = -i\hbar\nabla$ . This is the total momentum composed of kinetic and electro-magnetic parts

$$\underline{P} = m\underline{v} + e\underline{A} = -i\hbar\nabla \quad (1.2)$$

The electrical current in the system will just be proportional to the velocity operator,  $\underline{v}$ . Applying this operator to the wave function

$$\psi = \sqrt{\rho_S} e^{i\theta} \quad ,$$

in the usual way yields an expression for the current carried by the superconducting state<sup>3</sup>:

$$\underline{j}_S = \frac{\rho_S \hbar}{m^*} \left( \underline{\nabla} \theta - q^* \frac{\underline{A}}{\hbar} \right) \quad , \quad (1.3)$$

where  $q^*$  and  $m^*$  are the effective values of the charge and mass associated with a pair; twice the values for a single electron. The above equation is of fundamental importance to the understanding of superconductivity. The phase is seen to be a measurable (to within a constant) portion of the supercurrent.

Applying Schrodinger's equation to this wave function yields its time dependence

$$i\hbar \frac{\partial \psi}{\partial t} = \mu \psi \quad , \quad (1.4a)$$

where  $\mu$  is the electrochemical potential. If one assumes the amplitude of the wave function does not depend upon time, which follows from the requirement of zero net charge in the system of lattice and electrons, then the supercurrent is non-divergent. Expanding Eq. (1.4) we obtain

$$\hbar \dot{\theta} = \mu \quad . \quad (1.4b)$$

By combining this with Eq. (1.3) one obtains

$$\frac{\partial}{\partial t} (\mu_0 \lambda^2 j_s) = E, \quad (1.5)$$

where  $\lambda^2 = \frac{m}{\mu_0 \rho e^2}$  and will appear again in a more physical context below. This is one of London's equations.<sup>1</sup> We may obtain the other of London's equations from Eq. (1.3) by taking the curl of both sides to obtain

$$\nabla \times (\mu_0 \lambda^2 j) = -B. \quad (1.6)$$

This equation when combined with Maxwell's equations predicts that the magnetic field will decay exponentially inside a superconductor with a characteristic length

$$\lambda = \left( \frac{m}{\mu_0 \rho e^2} \right)^{1/2}$$

as above.  $\lambda$  typically is of the order of  $10^{-7}$  m. This implies that for samples large compared to  $\lambda$  the magnetic field is excluded from the interior of the superconductor; the well known Meissner effect.<sup>7</sup> If the magnetic field is confined to the surface layer of a superconductor then the supercurrents and thus the electric field must also be confined to a similar layer near the surface.

As an example of the application of macroscopic quantum mechanics to a superconducting system, consider the case of a superconducting ring. Deep within the ring the supercurrent is zero. Equation (1.3) becomes

$$\nabla\theta = q^* \underline{\tilde{A}}/\hbar = 2e\underline{\tilde{A}}/\hbar \quad . \quad (1.7)$$

Taking the line integral of this equation around the ring, one obtains an expression for the phase difference around the ring

$$\theta_1 - \theta_2 = \oint \frac{2e\underline{\tilde{A}}}{\hbar} \cdot \underline{d\ell} \quad . \quad (1.8)$$

The right hand side is the magnetic flux through the ring.

The phase must be single valued and this imposes the requirement that

$$\theta_1 - \theta_2 = 2\pi m \quad \text{where} \quad m = 0, 1, 2 \quad . \quad (1.9)$$

We have the result that the magnetic flux through the ring is quantized in units of  $h/2e$ , now known as the flux quantum  $\phi_0$ .

$$\frac{2e\phi}{h} = 2\pi m \quad \phi = \frac{mh}{2e} \quad . \quad (1.10)$$

This result, which has been confirmed experimentally,<sup>8,9</sup> is a direct result of the assumption of a macroscopic quantum state, in the same manner as the assumption of a microscopic quantum state leads to quantization of the angular momentum in electronic orbits.

## 1.2 The Josephson Effects

Josephson<sup>10</sup> was the first to consider the interaction of two such macroscopic wave functions. He treated the case of two superconductors characterized by wave functions  $\psi_1$  and  $\psi_2$  separated by a thin (10-50 Å) insulating barrier. These two wave functions were allowed to interact very weakly through the action of pairs tunneling through the insulating barrier. This allowed the wave function on one side of the barrier to sample the phase and chemical potential,  $\mu$ , of the wave function on the other side. One may treat this interaction by considering the Schrodinger equation for each side to be slightly perturbed by that of the other side. The results of this calculation are the well known Josephson equations<sup>2</sup>:

$$\frac{d(\theta_1 - \theta_2)}{dt} = 2eV/\hbar \quad , \quad (1.11)$$

and

$$I = I_C \sin (\theta_1 - \theta_2) \quad , \quad (1.12)$$

where  $I_C$  is a constant,  $I$  is the current through the junction,  $V$  is the voltage across it. In a single superconductor the rate of change of the phase is proportional to the chemical potential  $\mu$ . (See Eq. (1.4b)) In the tunnel junction the difference in the rate of change of the phase in the two superconductors is just the voltage, the difference

in electrochemical potentials, between them. The second equation indicates that a current will flow through the insulating barrier. This current is composed of pairs tunneling from one superconductor to the other. This current depends only upon the relative phase between the two superconductors, for it to be a net current in one direction the voltage must be zero. The maximum current is obtained when

$$\theta_1 - \theta_2 = \pi/2$$

and is given by  $I_c$ . This current is known as the critical current. If the voltage is not zero then the phase difference changes between the two superconductors and the tunneling current becomes oscillatory with a fundamental frequency given by

$$\omega = 2eV/\hbar$$

This result may also be obtained from energy considerations. Each time a pair tunnels, to come into equilibrium with the potential on the other side, it must emit or absorb a quantum of energy, a photon, of magnitude

$$\hbar\omega = 2eV \quad . \quad (1.13)$$

It should be noted that the Josephson equations are non-local equations, in that they depend upon the phase difference on the two sides of the insulating barriers.

A dc voltage across the tunnel junction gives rise to a sinusoidal current flow but to no net current. Although this is a time dependent situation, it gives rise to no dissipation.

With reference to the above discussion of the Josephson equations, the "Josephson effects" may be simply defined. The dc Josephson effect refers to the flow of current due to a phase difference across the device, in the absence of a voltage. The experimental consequences of the interaction of an external magnetic field with this difference is to modulate in a periodic manner the maximum zero voltage current with the total flux through the junction.<sup>11</sup>

The ac Josephson effect refers to the oscillating supercurrents of frequency,  $\omega = 2eV/h$ , due to the voltage across the bridge,  $V$ .

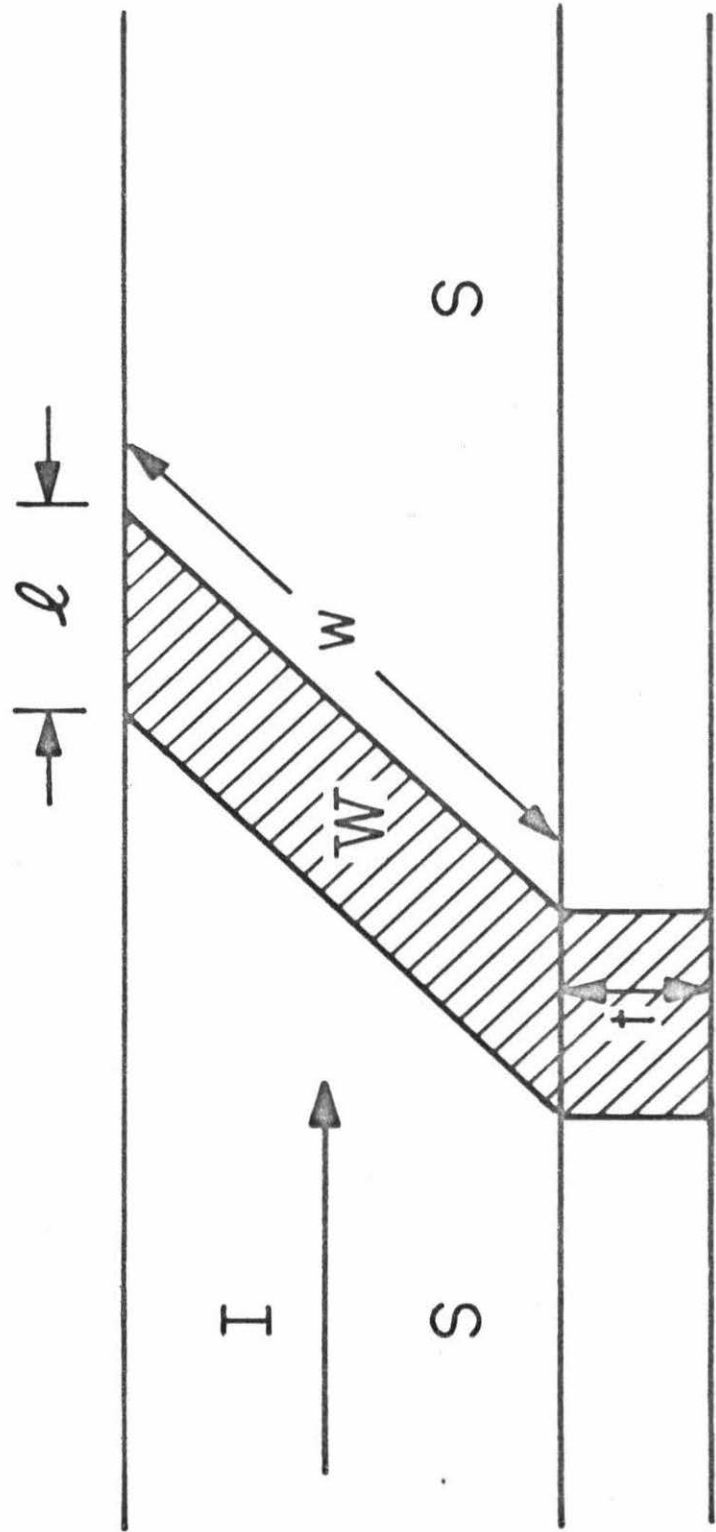
The experimental manifestations of these oscillating currents include constant voltage steps induced in the current-voltage characteristics of a tunnel junction in the presence of an external high frequency field of frequency  $\omega_{rf} = \omega_0 = 2eV_0/h$ .  $V_0$  is the magnitude of the constant voltage steps.<sup>12</sup>

### 1.3 The Josephson Effects in Non-Tunneling Structures

Experimentally it has been found that the Josephson effects are much more general than the particular structure, the oxide tunnel junction, used to analyze these effects.<sup>13</sup> Although the Josephson effects have been seen for superconductors separated by normal metals<sup>14</sup> and even semiconductors<sup>15</sup> we are primarily interested in the case shown in Fig. 1-1, two superconductors separated by a weakly superconducting region. A weakly superconducting material is one whose transition temperature,  $T_{C_w}$ , is lower than that of the surrounding superconductors. For convenience these structures are usually fabricated from superconducting thin films. This condition  $T_{C_w}$  implies that in the weakly superconducting region the density of superconducting carriers is less than that of the surrounding superconductors, resulting in a local inhomogeneity in the wave function. If the weak section is short enough ( $< 1\mu$  in our structures) this structure will exhibit effects analogous to the ac and dc Josephson effects.<sup>16</sup> Although the current voltage characteristics as well as the specific physical mechanism involved differ from the tunnel junction case, the zero voltage current depends upon the phase difference across the device, yielding the dc Josephson effect, and a voltage across the device results in current oscillations at frequency  $\omega = 2eV/h$  yielding the ac Josephson effect.

It has been found experimentally that the transition temperature of the weak section and its length are the fundamental considerations

Fig. 1-1. Schematic representation of a weakly superconducting proximity effect bridge. A thin superconducting film,  $S$ , is locally weakened in the area  $W$ . The weakened area has a transition temperature less than that of the original film,  $T_{CS} > T_{CW}$ . The weak area bisects the superconducting film perpendicular to the direction of current flow,  $I$ , forming a proximity effect bridge. Typical dimensions of the bridge are width,  $w$ ,  $10\mu$ , length,  $\ell$ ,  $0.5\mu$ , and thickness  $t$ ,  $100-300 \text{ \AA}$ .



for one of these bridges. That is, the specific method used to suppress the transition temperature of the weak section is of no importance. The central section of the superconducting films used for these bridges has been weakened in a number of ways: through the natural dependence of transition temperature upon film thickness,<sup>17</sup> through the proximity effect,<sup>16</sup> through structural damage occasioned by scratching the film,<sup>18</sup> and through structure changes induced by ion implantation.<sup>19</sup> Nor must these structures be fabricated from one type of superconducting thin film. Bridges have been successfully made from soft superconductors<sup>16</sup>; tin, lead, and indium; refractory superconductors<sup>16</sup>, Nb, Ta; and from high transition temperature alloys, NbN, Nb<sub>3</sub>Sn<sup>17</sup>, Nb<sub>3</sub>Ge.<sup>18</sup>

#### 1.4 Phase Slip

There are several physical differences between the weakly superconducting structures, in which conduction currents flow, and the oxide tunneling structure, in which only tunneling current flows. While both structures exhibit Josephson effects, these physical differences will lead to differences in the detailed operations of the two structures.

In the conducting structure, which we will refer to as a bridge, the fraction of the electrons in the superconducting state will be accelerated by the electric field present when a voltage is applied across the bridge. This is given by Eq. (1.5)

$$\frac{\mu_0 \partial j_s}{\partial t} = \lambda^{-2} E \quad , \quad (1.5)$$

where  $\lambda$  is the London penetration depth  $\lambda = (m/\rho\mu_0 e^2)^{1/2}$ . The electric field will also act upon the normal electrons to produce a current,  $j_n = \sigma E$ , where  $\sigma$  is the effective conductivity of the normal flow. Thus the current is composed of two components, a supercurrent and a normal current.

$$I = I_N + I_S \quad . \quad (1.14)$$

We presume that the voltage developed is just the normal current times the resistance of the device.

$$V = I_N R = (I - I_S) R \quad (1.15)$$

Generally these devices are current biased, fixing  $I$ , and leaving the ratio of supercurrent to normal current free to seek the value dictated by the dynamics of the superconductivity.

Consider an initial state in the weak superconductor with no current flow. Upon application of an electric field, generated by a voltage across the device, the supercurrent accelerates creating an increasing phase gradient across the device. As the supercurrent reaches the critical current of the device, the weak superconductor sustains the maximum permissible value of the phase gradient. The normal state then becomes energetically favorable and the wave function collapses, dissipating the kinetic energy of the formerly superconducting electrons. At this point, it is assumed that the system recondenses into a superconducting state, which experiences a phase gradient less by  $2\pi$  than that experienced before the collapse. This collapse and recondensation, assumed to happen on a time scale short compared to the Josephson frequency, constitutes the assumption of phase slip. After the phase slip the supercurrent again accelerates until the critical current is reached, and the process repeats. This ongoing process of acceleration and collapse of the supercurrent produces a quantum mechanical relaxation oscillation in the supercurrent. This

picture has been placed on firm theoretical grounds by describing this system with the Ginzburg-Landau description of superconductivity.<sup>20</sup>

The acceleration of the supercurrent is governed by the time rate of change of the phase gradient in the device. Integrating Eq. (1.5) across the device gives the time rate of change of the total phase difference across the device. That is

$$\frac{d(\theta_1 - \theta_2)}{dt} = 2eV/\hbar, \quad (1.16)$$

the Josephson relation. Since the quantum oscillation described above involves a phase change of  $2\pi$  per phase slip, we see that the oscillation occurs at the Josephson frequency  $\omega = 2eV/\hbar$ .

The oscillating supercurrent will produce an oscillating voltage as given by Eq. (1.15)

$$V(t) = (I - I_s(t))R \quad (1.15)$$

The oscillating voltage has been detected experimentally<sup>21</sup> and found to be consistent with a supercurrent given by

$$I_s(t) = I_c/2 \left( 1 + \cos(\theta_1 - \theta_2) \right) \quad (1.17)$$

and

$$\frac{d(\theta_1 - \theta_2)}{dt} = 2eV/\hbar \quad (1.18)$$

This yields a total current-voltage relation given by

$$V(t) = IR - I_c R/2 (1 + \cos(\theta_1 - \theta_2)) \quad (1.19)$$

and by Eq. (1.16).

The solution to these equations is just

$$V(t) = \frac{2IR[I - I_c]}{2I - I_c - I_c \cos \frac{2eVt}{\hbar}} \quad (1.20)$$

(see Appendix A)

If one solves for the time average voltage one obtains the dc current voltage relations.

$$\bar{V} = R(I^2 - II_c)^{1/2} \quad (1.21)$$

This characteristic has been found to fit the experimental I-V characteristic quite well.<sup>21</sup> It is also of interest to determine the harmonic content of the voltage oscillation given in Eq. (1.20). The Fourier expansion is

$$V(t) = \bar{V} \left[ 1 + 2 \sum_{m=1}^{\infty} \left( 2 I/I_c - \frac{2\bar{V}}{I_c R} - 1 \right)^m \cos \left( \frac{m2e\bar{V}t}{\hbar} \right) \right] \quad (1.22)$$

The oscillation occurs with a fundamental frequency set by the voltage across the device. At bias currents just above the critical current the oscillation has a high harmonic content. At higher currents, the oscillation becomes very nearly sinusoidal.

In the above model, dissipation is produced by both the normal flow and the phase slip process. The normal current produces a dissipation  $V^2/R$  as expected. Each time the supercurrent collapses the kinetic energy of this current is lost. This energy is just  $\bar{I}_S \phi_0$  where  $\bar{I}_S$  is the time average supercurrent. This loss recurs at the Josephson frequency so the power lost is just

$$P = \bar{I}_S \phi_0 \omega = \bar{I}_S V$$

The total dissipation is given by

$$VI = V^2/R + VI_S = (\bar{I}_N + \bar{I}_S)V \quad (1.23)$$

Thus at given voltage the bridge dissipates more energy than the normal resistor  $R$  but for a current bias will dissipate less than the equivalent resistor. The dissipation due to the time average supercurrent persists up to quite high currents as given by Eq. (1.21)

$$\bar{I}_S = I - \bar{V}/R = I - (I^2 - II_C)^{1/2} \rightarrow I_C/2 \quad . \quad (1.24)$$

$I \gg I_C$

The tunnel junction, by contrast, does not have dissipation due to the pair tunneling currents.

### 1.5 Proximity Effect

If a normal metal and a superconductor are placed in intimate contact then the pairs can drift into the normal material for a portion of their lifetimes.<sup>22</sup> Inside the normal material the pair density falls off exponentially with distance from the boundary.<sup>23</sup> If the thickness of the normal material is less than the characteristic distance for the exponential decay, approximately the coherence length,  $\xi$ ,  $\sim 100 \text{ \AA}$ , superconductivity will be induced into the normal material, and conversely if the superconductor is thin compared to the characteristic dimension of change of the wave function, the coherence length, the transition temperature of the superconductor will be depressed. This process is known as the proximity effect.

The proximity effect enters our bridges in two ways. The transition temperature of the weak section of our bridges is usually set by varying the thickness ratio of superconducting and normal films in a layered structure as will be described in Chapter 2.

More importantly, however, the proximity effect infuses the weak superconductor with pairs from the surrounding strong superconductors. These pairs carry coherent phase information from the neighboring strong superconductors. For the bridge to exhibit the Josephson effects the bridge must be short enough so that these tails of the strong superconductor wave functions may overlap. As expected from these considerations, the transition temperature of the weak section tends to rise, for a given intrinsic transition temperature,  $T_{C_w}$ , as the bridge is made shorter.

## FABRICATION OF PROXIMITY EFFECT BRIDGES

### 2.1 Introduction

It should be clear from the discussion in the first chapter that all that is needed to observe all the Josephson effects is a local inhomogeneity in the number of superconducting carriers. The particular inhomogeneity which we utilize is a local depression of the superconducting transition temperature  $T_c$ . This depression of the transition temperature results in a lower density of superconducting pairs in the depressed portion of the superconductor. By local, we mean an area sufficiently small that the coherent phase information is carried across the weakened region. In these films this is  $< 1\mu$ .

The question of device fabrication becomes a question of developing a method to locally modify the transition temperature of a superconductor. Towards this end, consider a superconductor in intimate contact with a normal material. If the films are thin enough, this gives rise to the well known proximity effect;<sup>1,2</sup> Due to the finite extent of the coherence length the superconductivity cannot end sharply at the interface, indeed, the wave function decays exponentially into the normal material. Therefore, there is a finite probability that a given pair will find itself, for part of its life, in the normal material. If the superconducting film is thin enough ( $< \xi$ ), so that its thickness dominates the coherence length, then a pair can spend a significant part of its life in the normal film. In the normal film the pairing potential is much weaker, so the average potential seen by

the pair will be lower than that in the superconducting film alone. This gives a transition temperature  $T_c'$  lower than that of the superconducting film alone,  $T_c$ .

The exact transition temperature depends on the thicknesses of the two films. If the thickness of the superconducting film goes to zero then  $T_c'$  also goes to zero. If, on the other hand, the thickness of the normal film goes to zero then  $T_c'$  goes to the appropriate value,  $T_c$ , for a superconducting film of the given thickness. Finally if the thickness of the superconductor is much greater than the coherence length,  $t_s \gg \xi$ , then  $T_c'$  goes to  $T_c$  the bulk value for the superconductor, as the relative probability of a pair being in the normal material diminishes.

Now consider the situation of two different superconductors, A and B, with transition temperatures  $T_{c_a}$  and  $T_{c_b}$ . Without loss of generality  $T_{c_a}$  is picked greater than  $T_{c_b}$ . Once again the transition temperatures will be modified by the proximity effect. Then due to the same argument about the average pairing potential,  $T_{c_b} \geq T_c' \geq T_{c_a}$  where  $T_c'$  is again the transition temperature for the combination. Again the exact value of  $T_c'$  depends on the thickness of the two films.

In a structure of this sort one can vary the transition temperature by varying the thickness of the film over a small area, thereby producing a weak link. In what follows we shall discuss the fabrication of the layered films, processes for thinning selected areas of the films, and the process for selecting the area to be weakened.

## 2.2 Fabrication of Layered Refractory Thin Films

The following materials have been found to be useful in the fabrication of proximity effect bridges, as superconductors or as normal metals; Nb, Ta, W, Ti, and Zr. These materials present significant advantages over non-refractory materials. As deposited in a thin film, they form a tough coating clinging tenaciously to the substrate. The fact that the films are so tough makes them impervious to normal handling and to cycling from room to liquid helium temperatures. The high temperatures required to evaporate these materials imply there will be very little interdiffusion if the films are stored at room temperature. The superconducting transition temperature of these films gradually decreases with time yielding an approximate shelf life of several years ( $\Delta T_c \lesssim 0.2^\circ\text{K}$  for time of 2 years). It is believed that this is due to oxygen slowly diffusing into the films. These materials also form a very tough protective oxide which can be grown anodically allowing precise thickness control of the films.

The properties of these materials and combinations of them which have been found useful for proximity effect bridges are listed in Table 2-1. Figure 2-1 shows the transition temperature dependence upon thickness for some of the combinations. For most of the work reported in this thesis the proximity effect bridges were fabricated from a thin film parent material of Nb and Ta nominally  $100 \text{ \AA}$  on  $200 \text{ \AA}$ . This particular combination of materials was chosen for its strong proximity effect and convenient operating temperatures. As shown in Fig. 2-1 junctions fabricated in these films will have a transition temperature

Table 2-1

## FILM PROPERTIES

Film	Thicknesses Ratios	Transition Temperature °K	Resistance At $T > T_c$ $\Omega/\square$
Nb/Ta Sapphire Substrate	100Å/200Å	5.3	1
Ta/Ti Sapphire Substrate	~200Å/200Å	3.2	1.5
Ta/Ti Glass Substrate	~200Å/200Å	3.0	4.5
Nb/Ta/W Sapphire Substrate	100Å/100Å/100Å	5.6	1
Nb/Ta/Zr	100Å/100Å/100Å	6.2	3
Nb/Zr	100Å/200Å	7.6	5

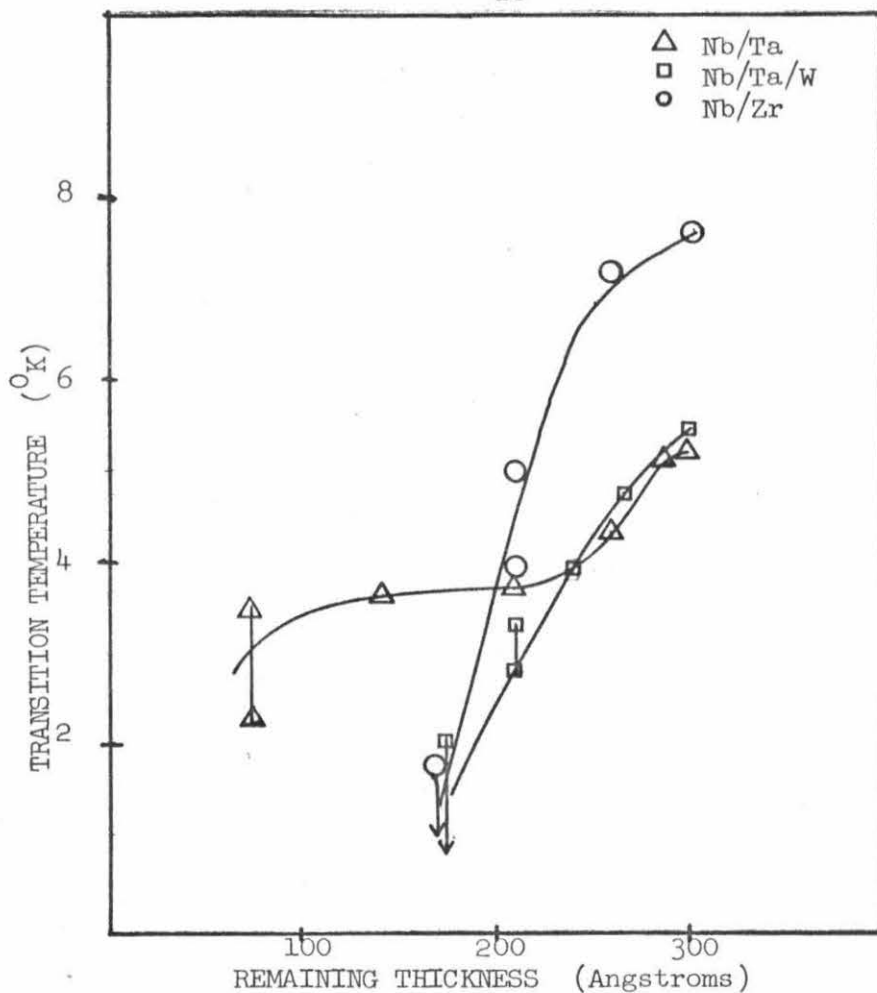


Fig. 2-1. Dependence of superconducting transition temperature upon remaining film thickness for several combinations of materials. All films are on sapphire substrates. Triangles denote Nb/Ta; 100 Å/200 Å. Squares denote Nb/Ta/W; 100 Å/100 Å/100 Å. Circles denote Nb/Zr; 100 Å/200 Å.

$T_c$  which, if desired, may easily be placed just below 4.2°K, and a wide range of thicknesses gives approximately the same transition temperature  $\sim 3.9^\circ\text{K}$ . This particular combination of thicknesses also lends itself to the anodization techniques to be described later.

The transition temperature of Nb and Ta thin films decreases dramatically with the addition of interstitial  $\text{O}_2$  and  $\text{N}_2$ . A decrease of about 1°K per atomic percent oxygen has been observed for Nb<sup>3</sup>. The films used in this work must be deposited under ultra-high vacuum conditions to sustain the transition temperatures at a high level.

To obtain films of sufficiently high quality one needs to use an ultra-high vacuum system using a combination of ion pumping and cryo-sublimation pumping, with sorption pumps for roughing. In the system one also needs an electron beam gun with multiple hearths, a substrate holder capable of being heated to  $\geq 400^\circ\text{C}$ , a capability for heating the system to clean those parts which will become hot during the evaporation, and a Sloan deposition monitor to monitor the film thicknesses.

The quality of the films was evaluated solely upon their usefulness in proximity effect device fabrication. This is primarily concerned with the mechanical and superconducting properties of the film. The films should be of the proper thickness, adhere well to the substrate, and be as free of pinholes as possible. These properties are influenced primarily by choice of substrate and materials and by the preparation of the substrate.

In addition the films should be superconducting at a temperature as near as possible to the bulk transition temperatures and the normal

to superconducting transition should occur over as narrow a temperature range as possible. These properties are controlled primarily by the thickness of the film, the temperature of the substrate during evaporation, the pressure during the evaporation, and the choice of substrates. Of these parameters, variations in the first two have the largest effect upon the superconducting properties. The effect of the second two parameters, while not as strong, is still significant

Let us delineate the effects of these parameters upon Ta and Nb films.

In the case of Ta, the superconducting transition temperature is strongly dependent upon the film thickness. The transition temperature decreases rapidly with thickness of the films, due to stresses imposed by the substrate. In the thin films we use, the other parameters in the system must be optimized to prevent oxygen inclusions and to allow the Ta to remain as stress free as possible. If the other parameters are optimized, as discussed below, then a thickness  $\geq 300 \text{ \AA}$  gives a reliable superconducting transition temperature above  $3.8^\circ\text{K}$ , if the thickness falls below  $200 \text{ \AA}$  the transition temperature is below  $3.6^\circ\text{K}$ . The temperature of the substrate during the evaporation must be above  $400^\circ\text{C}$ , reducing the probability that a contaminant striking the surface will remain. In the range  $400^\circ\text{C}$  to  $800^\circ\text{C}$  there is a slight improvement with increasing temperature. Below  $400^\circ\text{C}$  the transition temperature of the films falls rapidly with substrate temperatures. Ta films evaporated onto a room temperature substrate have  $T_c < 1.3^\circ\text{K}$  for all thicknesses less than  $1000 \text{ \AA}$ . As measured at the ion pump, small changes in pressure in the range  $10^{-8}$  to  $10^{-7}$  torr have little effect

on the quality of the film but at higher pressures the superconducting transition temperature falls sharply. Finally, the effects of substrate choice are minor but sapphire gives a sharper and a slightly higher temperature transition.

The conditions for niobium are similar but not as stringent as those imposed by the tantalum films. The critical values of the above parameters for high quality films are; thickness  $> 100 \text{ \AA}$ , substrate temperature  $200^{\circ}\text{C}-400^{\circ}\text{C}$ , pressure during evaporation  $5 \times 10^{-7}$  torr -  $8 \times 10^{-8}$  torr, substrates, sapphire or 7059 glass. In the case of Nb, for thicknesses  $> 200 \text{ \AA}$  films on room temperatures substrates will be superconducting though they have a low transition temperature and a very broad normal to superconducting transition.

In short the results for these two materials may be summarized<sup>4</sup> with reference to Fig. 2-2. The transition temperature of the films, their resistivity at  $4^{\circ}\text{K}$ , and their transition widths vary as universal functions of the following parameters; film thickness, substrate temperature, inverse of the pressure during evaporation, and to some extent substrate material. In Fig. 2-3 we give, as a specific example, the dependence of  $T_c$ , and resistivity, as a function of thickness for Nb films.

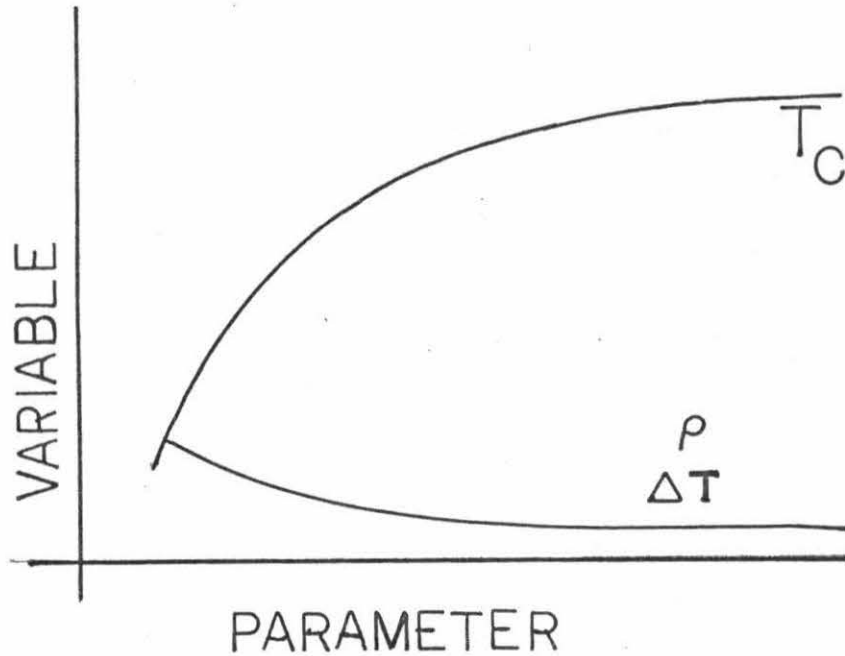


Fig. 2-2. Universal curves indicating the dependence of transition temperature,  $T_c$ , resistivity,  $\rho$ , and width of superconducting transition,  $\Delta T$  upon various parameters. The parameters include; film thickness, substrate temperature during evaporation, inverse of pressure during evaporation, and to some extent, substrate material.

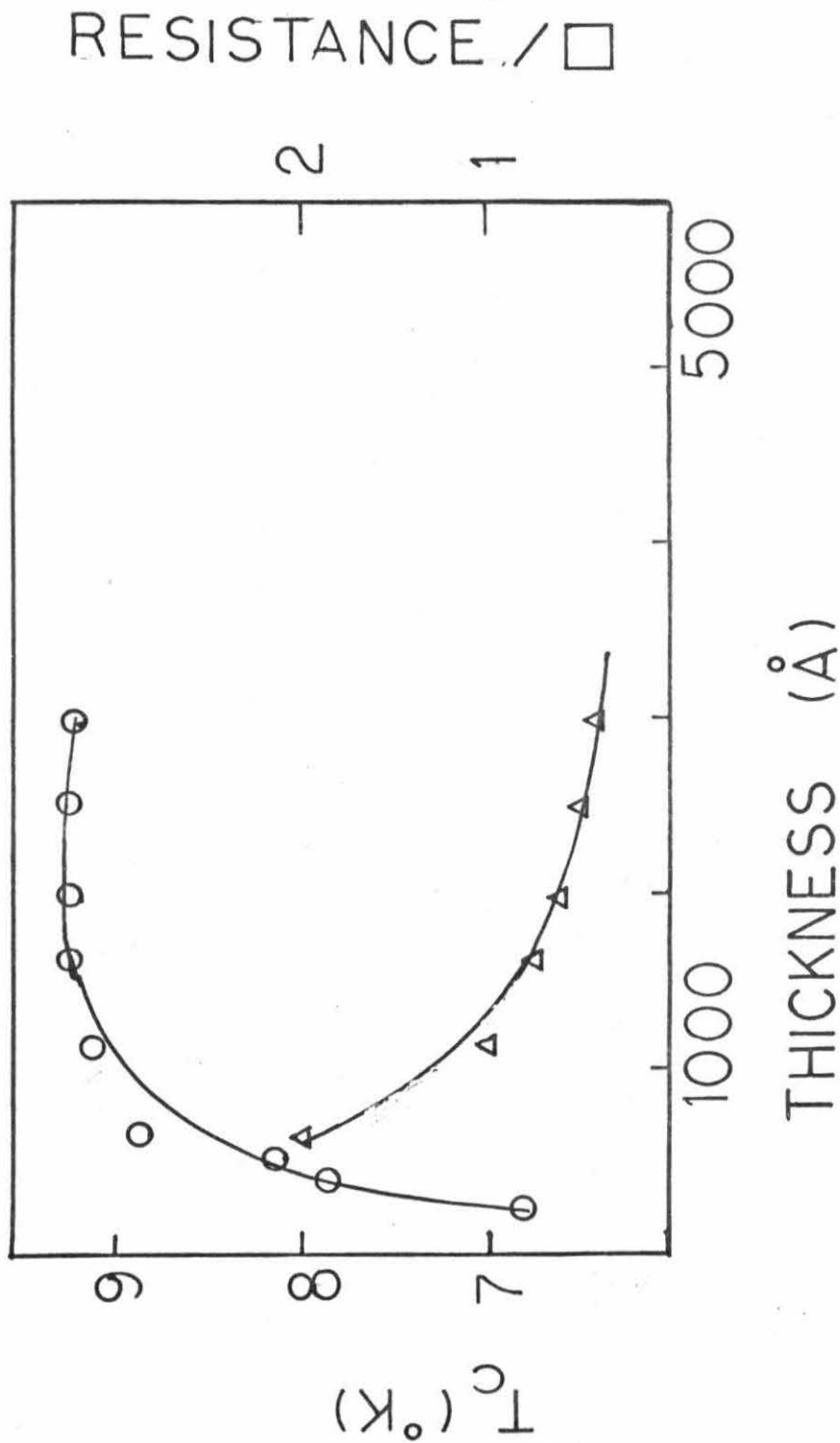


Fig. 2-3. A specific example of the universal curves shown in Fig. 2-2. The upper trace is the transition temperature of Nb films as a function of thickness. The lower trace is the resistance per square of these films as a function of thickness.

### 2.3 Fabrication of Superconducting Circuits

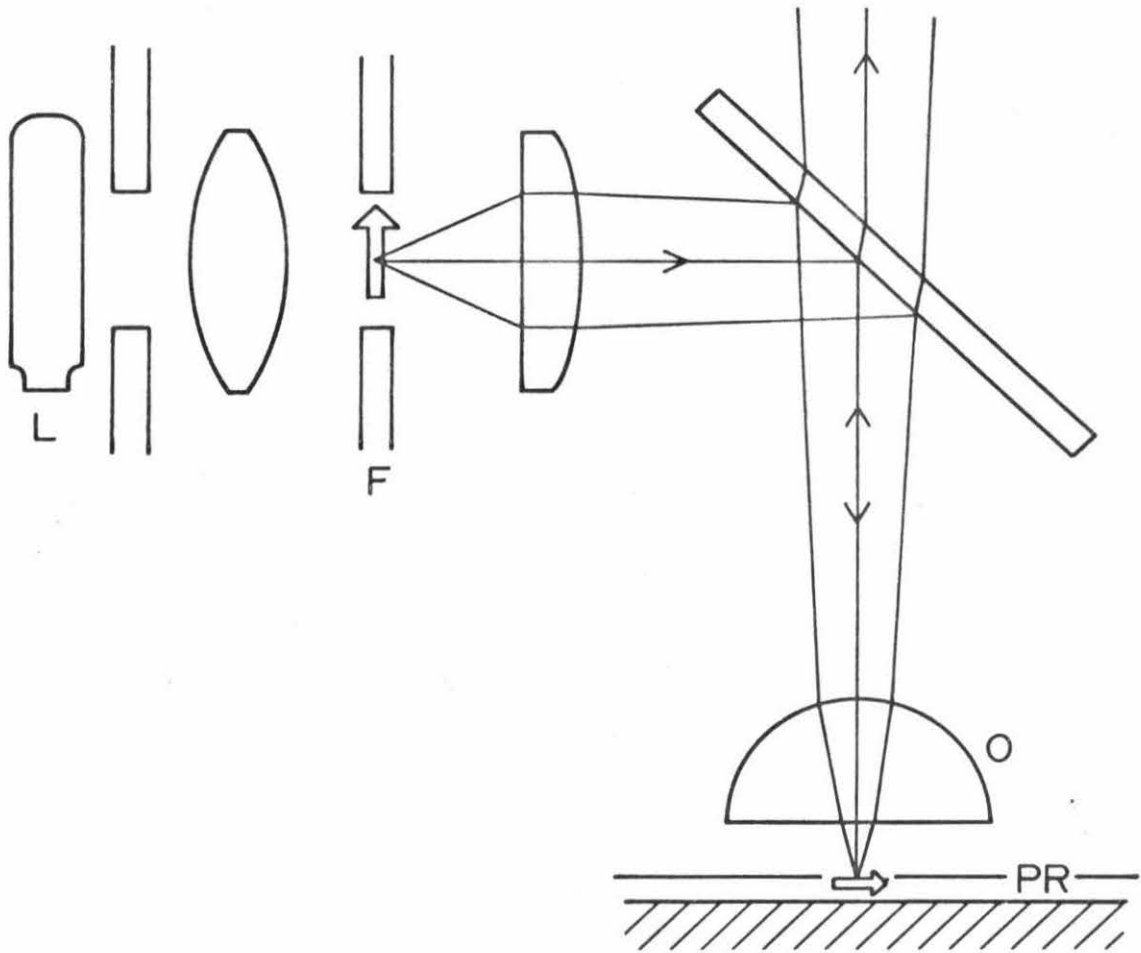
As outlined above the proximity effect bridges are fabricated by bisecting a superconducting film with a region of weaker superconductivity. In all the films we have described the weakened area is produced by locally thinning the film. The thinning may be accomplished in many ways; growth of an anodic oxide or anodization, ion beam etching, plasma etching, or chemical etching. Most of the work to be reported in this thesis utilized the anodization technique, which will be described in detail. The areas to be thinned are selected with photoresist (PR) films. These PR films are exposed with contact masks for large area patterns and by projecting the desired pattern through a reflecting microscope for more detailed patterns.

## 2.4 Microscope Projection

Submicron patterns in photoresist have been routinely obtained by using a reflected light microscope to project masks. Registry of subsequent masks to  $0.5\mu$  is easily achieved. Readily available masks with  $20\mu$  details can be used to obtain submicron results since the image is demagnified as it is projected through the objective lens. Requiring only a standard reflecting microscope and low cost masks, this method is fast and flexible, resembling a hand tool more than a production system. Thus such a technique is ideal for the research laboratory.

This work was done with a Zeiss RA microscope equipped with a II-B vertical illuminator. When the vertical illuminator of the microscope is adjusted for Koehler illumination, the field stop is imaged through the objective upon the focused sample. (See Fig. 2-4). If a mask is placed in the plane of the field stop, it too will be imaged upon the sample--the pattern of the mask appearing as an illuminated area on the sample. This allows optical alignment of the mask with patterns already on the sample. The image of the mask is smaller than the mask by an amount that depends on the power of the objective used. This demagnification allows the use of masks whose characteristic dimensions are much larger than those of the desired photoresist image. This increase in detail size for the masks implies that they are much cheaper and easier to construct than a contact mask producing the same final pattern in the PR film. Acetate photoreductions of artwork and simple ruby tape constructions are the most common sorts of masks employed, although such diverse items as

Fig. 2-4. Schematic diagram of vertical illuminator used in mask projection. In normal operation, when the microscope is adjusted for Koehler illumination, the field stop, F, is imaged upon the sample. If a mask is placed in the plane of the field stop, it is projected and demagnified through the objective, O, and imaged upon the photoresist surface.



broken razor blades, fine wires, and electron microscope grids have been successfully used as masks. The only requirement is an ability to block that portion of the optical spectrum from green to the near ultraviolet.

If the mask is mounted slightly behind the plane of the field stop, it is necessary to raise the stage to image the mask upon the sample. In this situation the microscope is not focused upon the sample, nor is the image of the mask viewed with the microscope. If such defocusing is necessary the defocusing distance must be determined for each microscope objective, either by trial and error, or, in the case of long working distance objectives, by directly viewing the sample with a separate microscope to determine the stage position giving the sharpest image of the mask. For most objectives the defocusing distance may be approximately calculated,<sup>5</sup> by measuring the stage displacement from the point at which the substrate is in focus to the point an image of the mask is in focus in the eyepiece. This procedure is illustrated in Fig. 2-5.

A given mask will expose different areas depending upon the power of objective used. Thus, the minimum detail which can be obtained depends upon the resolution of the objective used. For submicron work, we use a 100 X oil immersion objective with a numerical aperture of 1.4. Table 2-2 is a summary of the properties of this system with a number of different objectives.

Photoresist (Shipley 1350-Z) is spun on and air dried. The speed of the spinner determines the thickness of the resulting PR films. This thickness may be varied from 2 to  $0.2\mu$  with the corresponding speed

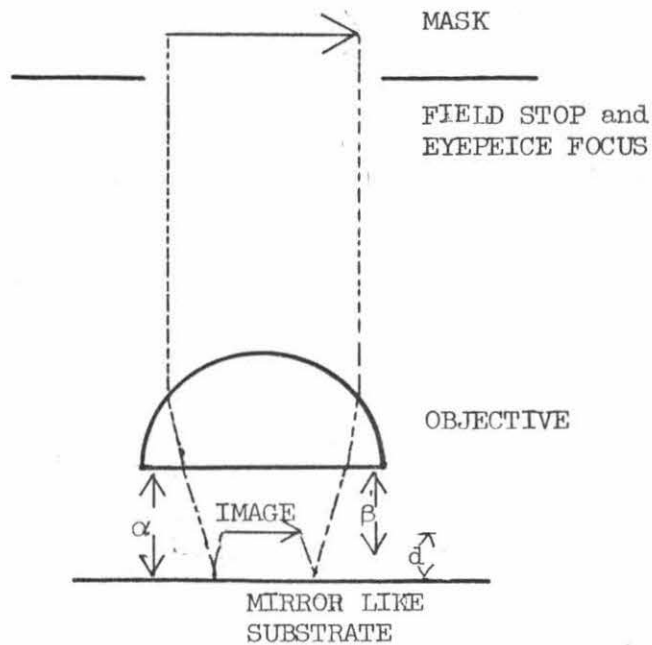


Fig. 2-5. Method of calculating defocusing distance for a given objective. The desired image of the mask is  $d$  above the mirrored surface  $M$ . When the substrate  $M$ , is in focus in the eyepiece the stage to objective distance is  $\alpha$ . The mask, located behind the field stop, will be in focus in the eyepiece at a stage to objective distance  $\beta$ , where  $\beta = \alpha - d/2$ .  $\alpha - \beta$  is readily measurable with a calibrated stage.  $\alpha - \beta = d/2$  where  $d$  is the distance the stage must be raised to focus the image of the mask upon the substrate.

Table 2-2

## MICROSCOPE OBJECTIVES

Objective	Demagnifying Factor	Minimum PR Detail	Field of View
100X with immersion oil	43.5	0.2-0.3 $\mu$	100 $\mu$
100X with glycerin	43.5	0.3-0.5 $\mu$	100 $\mu$
40X	17	0.8 $\mu$	250 $\mu$
8X	4	5 $\mu$	1.25mm
4X	2	10-15 $\mu$	2mm

range of 200-15,000 rpm. The PR layer must be thinner than the smallest detail to be exposed. Another boundary condition on thickness is the voltage that a layer of PR can withstand during anodization. Below 100 V the PR easily withstands 120 anodizing V/ $\mu$  thickness.

The photoresist is exposed by the above projection scheme which after development leaves a positive (exposed) image of the mask. Exposure times may be adjusted by varying the intensity of the light and are usually picked to be less than 1 min to minimize vibration problems. For a given intensity, the exposure time will vary with the objective used. The PR is then developed in the standard way with Shipley A-Z developer (1:1) (except in the case of the oil immersion objective as will be discussed later). For 45 sec, followed by a 1 min rinse in distilled water. The PR is thus removed from the region of the projected image of the mask.

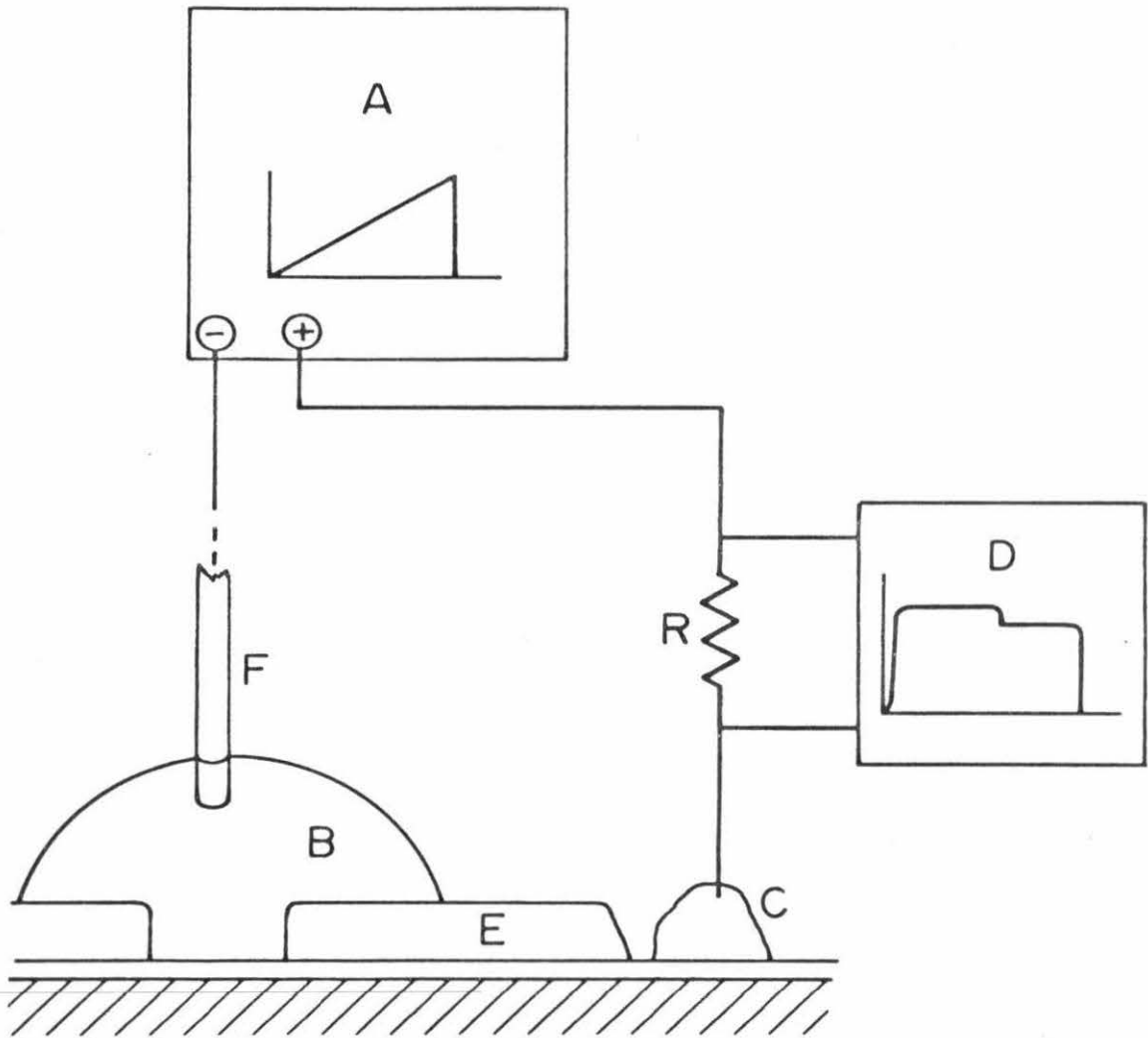
## 2.5 Anodization

Metal removal by anodization provides much more control and reproducibility than chemical etching. Over small areas the anodized depth is uniform to within a few angstroms, and along the boundary undercutting is less than  $0.1\mu$ . There exists an extensive literature on refractory metal oxide films formed by anodization.<sup>6</sup> But apparently, only in a few instances has anodization been used for metal removal. The exposed portion of the positive photoresist film determines the areas where metal is to be removed. These areas are covered with a drop of electrolyte; the film is made positive relative to a gold electrode which is in the electrolyte, as shown in Fig. 2-6.

The potential between the film and the gold electrode determines the thickness of the oxide formed. At a constant potential the oxide grows so that its thickness approaches this limit asymptotically with time. This dependence on voltage provides a convenient determination of the thickness of the oxide, and hence the thickness of the metal remaining in the film. The anodization oxide remains in place protecting the portion of the film during subsequent anodizations; thus, the metal is not physically removed, but simply converted to an insulator. These protective oxides, as well as the metal films themselves, cling tenaciously to the substrate, enabling them to resist the stresses involved in anodization. By integrating the amount of current that flows during anodization and knowing the area being anodized, one can estimate how many atomic layers have been removed.

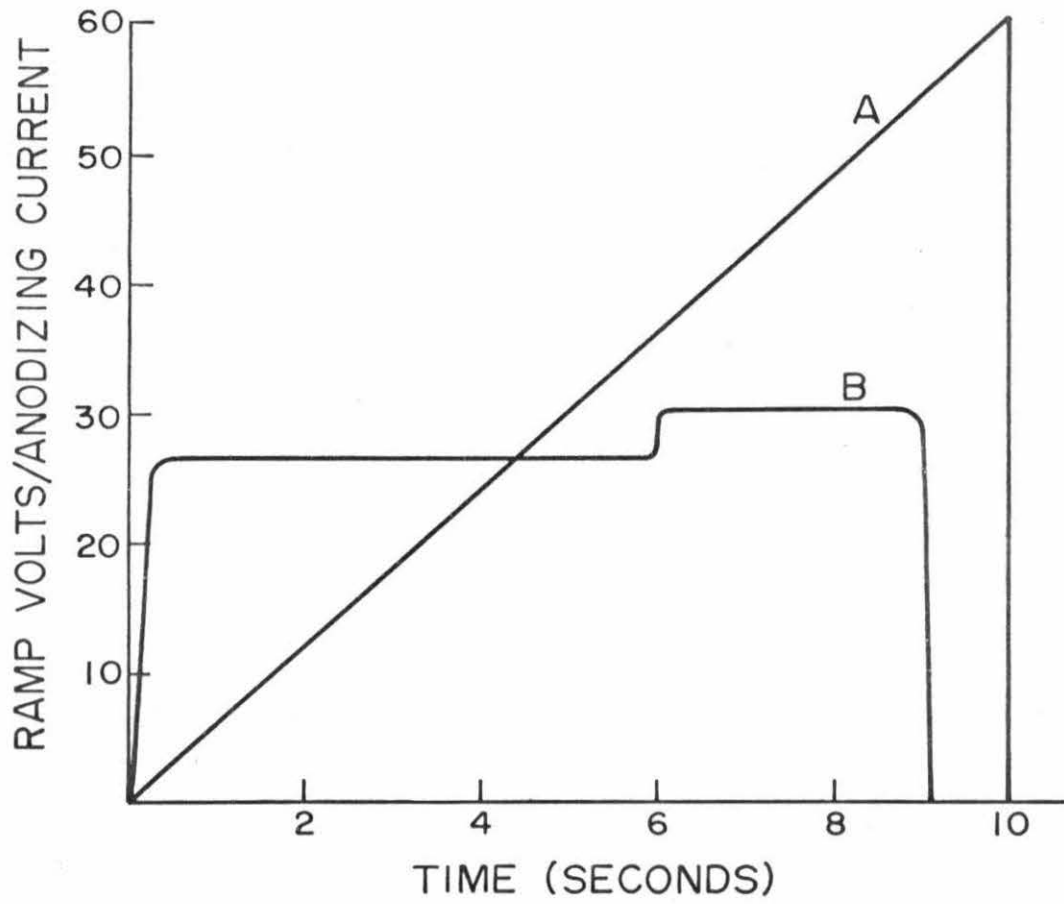
There are two drawbacks to this method: (1) There are often pin

Fig. 2-6. Schematic diagram of anodization circuit. A voltage ramp, as shown in A, is applied between the film and the Au electrode, F, immersed in the drop of boric acid, B. Current flow is monitored with R, a 100  $\Omega$  resistor; a typical current trace is shown in D. Contact is made to the film with indium tab C. The photoresist film E selects the area to be anodized.



holes or scratches in the PR under the drop and the current contributed by these areas is unknown; (2) if too short a voltage pulse is applied to a large film area, the resulting thickness is not uniform to the extent that the nonuniformity is apparent upon visual inspection. For this reason, a method of equilibrium anodization has been developed -- essentially, it is a method of anodizing at constant current. A voltage ramp is applied to the electrodes. The duration and rate of the ramp are determined by monitoring the current flowing in the anodization circuit. The rate is chosen so that a constant current is reached after a rapid buildup; then the anodization is in equilibrium and the oxide is growing at a constant rate. To calibrate a film thickness, one typically exposes a  $100\mu$  diam circle in the PR film and applies a ten second ramp across the electrodes while monitoring the current flowing. Figure 2-7 illustrates this technique applied to a layered film composed of Nb on Ta. The fast rise to a constant current indicates an equilibrium rate, the change in constant rates at 30V indicates a change in quality of film, in this case, the first 30V removed Nb and the rest of the ramp removed Ta. The sudden decrease in current at 55V indicates that all the metal has been anodized and this potential is defined as the breakthrough voltage. Using optical means to independently determine the thickness of our metal films, we have discovered the following anodization rates using boric acid as the electrolyte: Nb --  $6 \text{ \AA}/\text{V}$ ; W --  $4 \text{ \AA}/\text{V}$ ; Ta --  $8 \text{ \AA}/\text{V}$ ; Zr --  $10 \text{ \AA}/\text{V}$ . These values apply to films evaporated at pressures of  $10^{-8}$  torr and onto sapphire

Fig. 2-7. Current and voltage characteristics of a complete anodization of a  $100\mu$  spot on a Nb/Ta  $300 \text{ \AA}$  film. The voltage, trace A, is applied in a constant ramp with slope 6 V/sec. The current, trace B, is plotted in arbitrary units. The steep initial rise followed by a constant current indicates an equilibrium anodization. The change in current at 35 V (at 6 sec) marks the transition from Nb to Ta. The sharp fall at 55 V (9 sec) indicates the film is completely anodized.



substrates at 400°C.

It is often convenient to use a faster ramp than would supply the equilibrium rate, especially if undercutting is a problem. In this case a special calibration technique is used. An area identical in size to the required area is first tested with a fast ramp whose final voltage exceeds the equilibrium breakthrough value. The fast ramp breakthrough voltage is greater than the equilibrium value. Depth control is achieved by using a ramp of the same slope as the test ramp, but terminating at a voltage indicated by integration of test anodization current. For example, to anodize two-thirds of the way through the film, one finds the voltage at which two-thirds of the anodization charge has already passed through the test area and uses this voltage as the terminal voltage of the ramp. It is found that if the ramp time is very rapid, anodization current never becomes constant; the metal is no longer removed uniformly over the area of anodization but is preferentially removed along the boundaries of the PR mask. Instead of a voltage ramp, a voltage pulse can be used to anodize. Generally, pulse work is preferred when complete removal of metal from areas is required since a pulse takes less time to pass the necessary charge than a ramp, thus minimizing the time during which undercutting can take place. However, ramps have proven far superior for depth control and reproducibility.

## 2.6 Example of Fabrication

As a specific example, we outline the construction of a line  $0.5 \times 50\mu$  in a  $300 \text{ \AA}$  Ta film. First, clean the Ta surface with water, acetone, and Chromerge baths to remove any organic or metallic contaminants. Spin on Shipley positive A-Z 1350 PR at 10,000 rpm. This gives a PR film of less than  $0.5\mu$  thickness. The PR film should always be thinner than the smallest dimension that is to be constructed (aspect ratio  $\leq 1$ ). The PR is filtered to  $0.5\mu$  when applied to avoid any particle inclusions, and simply air dried for 3 min after application, to avoid heat degradation through oxygen diffusion of metal films.

A transparent line  $15 \times 1500\mu$  on a black acetate film serves as the mask. The mask is fitted in place of the auxiliary lens holder in the vertical II-B illuminator of a Zeiss RA microscope; this is just behind the field stop. Illumination comes from a standard 6V, 15 W lamp run at 4.5 V. The light column is restricted by setting the aperture stop to 4. A red filter is placed in the vertical illuminator to allow mask adjustments and focusing without exposure of the PR. An oil immersion 100X objective lens is used with Cargille's immersion oil. Since the sample is semitransparent, a red stage slide is used to prevent stray exposure by scattered light. After the mask is brought into focus through the microscope, the stage is lowered  $1\mu$  to assure a sharp image of the mask on the sample for this objective. The red filter is removed for approximately an 8 sec exposure. To remove the immersion oil, the sample is blotted, rinsed in A-Z developer, and then

gently wiped with developer soaked lens paper or facial tissue. The PR is developed for the remainder of our standard time (45 sec) and rinsed in water, leaving a  $0.5 \times 50\mu$  line in the PR film.

The metal is thinned in this exposed spot by anodization. A drop of electrolyte, an aqueous solution of boric acid, is placed on PR pattern (see Fig. 2). A positive voltage contact is made to the metal film in a remote corner. A gold wire forms the negative contact to the drop. A 30 V 0.1 sec ramp is applied across these contacts. This is an equilibrium anodization, thus  $(30 \text{ V}) (8 \text{ \AA}/\text{V}) = 240 \text{ \AA}$  is removed. The PR is removed with acetone. Under microscope inspection with reflected light, the completed line appears darker than the surrounding film.

The problem of finding the exact focus point for an object, such as the line in the above example, which is small enough to be diffraction limited can be eased by placing a blue filter in the light path and focusing and exposing on the line with monochromatic light. The effects of small nonuniformities in the mask may be reduced by placing a frosted glass in the vertical illuminator. Both of these measures affect the exposure times.

For submicron work, it is necessary to use a 100X lens. These lenses typically have a field of view of about  $100\mu$ . If larger patterns are necessary, it is easy to "microscopically continue" the pattern with overlapping fields of view. To make a long line, we simply translate the stage uniformly while projecting a line mask.

A mask with several closely set fine details may produce a

distorted image due to optical interference. For example, two parallel line segments may exhibit broadening in their middles (cigar syndrome). Careful spacing and exposure times can help, but it is often necessary to expose one line at a time, either on the same PR film or in consecutive exposure -- anodization cycles. Microscope vibrations and mask movements have not been a problem as long as light intensity is high enough to keep exposure times less than a minute.

## 2.7 Advantages and Limitations

The combination of anodization and microscope photolithography techniques with the extreme ruggedness of the refractory metal films yields a unique realization of the Josephson effects, the refractory metal proximity effect bridge. Using the above techniques, these bridges may be quickly and easily fabricated within certain well defined limitations. The optical resolution of our microscope sets a lower limit on bridge length of about  $0.3\mu$ . Shorter bridges have been made but require the use of a scanning electron microscope and such bridges were not used in the work discussed in this thesis. Anodization of refractory metals does not seem to be resolution limited. However, for large areas ( $> 0.25 \times 10^{-6} \text{m}^2$ ) undercutting can become a serious problem. Metal removal through anodization is limited to a depth such that the applied voltage does not exceed the breakdown potential of the photoresist. This effectively limits us to films of less than  $500 \text{ \AA}$  thickness, necessitating the care in film fabrication described early in the chapter. Bridges have been fabricated using ion beam etching and plasma etching for metal removal, but again these techniques fall outside the scope of this work. Within the above limitations the combination of refractory metal removal through anodization and exposure of photoresist through the microscope presents a powerful tool for laboratory thin film processing.

## Chapter 3

## APPLICATIONS OF QUANTUM INTERFERENCE AT FINITE VOLTAGES

In the preceding two chapters we have considered the behavior and fabrication of the proximity effect bridges. In this chapter, we will consider combinations of two such bridges into superconducting thin film circuitry with emphasis upon use as quantum interferometers and the detection of small currents.

### 3.1 Quantum Interference at Zero Voltage

Quantum interference effects between two Josephson junctions at zero voltage offer compelling experimental evidence<sup>1,2</sup> to London's representation of superconductivity as a macroscopic quantum state whose phase is coherent over the extent of the superconductor.<sup>3</sup> As with any coherent wave function, one should be able to ascertain relative phase between two points through interference effects. This process forms important background material for much of the work in this chapter so we present a fairly detailed account.<sup>4,5</sup>

In a superconductor, the gradient of the phase of the wave function,  $\nabla\theta$ , is set by the total momentum, mechanical and electromagnetic. Therefore by integrating this quantity between two points, A and B, one obtains the phase difference between them.

The phase gradient in a superconductor is given by Eq. 3.3

$$\nabla\theta = \frac{e^*}{\hbar} (\mu_0 \lambda^2 \mathbf{j} + \mathbf{A})$$

$\lambda^2$  is the London penetration depth  $\lambda^2 = \frac{m^*}{\rho e^2 \mu_0}$  .

If we consider a superconducting strip with a Josephson element in it, then the phase difference between ends of the strip will just be the path integral of the above expression along the strip plus the phase difference across the Josephson element,  $\delta$ . The phase difference across the Josephson element is determined.

$$j_s = j_0 \sin \delta \quad , \quad (3-1)$$

which implies

$$\theta_A - \theta_B = \int_A^B 2e/\hbar (\mu_0 \lambda^2 j + A) d\ell + \delta \quad . \quad (3-2)$$

Consider the geometry indicated in Fig. 3-1, two Josephson elements connected in parallel by superconducting links. The phase change from point A to B across the structure must be the same independent of the path followed. The phase change of the current through each arm must be the same.

$$\delta_1 + \int_1 2e/\hbar (\mu_0 \lambda^2 j_1 + A) d\ell = \delta_2 + \int_2 2e/\hbar (\mu_0 \lambda^2 j_2 + A) d\ell \quad . \quad (3-3)$$

where  $\delta_1$  and  $\delta_2$  are the phases across the Josephson elements in each arm.

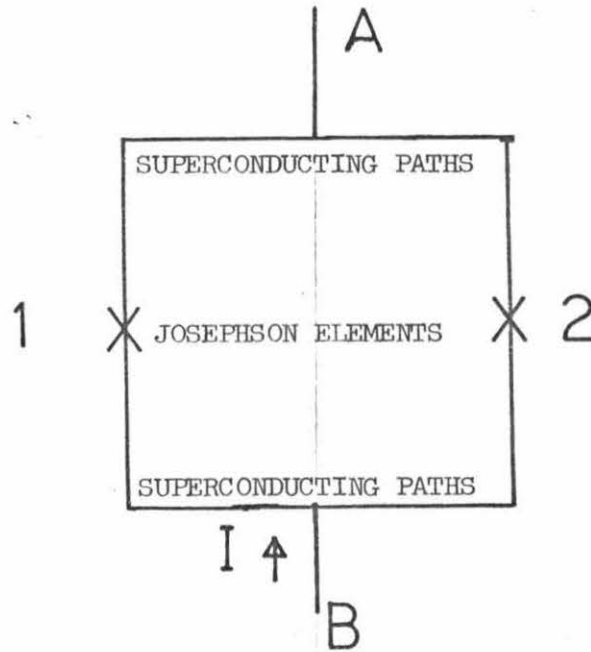


Fig. 3-1. Schematic representation of a generalized quantum interferometer. Interferometer consists of two Josephson elements, connected in parallel with superconducting paths. Current,  $I$ , flows from B to A, divided between paths 1 and 2. The Josephson elements involved may be of any physical realization, tunnel junctions, point contacts, or proximity effect bridges.

$$\delta_1 - \delta_2 = \oint \frac{2e}{\hbar} A d\ell + \int_a^b \frac{2e}{\hbar} \lambda^2 \mu_0 (j_1 - j_2) d\ell \quad (3-4)$$

The right hand side of this equation is the total angular momentum of the system. The line integral of  $A$  is just the enclosed magnetic flux.<sup>6</sup> If we consider the totally symmetric case the currents in each arm are equal ( $j_1 = j_2$ ) and the magnetic term is all that contributes to the phase difference.<sup>7</sup>

$$\delta_1 - \delta_2 = 2e/\hbar \phi$$

The total current through the interferometer is the sum of the currents in each branch

$$J = j_0 \left[ \sin \delta_1 + \sin \delta_2 \right] \quad (3-5)$$

$$= j_0 \left[ \sin \left( \delta_0 - \frac{e\phi}{\hbar} \right) + \sin \left( \delta_0 + \frac{e\phi}{\hbar} \right) \right] = 2j_0 \sin \delta_0 \left[ \cos \frac{e\phi}{\hbar} \right] \quad (3-6)$$

The maximum zero voltage current that the interferometer can support is

$$I_{\max} = 2I_0 \left| \cos \frac{\phi\pi}{\phi_0} \right| \quad (3-7)$$

where  $\phi_0$  is the flux quantum  $h/2e$ .<sup>8</sup> This well known relationship has been verified for interferometers formed of all varieties of Josephson elements,<sup>1,9,10</sup> including proximity effect bridges. In the zero

voltage case the above is a full description of the quantum interference phenomena.

If the Josephson elements in the interferometer are proximity effect bridges, the quantum interference effects persist at finite voltages, above the critical current. With a finite voltage across the bridges the supercurrent through each bridge oscillates at a frequency  $\omega = \frac{2eV}{\hbar}$ . Thus, the impedance of the superconducting paths between bridges must also be considered for quantum interference at finite voltages.

### 3.2 Quantum Interference at Finite Voltages

The quantum interference effects appearing at finite voltages for a quantum interferometer composed of proximity effect bridges are schematically illustrated in Fig. 3-2. The upper portion of this figure depicts the variation of critical current with magnetic flux through the interferometer for purposes of comparison. The lower portion of the figure shows the variation of dc voltage across the bridge as a function of magnetic flux. For each trace the total current through the interferometer is held constant. If the bias current is less than the critical current, no voltage is produced. If the bias current is above the critical current the voltage is modulated periodically with the flux through the interferometer. Thus, the voltage across the device is a function of bias current and flux through the interferometer  $V = V(I_B, \phi)$ . Another representation of this is given in Fig. 3-3. The trace in the  $V = 0$  plane is the critical current as a function of flux through the interferometer. The traces in the  $\phi = 0$  plane are current-voltage characteristics for the interferometer, which correspond to a critical current maximum and minimum, projected into the zero flux plane.

Fig. 3-2. Illustration of quantum interference effects at finite voltage. The uppermost trace is the critical current of the interferometer,  $I_c$ , as a function of magnetic flux through the interferometer. One period represents a change of one flux quantum,  $\phi_0$ .

The lower traces illustrate the variation of the time average voltage across the interferometer, at a constant bias current, as a function of magnetic flux through the interferometer. The parameter between traces is the bias current. For bias currents below the minimum critical current, A, no voltage is produced. For bias currents above the minimum critical current and below the maximum critical current, B, the voltage is finite for part of a cycle but zero for the remainder. For bias currents increasingly above the critical current, C, D, and E, the voltage is periodically modulated by the flux through the interferometer. As the bias current is increased the modulation becomes smaller and more nearly a sinusoidal function.

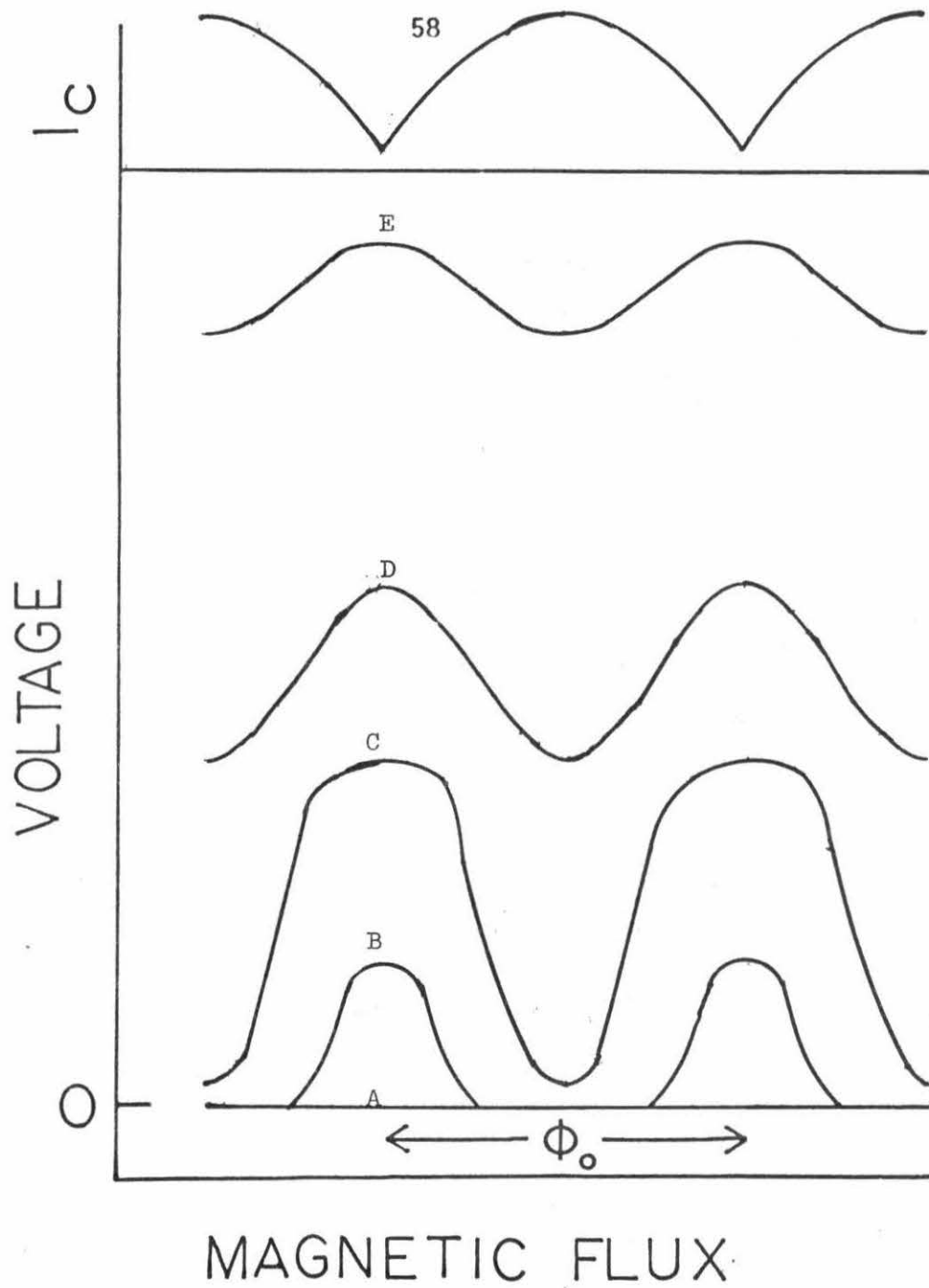
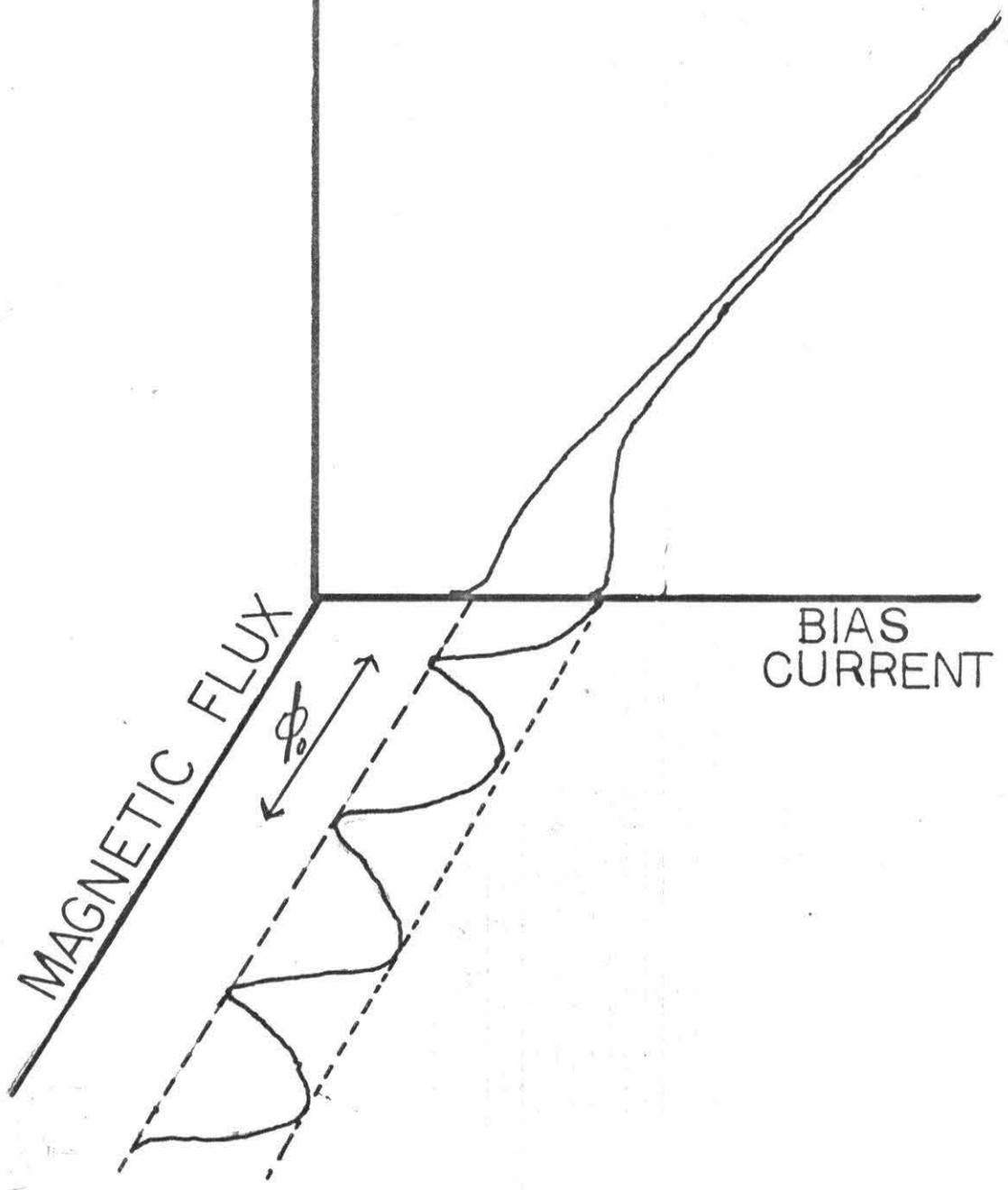


Fig. 3-2

Fig. 3-3. Illustration of quantum interference at finite voltages. The trace in the  $V = 0$  plane is the modulation of the critical current of the interferometer with magnetic flux through the interferometer. The traces in the  $\phi = 0$  plane are I-V characteristics projected into this plane. These are the I-V characteristics corresponding to a critical current maximum and a critical current minimum. The voltage across the interferometer varies both as a function of bias current  $I_B$  and magnetic flux  $\phi$ .

VOLTAGE



BIAS CURRENT

MAGNETIC FLUX

### 3.3 The Relationship of Dissipation to Quantum Interference at Finite Voltages

The interference effects at finite voltage have not previously been subjected to analysis. However, they may be approached through consideration of the power dissipated in the interferometer. At finite voltages each bridge, considered as an oscillator, may drive currents through the other. The currents lead to a change in dissipation with magnetic field resulting in a change in voltage across the device.

Let us consider in more detail a quantum interferometer composed of two proximity effect bridges connected in parallel by superconducting, thin film, paths. Most descriptions of the superconducting quantum interferometer are given in terms of current, as in the preceding sections. However, a common mode of operation for these devices is to bias at a constant current,  $I_B$ , which is larger than the critical current,  $I_C$ , and monitor the dc voltage  $\bar{V}$  developed across the device. The magnitude of this voltage is periodic with magnetic flux in the same manner as the zero voltage current. In this mode of operation, the magnitude of the variation of  $\bar{V}$  will ultimately determine the sensitivity of the device. Since we commonly operate our thin film devices in this mode we present a brief analysis outlining the dependence of the signal voltage,  $\delta\bar{V}$ , on the circuit parameters of the interferometer.

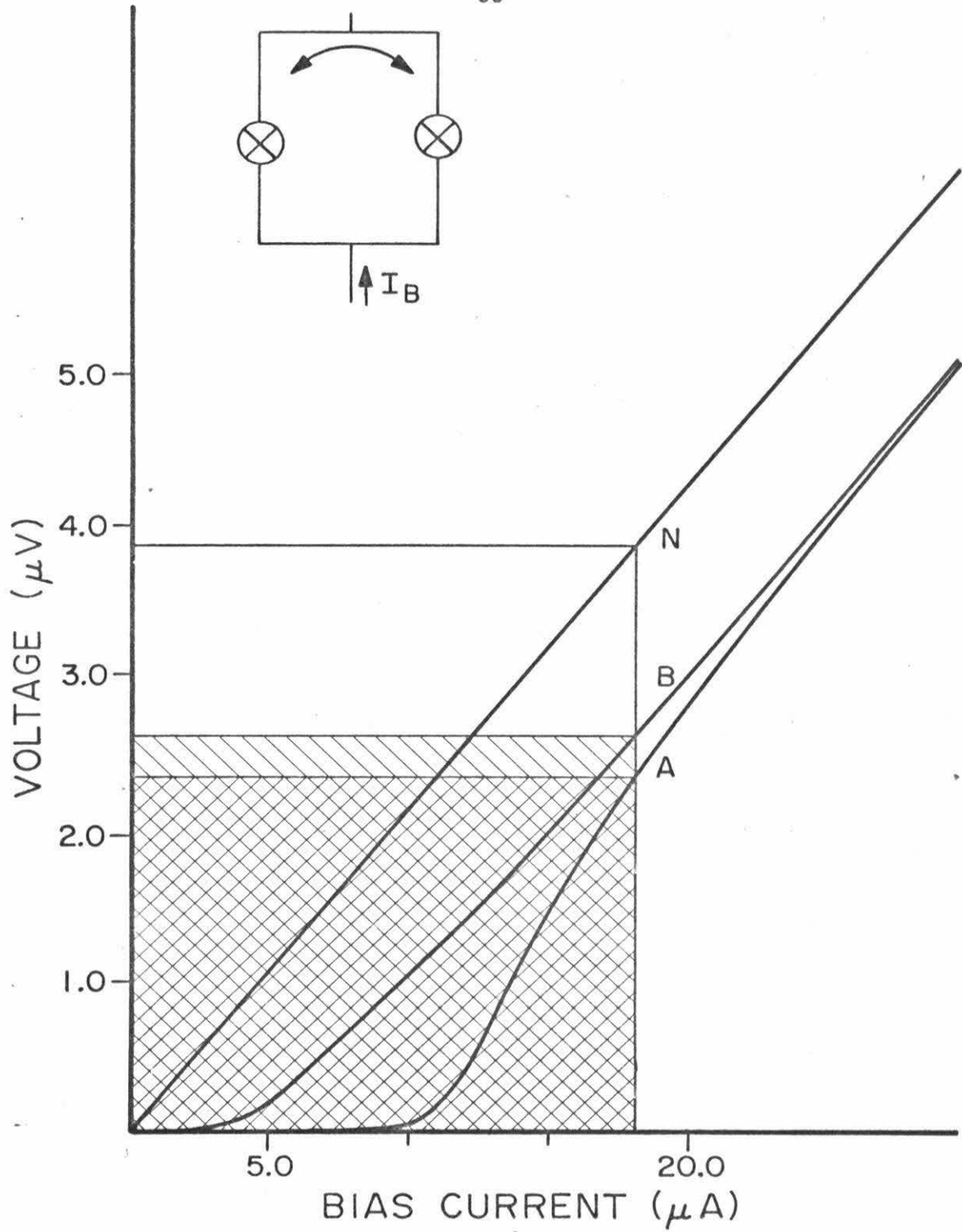
The origin of the dc voltage,  $\bar{V}$ , is in the dissipation within the interferometer, and the power so consumed is  $I_B\bar{V}$ . Thus any variation in dc voltage,  $\delta\bar{V}$ , arising in a current biased mode reflects a change in the dissipation. This relationship is shown in Fig. 3-4. It

Fig. 3-4. Measured I-V characteristics of a quantum interferometer. Curve N is the I-V characteristic when the interferometer's bridges are in the normal state, above their transition temperature. B corresponds to a critical current minimum; A to a critical current maxima. Both A and B are below the transition temperature. For a given bias current, 18  $\mu$ A. in this case, the power supplied to the interferometer is given by the large box with corner at N. The double hatched box with corner at A is the power supplied to the interferometer at a critical current maxima. The single hatched area with corners at A and B represents the increase in the dissipation of the interferometer caused by a change in the magnetic field of one half  $\phi_0$ . This change in dissipation is related to the maximum voltage modulation,  $\delta V$ , through the relation

$$\delta(\text{Diss}) = I_B \delta V$$

as discussed in the text.

Inset pictures source of the change in dissipation. Circulating ac supercurrents are driven through one bridge by the other.



It has been found<sup>11</sup> that the power dissipated in a proximity effect bridge can be approximated by the sum of a normal dissipation plus a dissipation due to the phase slip process. Each time the wave function collapses an amount of energy,  $I_S \phi_0$ , is lost.<sup>11</sup> This happens at the Josephson frequency and gives,  $\text{Diss} = I_S \phi_0 \nu = I_S \bar{V}$ , the product of the supercurrent and the time average voltage. In the mode of operation we consider, near the critical current, most of the dissipation is due to the supercurrent dissipation. At a constant bias current we can relate a change in dissipation to a change in voltage, the signal voltage,

$$\delta \bar{V} = I_b^{-1} \delta(\overline{I_C V}) \quad , \quad (3.8)$$

where the bar denotes time average. It should be noted that the voltage is a function of both bias current,  $I_B$ , and magnetic flux  $\phi$ , and thus the signal voltage is not necessarily related to the dynamic resistance  $R_d = \partial V / \partial I_B$  as measured on an I-V curve.

The equivalent circuit used to model the interferometer is shown in Fig. 3-5. Essentially, the two bridges are connected in parallel by an inductance,  $L$ . The devices have a well defined resistance which can be measured when the junctions are in their normal state. For an interferometer composed of two identical bridges the measured resistance is one half the resistance  $R$  in Fig. 3-5. The inductance  $L$ , is also a measurable quantity. (See Fig. 3-8 and Sec. 3.5).

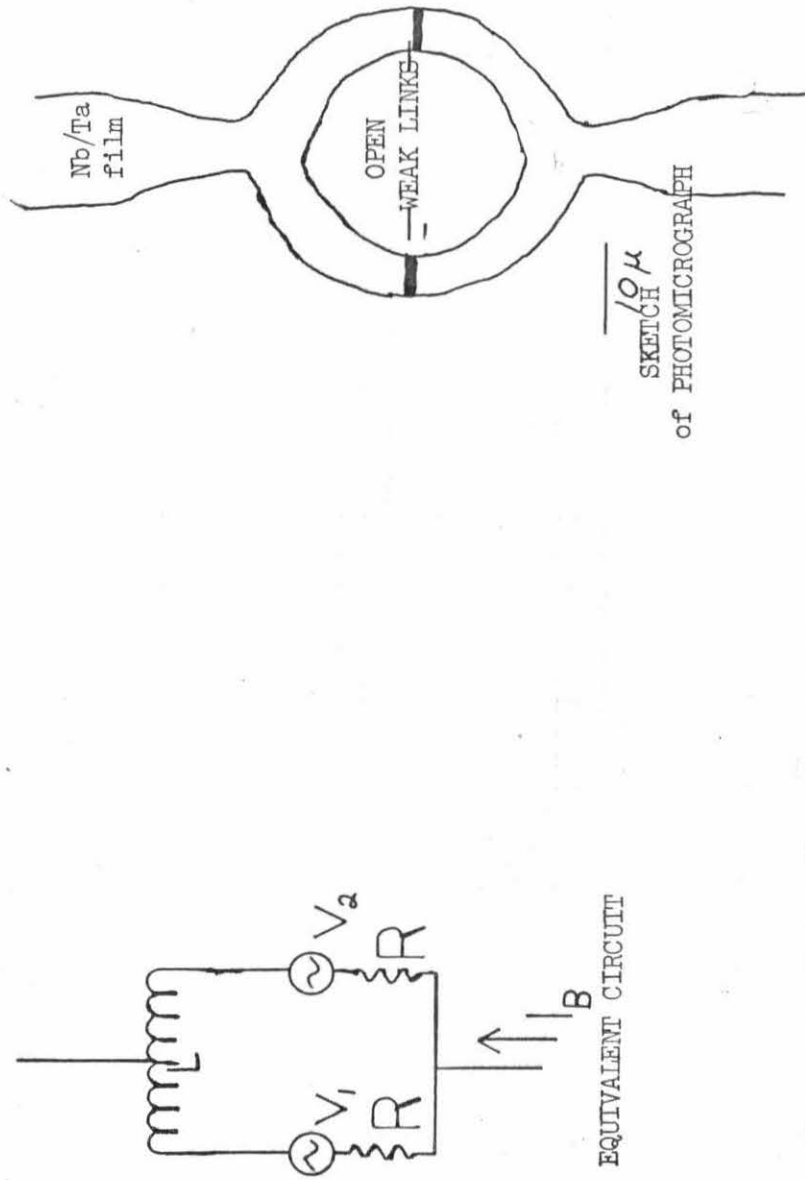


Fig. 3-5. Double bridge quantum interferometer. Sketch from photomicrograph and equivalent circuit for operation in finite voltage state.

In the equivalent circuit the bridges themselves can be considered as quantum voltage oscillators<sup>12</sup> of amplitude  $V = RI_c/2$  and frequency  $\omega = 2e\bar{V}/h$ .

The alternating currents driven by one oscillator through the other, lead to a change in the time average dissipation in the interferometer. This change in dissipation will depend upon the relative phase of the oscillators.

The phase gradient in the superconducting strips is set by the vector potential exactly as in the case of zero voltage quantum interference (see Sec. 3.1). Thus the effect of the magnetic flux in this model is to shift the relative phase of the two oscillators. This phase shift will cause a variation in the superconducting dissipation,  $I_2 \cdot v_1 + I_1 \cdot v_2$ , and result in a change in voltage,  $\delta\bar{V}$ , as discussed above.

To analyze the dependence of the maximum amplitude of  $\delta\bar{V}$  upon circuit parameters, bias current, and average voltage we consider the bias currents large compared to the critical current. For these bias conditions the oscillations of the bridges are nearly harmonic, justifying the use of harmonic circuit theory. Due to the extremely small physical size of the superconducting circuits, the characteristic dimensions will be much smaller than the wavelength of the oscillations for all frequencies of interest. Therefore we have utilized lumped circuit theory in the analysis that follows. That is, if  $\omega L \sim R$  then the circuits will be much smaller than the wavelength associated with  $\omega$ . For example  $R \approx 0.1 \Omega$  then for  $L \sim 10^{-11} \text{ h}$ ,  $\omega \sim 10^{10}/\text{sec}$ . If  $\ell$

is the characteristic dimension of the inductance,  $\ell \sim 10^{-5}$  m, which is much less than  $\lambda$  for frequencies up to 100 GHz.

By shifting the relative phase between the two oscillators, the dissipation due to the rf circulating currents in the interferometer is modulated. This dissipation is  $I_i V_C$ , where  $I_i$  is the rf circulating current induced around the interferometer and  $V_C$  is the rf voltage around the circuit, and it ranges in amplitude from zero when the oscillators are in phase, to a maximum value when the oscillators are out of phase. The maximum out of phase rf voltage around circuit,  $V_m$ , is the sum of the rf voltages of the two oscillators. The maximum current  $I_i$  can be estimated from the equivalent circuit to be  $I_i = V_m [2R + i\omega L]^{-1}$ . Introducing the flux quantum  $\phi_0$ , this induced circulating current can be rewritten as,

$$I_i = \frac{\phi_0}{L} \frac{V_m}{[2R\phi_0/L + 2\pi i \bar{V}]} \quad (3.9)$$

The maximum change in dissipation due to these circulating supercurrents occurs upon going from the in-phase to out of phase saturation.

$$\delta P_{\max} = \left| \frac{4 v_1 \cdot v_2}{\frac{2R\phi_0}{L} + 2\pi i \bar{V}} \right| \quad (3.10)$$

The voltage oscillators have experimentally been found to have the form<sup>12</sup>

$$v_1 = v_2 = \frac{I_C R}{2} \left( 1 + \cos 2e/\hbar \int v dt \right) \quad (3.11)$$

After substituting for  $v_1$  and  $v_2$  we rationalize the expression and take the time average. We obtain an expression for the maximum modulation of the dissipated power, in the high bias power limit, i.e.  $\omega L \gg 2R$

$$\delta P_C = 3/2 (I_C R)^2 \phi_0 / \bar{V} 2\pi L \quad (3.11)$$

This implies a voltage modulation

$$|\delta \bar{V}| = \frac{|\delta P_C|}{I_B} = \frac{1}{I_B \bar{V}} 3/2 \left( \frac{R \phi_0}{2\pi L} \right) (I_C^2 R) \quad (3.12)$$

This expression contains no free parameters; all quantities are measurable.

The high power asymptotic limit was taken to simplify the calculation. The harmonic expansion of the oscillating voltage as given in Appendix A is

$$v(t) = \bar{V} \left( 1 + 2 \sum_{m=1}^{\infty} (-1)^m \left( \frac{2\bar{V}}{I_C R} - \frac{2I}{I_C} + 1 \right)^m \cos m \frac{\bar{V}t}{\phi_0} \right) \quad (3.13)$$

With increasing bias power,  $I_B \bar{V}$ , the harmonic content of the oscillations drops off. Near the critical current the harmonic content is very large and the above analysis no longer applies. This prevents  $\delta \bar{V}$  from becoming

as large as predicted for low bias powers. At low voltages ( $V < I_c R$ ) the amplitude of the oscillating voltage becomes limited by that of the dc voltage and the magnitude of the voltage difference expected thereby decreases.

### 3.4 Experimental Evidence

Experiments to confirm the maximum separation in the I-V characteristics calculated in the previous section have been performed. The maximum separation,  $\overline{\Delta V}$ , may be measured directly from the difference in the I-V characteristics. The maximum such difference is seen to occur for the I-V characteristics associated with critical current maxima and minima. The separation between these two I-V characteristics at a given bias current is just the quantity,  $|\delta V|$ , we desire. This method, while straightforward, has the disadvantage that the resultant quantity is the difference between two large numbers increasing the error. An alternative approach is to modulate the magnetic field and use standard lock-in techniques to detect the alternating voltage produced. If the quantity,  $dV/d\phi$ , is plotted against total time average flux for a constant bias current then the integral between zero crossings also gives  $|\delta V|$ . Both methods give the same dependence on  $(I_B \overline{V})^{-1}$ . Figure 3-6(a) presents data from two interferometers, obtained from the I-V traces.

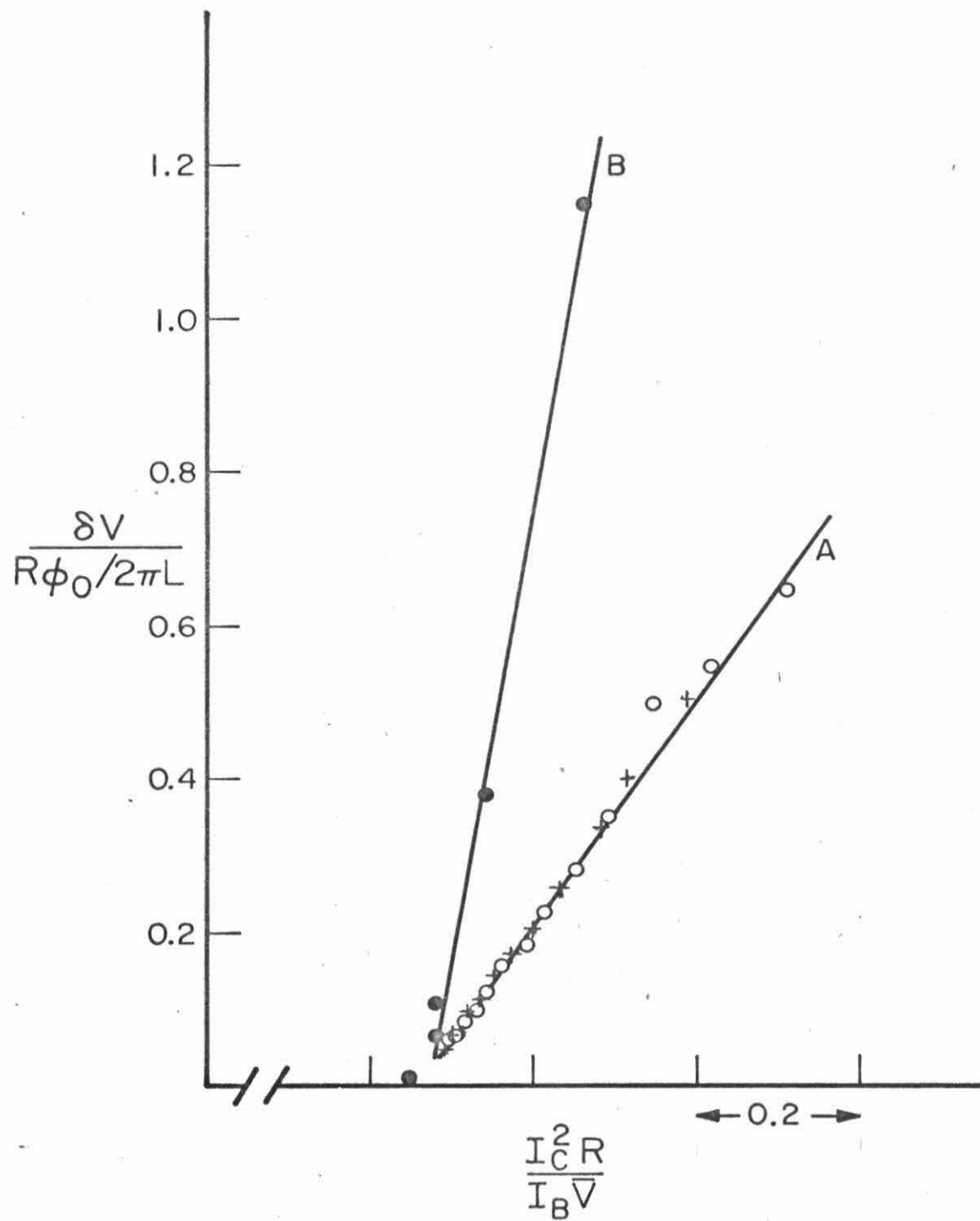
Equation 3.12 indicates a natural set of reduced units for the quantity  $\delta V$ .

$$|\delta \overline{V}| = \frac{|\delta P_c|}{I_B} = \frac{1}{I_B \overline{V}} \frac{3}{2} \left( \frac{R\phi_0}{2\pi L} \right) (I_c^2 R) \quad (3.12)$$

Fig. 3-6.  $|\delta V|$  as a function of  $(I_B \bar{V})^{-1}$  plotted in reduced

units  $|\delta V| \frac{R\phi_0}{2\pi L}^{-1}$  and  $\frac{I_c^2}{I_B \bar{V}}$ . Data (trace a) are for two

interferometers at different critical currents. Data obtained from direct I-V measurements. Line a has predicted slope 3/2. Line b has slope 6 as predicted for a four junction interferometer. Both interferometers shown in trace a are plotted from the same origin. The break in the horizontal axis is to facilitate comparison between a and b.



The data are plotted in reduced units

$$|\delta V|/R\phi_0/2\pi L$$

and

$$\frac{I_C^2 R}{I_B \bar{V}}$$

to facilitate comparisons between devices. The predicted values of the slope of the straight line, in these units, is just 3/2, in excellent agreement with the observed slope. The magnitudes in this zero-parameter fit, generally agree to within a factor of 2. The excellent agreement with this simple model justifies our use of lumped circuit theory and our use of the single equivalent circuit shown in Fig. 3-5.

A special interferometer with the geometry and equivalent circuit shown in Fig. 3-7 was constructed as an additional test of this model. It is an interferometer with two bridges ( $\sim 2\mu$  spacing) in each arm. This geometry allows us to investigate changes in the oscillator strength as well as changes in the parameters of the equivalent circuit. If two bridges are placed in series and if they are nearly identical it is possible for them to interact and synchronize their oscillations. This interaction depends upon the separation of the bridges. For a separation of  $2\mu$  the interaction is weak enough that differences in the bridges may easily disrupt the synchronization.<sup>13</sup> The special interferometer shown in Fig. 3-7 was constructed in such a way that bridges A and C in Fig. 3-7b, one in each arm of the

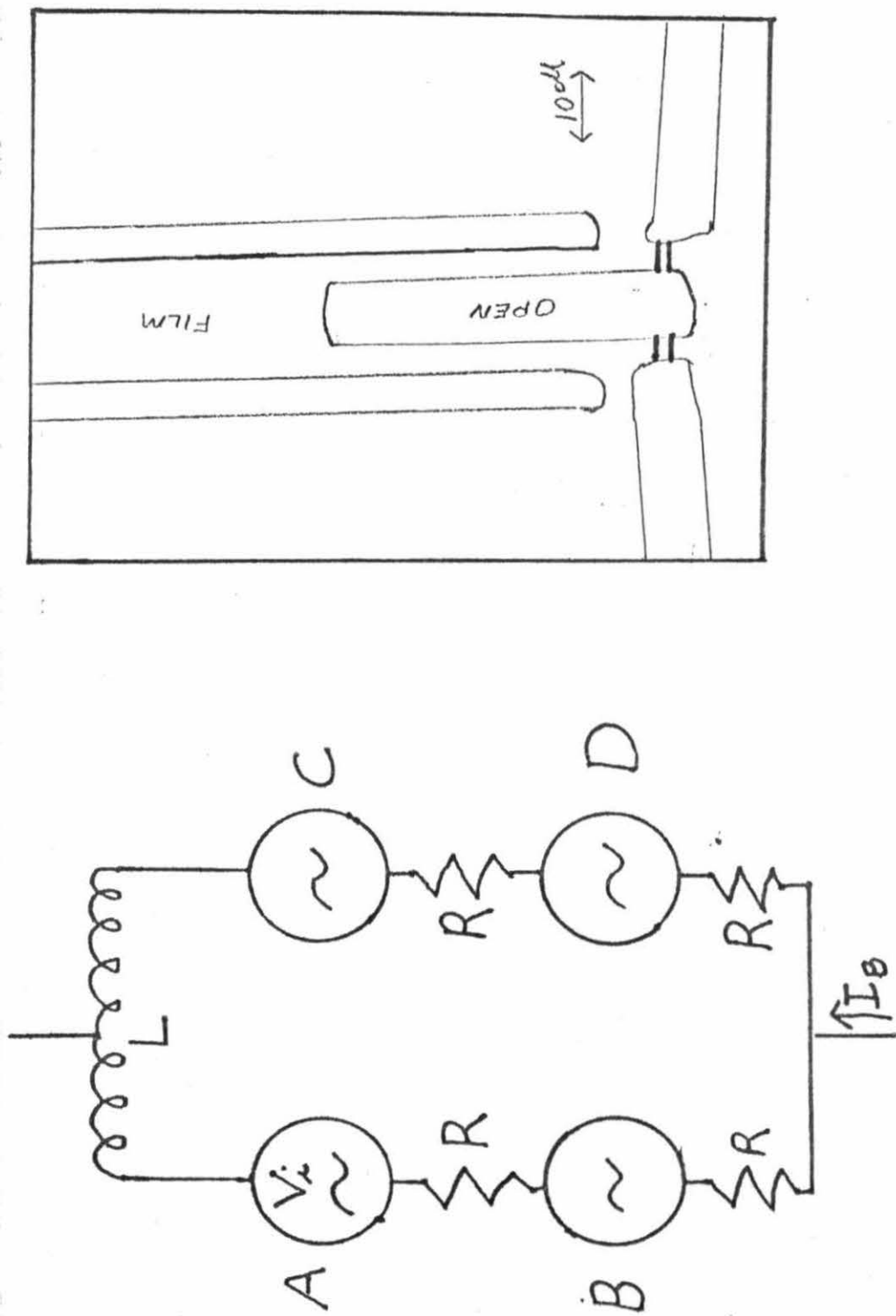


Fig. 3-7. The special four junction interferometer constructed to test the effects of changes in oscillator strengths. On the left is the equivalent circuit for operation in the finite voltage state. On the right is a sketch from a photomicrograph.

interferometer, will be identical as will bridges B and D, but there may be differences between the pairs, that is between A and B and C and D.

The above analysis of the operation of a quantum interferometer at finite voltages must be modified slightly for an interferometer with two bridges in each path. The power dissipated in the circuit will be increased, and the voltage across each bridge, and thus the frequency of oscillation will be reduced by approximately a factor of two.

If the oscillations in each of the bridges in each arm of the interferometer are at the same frequency then the oscillator strengths in our previous calculations are increased by a factor of two increasing the dissipation by a factor of four. The voltage across each bridge is half the total voltage across the interferometer. In the asymptotic limit, the effect upon the slope of the line predicted by Eq. 3.12 is to increase it by a factor of eight

$$|\delta V| = 8 \cdot 3/2 \left( \frac{R\phi_0}{2\pi L} \right) \frac{I_C^2 R}{I_B V} \quad (3-14)$$

If the two bridges in each are of slightly different resistances then they will operate at slightly different voltages, and thus at slightly different frequencies. The increase in dissipation in this case is limited to a factor of 2 as the circulating currents will only dissipate in an oscillator of the same frequency. The operating voltage of each bridge will again be approximately half the voltage

across the interferometer. The slope of  $\delta V$  v/s  $1/I_B \bar{V}$  in high current limit will again be modified, this time by a factor of 4. Equation (3-12) becomes

$$|\delta V| = 4 \cdot 3/2 \left( \frac{R\phi_0}{2\pi L} \right) \frac{I_C^2 R}{I_B \bar{V}} \quad (3-15)$$

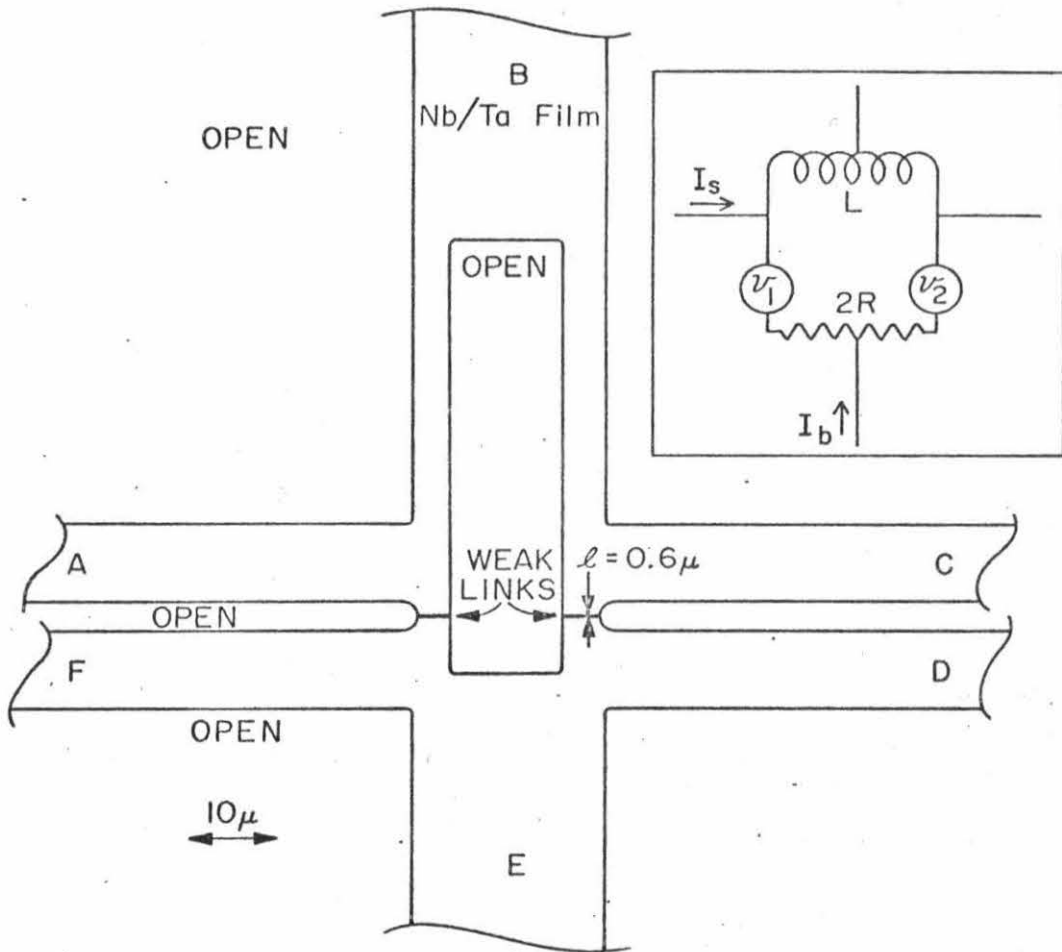
Therefore the slope of the linear dependence of  $\delta V$  on  $(I_B \cdot \bar{V})^{-1}$  provides a test of the coherence of the oscillators in each arm of the interferometer. If the oscillators are synchronized the slope will be increased from 3/2 to 12, a factor of 8. If the oscillators are incoherent the slope will increase from 3/2 to 6, a factor of 4. The evidence, given in Fig. 3-6b, indicates that for this interferometer the data exhibit a slope of six as expected for incoherent oscillators.

### 3.5 Use of Quantum Interferometer as a Galvanometer

We have seen that the quantum interferometer with proximity effect bridges as the active elements, produces a voltage signal periodic in the magnetic flux through the interferometer. This signal has a period of  $\phi_0 = h/2e$ . To illustrate the size of a flux quantum consider the earth's field threading a hole of 3 micron radius produces one flux quantum. The small size of the flux quantum, which may easily be further subdivided by at least a factor of  $10^3$ ,<sup>14</sup> makes these devices extremely attractive for magnetic field device applications. In particular one may measure the magnetic flux produced by a current. The current  $I_s$  produces flux through the interferometer given by  $I_s M = \phi$  where  $M$  is the mutual inductance between current path and the interferometer. This signal current,  $I_s$ , produces magnetic flux in the interferometer which modulates the critical current and thereby, the voltage across the bridge.

By incorporating an integral, thin film, superconducting current path into the interferometer, as shown in Fig. 3-8, one forms a mutual inductance,  $M$ , of the same magnitude as the interferometer inductance  $L$  thus producing a sensitive galvanometer, composed entirely of thin films. We have found experimentally that the best coupling between  $I_s$ , the signal current, and the interferometer requires a large hole and a narrow signal path as shown. This geometry allows a determination of the interferometer inductance through the relation  $I_{s_0} L = \phi_0$  where  $I_{s_0}$  is the signal current necessary to modulate the critical current through one period and we

Fig. 3-8. Schematic representation of the galvanometer element. The signal current,  $I_s$ , flows from A to C; the bias current,  $I_b$  may be fed from E to B in the symmetric case, or from F to A in the asymmetric case. The voltage produced in the quantum interferometer is monitored between C and D. Inset shows equivalent circuit considered in text.



have made the approximation (excellent for this geometry)  $L = M$ . Thus the galvanometer has a built-in, very accurate calibration point,  $I_{s_0}$ .

The voltage across the galvanometer,  $\bar{V} = V(I_b, I_s)$ , for a given critical current is dependent on the bias current  $I_b$  and the dc value of the signal current (which determined the relative phase of the oscillators). A small change in the voltage may be produced by a change in either  $I_s$  or  $I_b$ .

$$dv = \left. \frac{\partial v}{\partial I_s} \right) I_b dI_s + \left. \frac{\partial v}{\partial I_b} \right) I_s dI_b \quad (3.15)$$

The quantity  $\left. \frac{\partial v}{\partial I_b} \right) I_s$  is the dynamic resistance,  $R_d$ , and we define  $\left. \frac{\partial v}{\partial I_s} \right) I_b$  as the response,  $r$ , of the galvanometer. Both the response and the dynamic resistance are functions of  $I_s$  and  $I_b$ . In operation, the galvanometer is biased with  $I_b$  and  $I_s$  to that portion of the voltage surface having the maximum value of the response. Biasing to this point yields the greatest sensitivity. As a specific example, a galvanometer with  $R = 0.65 \Omega$  and  $L = 7.7 \times 10^{-11} \text{ h}$ , produces a maximum response of  $380 \text{ m}\Omega$ . Our voltage sensitivity of  $1 \text{ nv}$  in room temperature electronics implies a current sensitivity of  $2.6 \times 10^{-9} \text{ amps}$  for this device. This corresponds to a resolution of  $10^{-4} \phi_0$ . This resolution, quite respectable in itself, is not set by a fundamental limit in the galvanometer but rather by the noise in the room temperature electronics. Use of the LHe-cooled transformer system described in detail in Chapter 4 extends the capabilities of the device to the limit

set by the fundamental voltage fluctuations in the device  $\sim 10^{-21} \text{ V}^2/\text{Hz}$ . This implies a current sensitivity of  $8 \times 10^{-11} \text{ A}$  or  $5 \times 10^{-6} \phi_0$  with a one second time constant.

It should also be noted that the input to this device is entirely superconducting and, therefore, lossless. The input impedance is entirely inductive and set by the inductance of the signal current path  $\sim 10^{-10} \text{ h}$ . This thin film device is a true galvanometer with a low impedance input which is entirely inductive. Greater current sensitivity is available in commercial electrometers but only at the cost of a very high input impedance. The galvanometer described above, offers the intriguing possibility of being fabricated as an integral portion of a low temperature thin film experiment. A detailed plot of the response  $\frac{dV}{dI_S}$ , as a function of  $I_S$  is given in Fig. 3-9. The maximum response occurs for bias currents just larger than the maximum critical current. These data were taken from a galvanometer with  $R=0.65\Omega$  and  $L=7.7 \times 10^{-11} \text{ h}$ .

In the cases considered thus far, the critical current is a symmetric function of the signal current. If however the characteristic is not symmetric then a small change in signal current can give rise to a large change in critical currents, as illustrated in Fig. 3-11. Various techniques have been proposed<sup>15,16,17</sup> to cause the critical current to vary asymmetrically with the signal current. These generally involve an asymmetric bias current geometry, for example biasing between leads A & F in Fig. 3-8. An asymmetric current bias will cause a net flux through the interferometer. As the signal current changes this changes the critical current, and if the bias current is kept equal

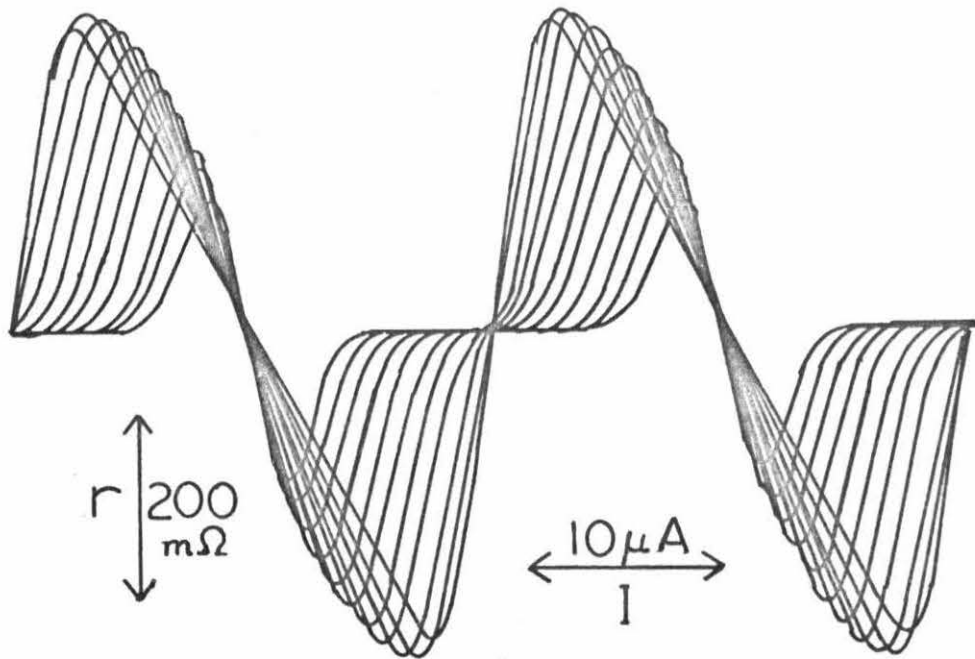
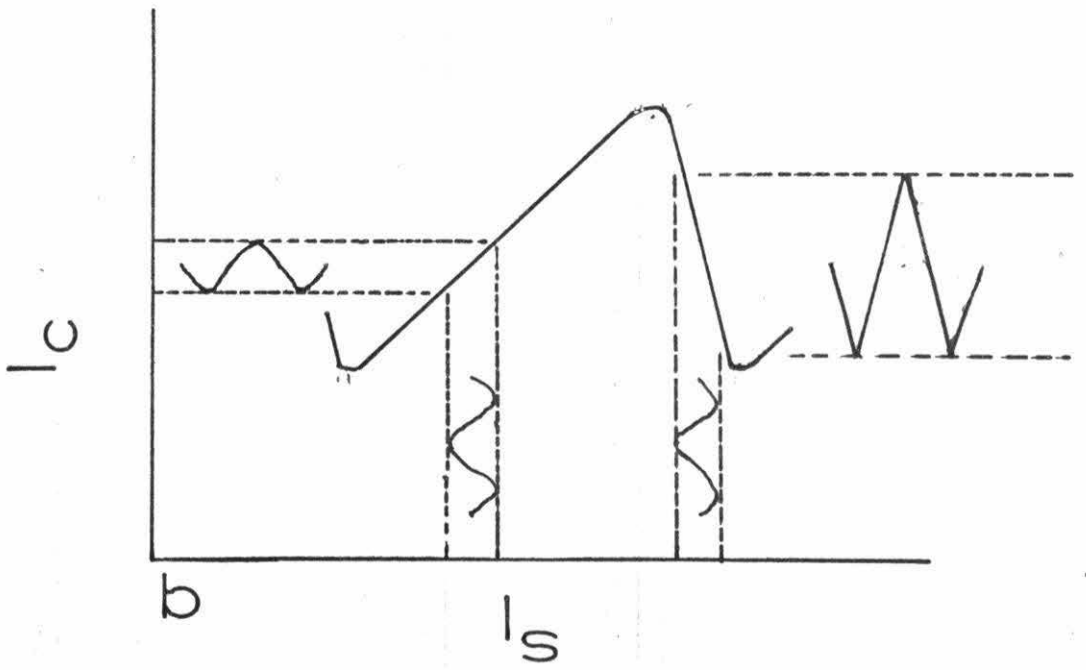
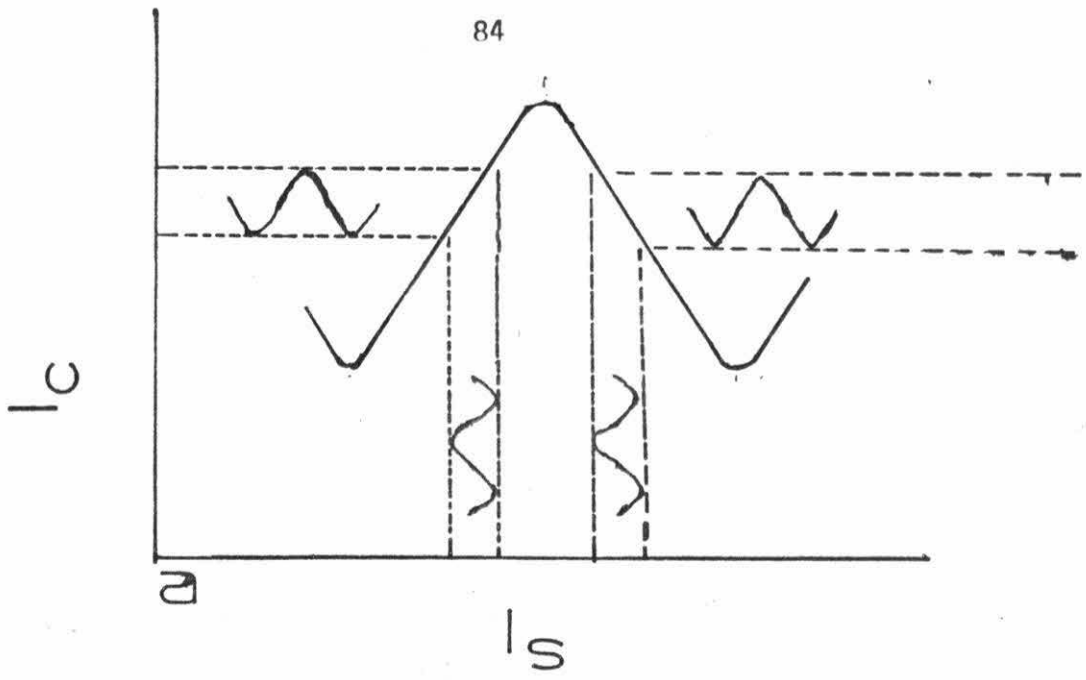


Fig. 3-9. Galvanometer response,  $\left. \frac{\partial V}{\partial I_S} \right|_{I_B}$ , as a function of dc signal current,  $I_S$ . Parameter between the curves is bias current in microampere steps. Galvanometer had  $R = 0.65\Omega$  and  $L = 7.7 \times 10^{-11} \text{h}$

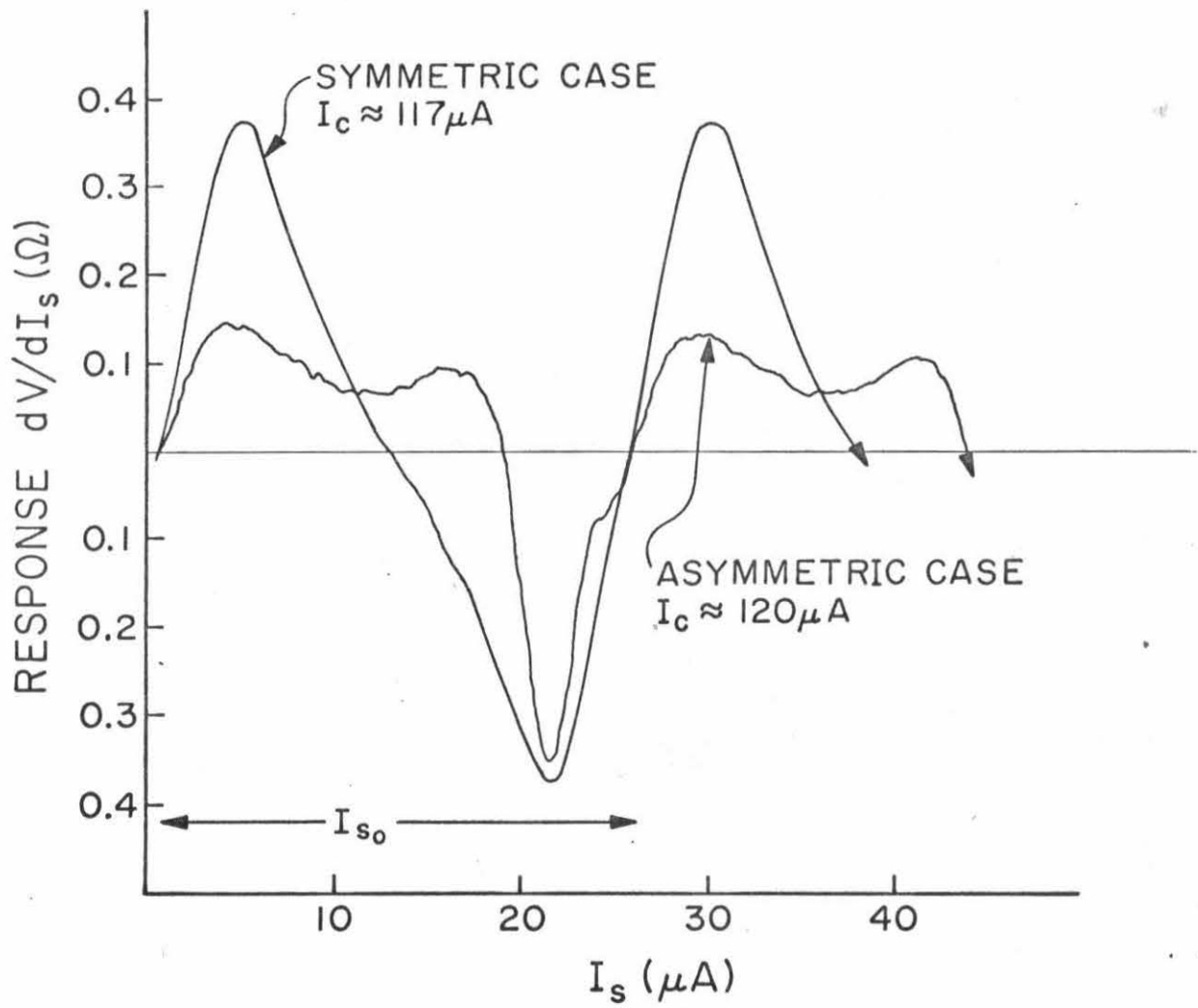
Fig. 3-11. Schematic illustration of asymmetry in the  $I_C$  v/s  $I_S$  characteristics giving rise to current gain. Fig. 3-11a shows the symmetric case; a small change in  $I_S$  produces a small change in the critical current  $I_C$ . In the asymmetric case, 3-11b, on the steep portion of the characteristic a small change in  $I_S$  gives a large change in  $I_C$  and thus can result in current gain. On the opposite portion of the characteristic a small change in  $I_S$  gives rise to a yet smaller change in  $I_C$ .



to the critical current, the flux it contributes will also change, reinforcing or detracting from the effect of the signal current. On that part of the  $I_C-I_S$  characteristic where the effects add, the quantity  $\frac{dI_C}{dI_S}$  can be very large, leading to a large current gain as reported by Clarke.<sup>15</sup> That is, a small change in signal current will induce a large change in critical current. These devices also show such current gain with a maximum value of  $dI_C/dI_S \approx 5$ .

This current gain does not result in an increase in the response of the galvanometer operated in a current biased, finite voltage mode. In this case the total current through the device is fixed and the change of flux produced by a change in critical current is small and does not produce a large increase in response. Figure 3-10 shows the maximum response in the asymmetric and symmetric cases for the same galvanometer element. The maximum response for a given temperature is found by measuring the response,  $r$ , and the dynamic resistance,  $R_d$ , as a function of  $I_S$  with  $I_b$  as a parameter. Apparently, the voltage surface  $V(I_S, I_b)$  varies with  $I_S$  in such a way as to limit the maximum response to approximately the levels in the symmetric case.

Fig. 3-10. Variation of galvanometer response with dc signal current in symmetric and asymmetric current bias cases. Traces shown are those, for a given temperature, yielding the largest value of the response.



### 3.6 Inclusion of the Quantum Galvanometer into a Superconducting Transformer

The maximum response of the galvanometer element in conjunction with the minimum detectable voltage sets a limit upon the minimum current the galvanometer element will detect.  $I_{s_{min}} = V_{min}/r$ , where  $r$  is the responsivity of the galvanometer. Frequently the minimum detectable voltage is set by room temperature electronics rather than by intrinsic noise levels in the galvanometer element. Since the input to the galvanometer is entirely superconducting, the galvanometer element is ideal for inclusion in the secondary of a superconducting flux transformer. Under ideal conditions, the flux transformer will provide a current gain given by the turns ratio,  $n$ , of the transformer.<sup>18</sup> This passive current gain raises the signal current to a level higher than the minimum detectable current of the galvanometer element.

The superconducting transformer, due to its zero resistance to current flow, will act to oppose flux changes through the secondary even down to zero frequency. The secondary, a single turn of superconducting material, is conveniently fabricated from the same thin film parent material as the galvanometer element itself. The geometry of the secondary is illustrated in Fig. 3-12. The current in the primary generates flux which would cut the secondary if it were not a closed superconducting loop. This flux is given by  $\phi_s = IM$  where  $M$  is the mutual inductance between primary and secondary. The shielding currents in the secondary generate an equal and opposite

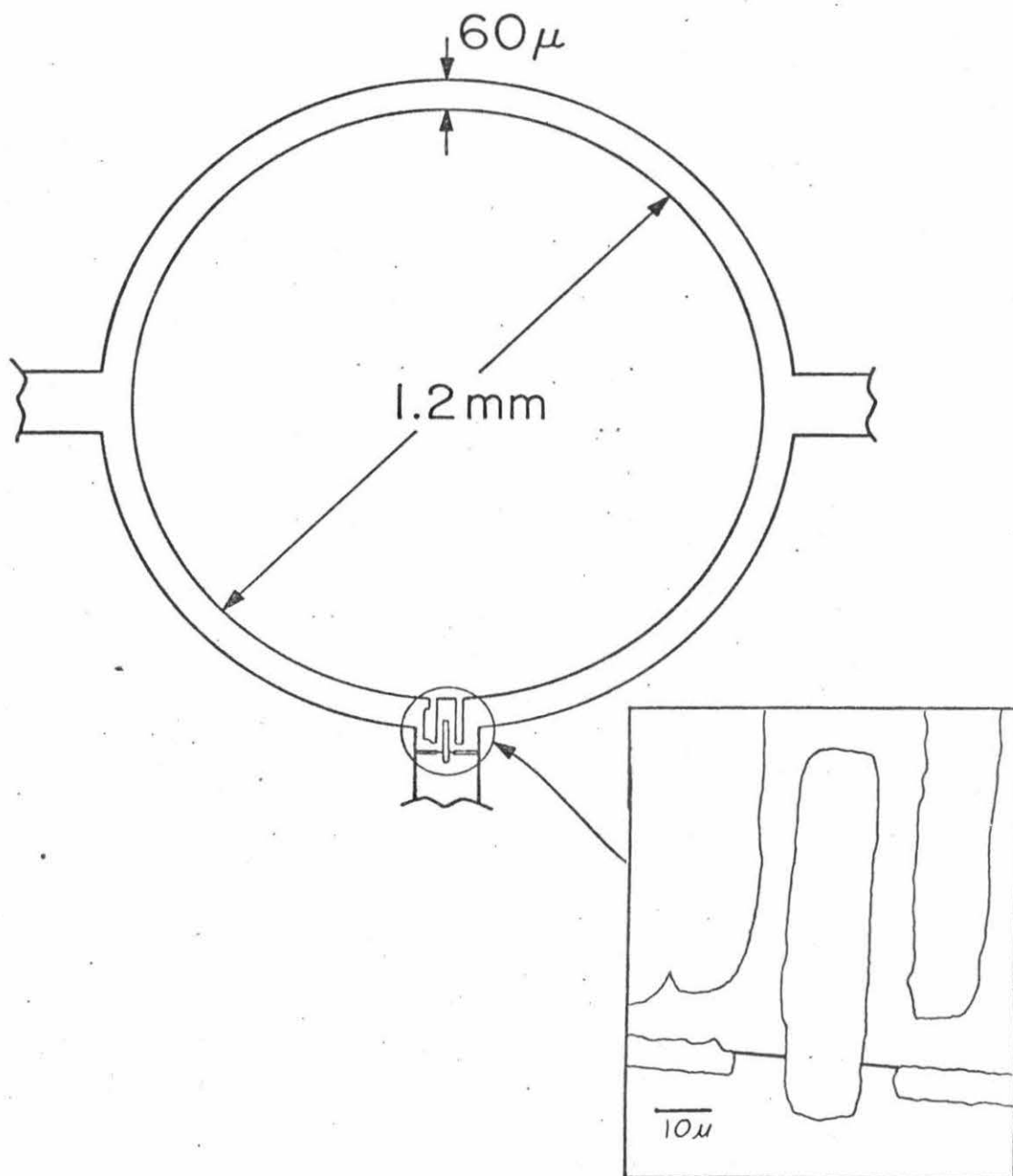


Fig. 3-12. Flat thin film superconducting transformer secondary with galvanometer element included. See text for details of operation. Leads to sides and bottom are for dc bias of galvanometer.

flux to maintain a net zero flux through the secondary.  $0 = \phi_s - I_s L_s$  where  $I_s$  is the inductance of the ring. This yields the shielding currents

$$I_s = \frac{IM}{L_s}$$

These shielding currents produce a flux through the galvanometer element given by  $\phi_g = I_s L$  where  $L$  is the mutual inductance of the signal path and the galvanometer element. Therefore, the flux through the galvanometer element is  $\phi_g = IL \frac{M}{L_s}$ . Since without the transformer the flux generated by the signal current would be just  $\phi = IL$ , one may generate more flux through the galvanometer element, and thus a larger signal, with the same input current, if  $M/L_s$  is greater than unity. The primary-secondary mutual inductance is given by  $M = k \sqrt{L_p L_s}$  where  $L_p$  and  $L_s$  are the self inductances of primary and secondary and  $k$  is a coupling constant ranging from zero to unity. The constant  $k$  is the ratio of the realized mutual inductance to the maximum possible value  $M = \sqrt{L_s L_p}$ . The gain of the transformer, that is, the ratio of the currents needed to produce the same galvanometer signal with and without the transformer is

$$G = \frac{I_{\text{no trans}}}{I_{\text{trans}}} = \frac{M}{L_s} = k \sqrt{L_p/L_s}$$

as  $k$  approaches unity the primary and secondary must be nearly the same physical configuration which yields,  $G = n$ , where  $n$  is the turns ratio as predicted. Of course, lack of perfect coupling will limit the gain achieved in any real configuration. The maximum value of coupling attained was  $k = 0.05$  yielding a gain of 2 for the flat ring system.

The behavior of the secondary may be investigated independently of the coupling between primary and secondary. If the secondary and galvanometer element are placed in a uniform magnetic field,  $B$ , then the flux necessary to produce one flux quantum in the galvanometer element is just

$$B_{or} = \frac{\phi_0 L_s}{A_r L}$$

where  $\phi_0$  is the flux quantum  $h/2e$ ,  $A_r$  is the area of the secondary ring,  $L_s$  the inductance of the secondary, and  $L$  the mutual inductance between secondary current path and the galvanometer element. The field necessary to produce a flux quantum in the galvanometer element without the secondary is  $B_0 = \phi_0/A_g$  where  $A_g$  is the enclosed area of the galvanometer element. The ratio of these two fields is given by

$$B_{or}/B_0 = \frac{L_s A_g}{A_r L}$$

For a secondary ring 1.2 mm in inner diameter, 60  $\mu$  wide,  $L_s$  is approximately  $3 \times 10^{-9}$  h. The particular galvanometer element in this ring had  $L = 5 \times 10^{-11}$  and  $A_g = 1 \times 10^{-9}$  m<sup>2</sup>. These yield an expected value for  $B_{or}/B_0$  of  $5.3 \times 10^{-2}$ . The experimentally measured value of this quantity is  $6.7 \times 10^{-2}$ . The excellent agreement indicates that the combination of superconducting secondary and galvanometer element transfers the magnetic flux from ring to galvanometer as calculated above.

Theoretically one could achieve infinite gain with such a superconducting transformer, however in any real system the coupling constant will diminish as the number of primary turns is increased thus

limiting the gain that may be achieved. In the case of the flat ring the very low coupling constant attained is due to the essentially zero axial extent of such a ring and the finite thickness of the substrate. These limitations on the coupling of primary to secondary encountered with the flat ring may be circumvented through a simple change of geometry that has been demonstrated to yield a high value of the coupling. Wang<sup>19</sup> has investigated the coupling of cylindrical thin film rings on rods to a primary coil wound tightly upon it. In the case of a 3 mm rod and a one hundred turn, single layer primary wound tightly (spacing less than  $25\mu$ ) upon the rod, he has obtained a value of the coupling constant,  $k$ , of 0.97. This tight coupling makes possible a dramatic increase, by nearly the number of turns in the primary, in the sensitivity of the quantum galvanometer element. The galvanometer, fabricated from the thin film material on the rod, would respond to the shielding currents in the cylindrical secondary in the same manner as was observed in the flat secondary ring described above. The precise geometry and turns ratio needed would depend upon the final desired experimental application but would resemble that given in Fig. 3-13.

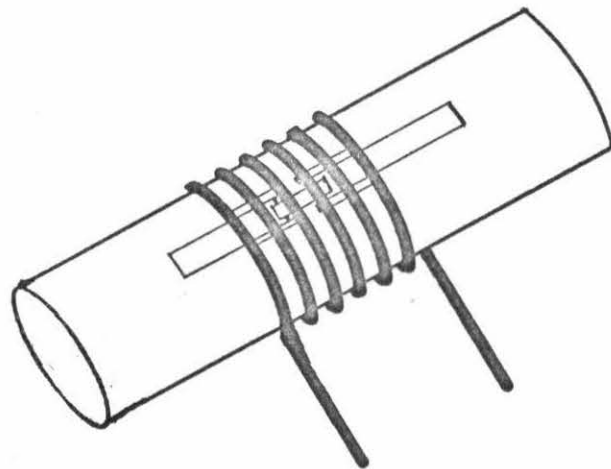
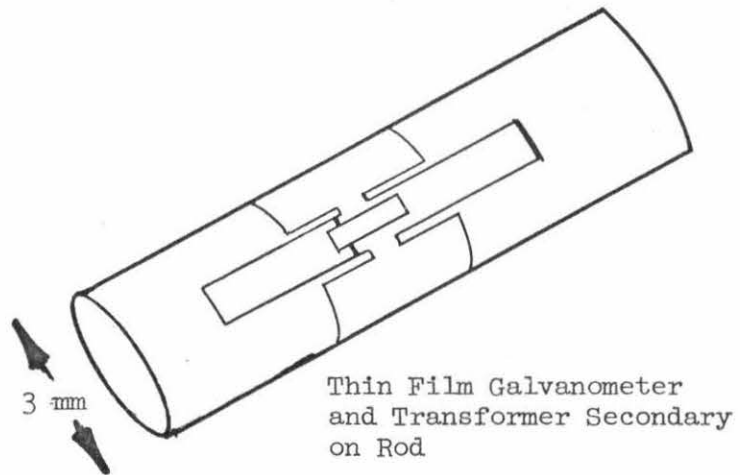


Fig. 3-13

### 3.7 Summary

We have investigated the behavior of a quantum interferometer composed of two proximity effect bridges connected in parallel with thin superconducting films. In addition to the usual quantum interference effects at zero voltage, these interferometers exhibit quantum interference effects when the proximity effect bridges are in the voltage sustaining state. The time average voltage across the interferometer is periodically modulated by the flux through the interferometer. As with the modulation of the critical current, the period is the flux quantum  $\phi_0$ .

In the voltage sustaining state, the proximity effect bridges behave as quantum oscillators whose frequency depends upon the time average voltage across them. The relative phase of the two oscillators in the interferometer depends upon the flux through the interferometer. The relative phase of the oscillators determines the magnitude of the circulating currents, and thus, the magnitude of the internal dissipation in the device.

We have found the modulation of the dc voltage across the device to be consistent with a change in internal dissipation of the device due to circulating currents. The dependence of this voltage modulation upon bias power and upon parameters of the interferometer has been found to be in accord with a simple lumped circuit model of the device, which treats the bridge as voltage oscillator whose frequency depends upon the time average voltage across the device.

We have also investigated utilizing such an interferometer as a sensitive galvanometer. The galvanometer has a maximum current sensitivity of  $\sim 10^{-10}$  amps. The galvanometer is completely composed of thin films and is of typical dimensions  $\sim 100 \mu$ , thus presenting an excellent choice for inclusion in superconductivity microcircuitry.

We have also investigated the possibility of extending the current sensitivity of this device through inclusion in the secondary of a superconducting flux transformer. We have found it is indeed possible to do so with the exact value of gain so achieved depending upon the conditions imposed by the final experimental applications.

NOISE MEASUREMENTS IN PROXIMITY EFFECT BRIDGES

4.1 Introduction

Many device applications of quantum interference are possible due to the precise, yet sensitive nature of the phenomena involved. Whatever the realization of the quantum interference element, the fluctuations or noise in its electrical parameters will ultimately determine the sensitivity limits of any device utilizing these elements.

The fluctuations in a proximity effect bridge whether in the voltage across the bridge or in the current through it will limit the device in two separate ways. For the sake of correctness, consider the voltage fluctuation. The fluctuations will, of course, limit the accuracy to which one may measure the voltage across the device. However, the voltage fluctuations will affect the bridge in a more fundamental manner. The fluctuations in the voltage will result directly in fluctuations of the phase difference across the bridge, thus affecting the quantum relations governing its performance.

Voltage or current fluctuations within a given bandwidth will limit any device dependent upon a low frequency measurement of the critical current of the bridge or the voltage across it. This effect would limit the sensitivity of a double bridge interferometer used, for example, as a galvanometer as described in the preceding chapter. The operation of a bolometer utilizing a bridge as a temperature sensor<sup>1</sup> will be degraded by noise from this source in addition to environmental temperature fluctuations reflected into the critical current.

The dependence of both the voltage across the bridge and the

supercurrent through it upon the phase difference of the superconducting wave function across the device demands that fluctuations in the current or voltage cause fluctuations in the phase,  $\theta$ . Through the relation  $2eV = \hbar \frac{d\theta}{dt} = \hbar\omega$  a fluctuating voltage will directly result in a finite linewidth for the Josephson oscillation. Voltage or current fluctuations will be associated with a fluctuation in the phase of the wave function. The current-voltage characteristic will be strongly affected by such fluctuations around the critical current. As the binding energy,  $E = I_c \phi_0 \cos\theta$ , becomes comparable to  $kT$  for bias currents near the critical current. This changes the characteristics from the theoretical with infinite slope at  $I_c$  to one with slope changing smoothly from zero to a finite value.<sup>2</sup> A similar effect is observed near an rf induced constant voltage step in the characteristic; the step edges are rounded and for small steps the dynamic resistance is no longer zero at the step center.

Thus, integrated effects of the fluctuations serve to limit devices dependent upon the A-C Josephson effect; coherent radiation detectors, voltage standards, mixers and signal sources.

A study of the fluctuating electrical parameters in a bridge will help determine the limits of devices using the proximity effect bridges. Further, such a study through measurements of the total voltage fluctuations and the spectral density of these fluctuations will reflect understanding upon dissipative processes in the proximity effect bridges.

## 4.2 Background

In contrast to a regular, periodic signal, the future behavior of a randomly fluctuating quantity cannot be predicted from a knowledge of its past behavior.<sup>3,4</sup> This lack of predictive ability generally is the result of a lack of knowledge of the detailed motion of every quantity in a system. There is, however, a certain amount of information that is available about a fluctuating signal. In general, one can measure the average value of such a noise signal, and in physical systems it is generally assumed that this average value is independent of the time it is measured. Generally one can decompose such a signal into a constant equal to its average value and a fluctuating component  $\alpha(t)$  whose time average is zero.

$$\langle \alpha(t) \rangle = 0$$

where the brackets indicate an average over a large number of similarly prepared systems at a given time, which is equivalent to a time average. The average value of the square of the fluctuating component is, of course, not zero.  $\langle \alpha(t)\alpha(t) \rangle \neq 0$  If we take the product of the value of the fluctuating quantity at one time,  $t$ , and another time,  $t'$ , then for very long time differences this quantity is zero.  $\langle \alpha(t)\alpha(t') \rangle = 0$  but as  $t \rightarrow t'$  this quantity acquires a finite value as stated above. Therefore, there must be some characteristic time,  $T$ , over which the fluctuating quantity retains some memory of its previous values. Further, since we have assumed the averages independent of absolute time, the above expression may be replaced by

$\langle \alpha(t')\alpha(t'') \rangle = \langle \alpha(0)\alpha(t) \rangle = K(t)$ . This quantity is the correlation function of the fluctuating quantity  $\alpha(t)$  and only depends on the time interval  $t$ . The characteristic time  $T$  may be thought of as the approximate time between zero crossings of  $\alpha(t)$ . In addition to the total mean-square fluctuations one is often interested in the spectral decomposition of the fluctuating quantity. If we define

$$K(t) = \int_{-\infty}^{\infty} P'(\omega) e^{i\omega t} d\omega$$

then  $P'(\omega)$  is just the Fourier transform of  $K(t)$ . For  $K(t)$  to be real

$$P'(-\omega) = P'^*(\omega)$$

For the special case  $t = 0$

$$K(0) = \langle \alpha(0)\alpha(0) \rangle = \langle \alpha^2 \rangle = \int_0^{\infty} P(\omega) d\omega$$

where  $P(\omega) = 2\text{Re}P'(\omega)$ .  $P(\omega)$  is the spectral power density of  $\alpha(t)$ . This very important quantity indicates the contribution of each frequency interval to the total mean square fluctuations.

### 4.3 Previous Analysis

The resistance of a normal conductor gives rise to both the dissipation in the conductor and the noise currents generated by the conductor. For a system in thermal equilibrium the powerful fluctuation dissipation theorem<sup>5</sup> relates the fluctuation power density to the dissipative terms in the equation of motion of the body. If in the classical case where  $h\omega \ll kT$  one considers the current fluctuations in a conductor then

$$\langle i^2 \rangle = \int_0^{\infty} P_I(\omega) d\omega, \quad (4-1)$$

and

$$P(\omega) = \frac{2kT\sigma(\omega)}{\pi} \quad (4-2)$$

If  $\sigma$  is independent of frequency this is a white noise spectrum normalized by setting the magnetic energy of the noise currents equal to  $1/2 kT$ . The equal energy in each frequency interval implies that the correlation time  $\tau$  for the electron-phonon interaction is short compared to any time of interest in the problem. That is, for frequencies much less than  $\sim 1/\tau$  the current fluctuations are uncorrelated and independent of frequency. In the general case, the power spectrum of the current fluctuations is

$$P(\omega) = \frac{\hbar\omega\sigma(\omega)}{\pi} \coth\left(\frac{\beta\hbar\omega}{2}\right) \quad (4-3)$$

This expression agrees with Eq. (4-2) in the classical limit as it should. The requirement that the system is in equilibrium does not apply to our case as we are most often interested in the non-equilibrium situation where the bridge is driven in a steady state. In this case other noise sources may enter with appreciable magnitudes, but must be calculated for the particular physical processes involved.

In the case of a Josephson tunnel junction fluctuations in the current will be introduced by the tunneling process. The tunneling of the pairs involves the emission or absorption of a photon and the tunneling probability will be influenced by the number of such photons present. Fluctuations in the dissipation of these photons will result in fluctuations in the pair tunneling currents. Stephen<sup>6</sup> has calculated this effect and finds, for  $\omega < eV_0/\hbar$ ,

$$P_{I_p}(\omega) = \frac{2e}{\pi} I_p(V_0) \coth(e\beta V_0) \quad (4.4)$$

where  $V_0$  is the operating voltage.

Rogovin and Scalapino<sup>7</sup> have calculated the fluctuations in the quasiparticle tunneling currents and find

$$P_{I_{qp}}(\omega) = e/2\pi \left\{ I_{qp}(V_0 + \hbar\omega/e) \coth\left[\frac{\beta}{2}(eV_0 + \hbar\omega)\right] + I_{qp}(V_0 - \hbar\omega/e) \coth\left[\frac{\beta}{2}(eV_0 - \hbar\omega)\right] \right\} \quad (4.5)$$

This is the noise associated with the random passage of quasiparticles across a tunneling barrier.

Ambegoaker and Halprin<sup>2</sup> have investigated the effects upon a tunnel junction of a resistive shunt element with power spectrum given by Eq. (4-2). The current fluctuations in the resistor introduce fluctuations into the quantum phase difference across the device. They find the current-voltage characteristics most strongly affected in the area around the theoretical critical current where the energy in the fluctuations is comparable to the bridge energy of the two superconductors. This effect is strongest for small critical currents;  $I_c \phi_0 \approx kT$ . The noise fluctuations limit the maximum slope of the current voltage characteristics to finite values.

For a Josephson device of low heat capacity, thermodynamic temperature fluctuations

$$\langle \Delta T^2 \rangle = \frac{kT^2}{C_V} \quad (4-6)$$

where  $C_V$  is the heat capacity, will also introduce an additional noise source. These fluctuations will give rise to fluctuations in the critical current resulting in addition to fluctuations at all points on the I-V characteristics. Clarke<sup>8,9</sup> has analyzed such fluctuations phenomenologically and finds that a power spectrum proportional to  $1/f$  should appear.

#### 4.4 Previous Experiments:

There are two primary quantities of interest in the noise properties of a Josephson device. The total mean-square current or voltage fluctuations have been investigated primarily through their effect upon the linewidth of the Josephson oscillation<sup>10</sup> and upon the D-C current-voltage characteristics of the devices.<sup>11</sup> The power density spectrum of the fluctuations has not been as thoroughly investigated although some work has been done on a few types of devices.<sup>9,13</sup>

Kirschman<sup>12</sup> measured the radiation linewidth of a current biased proximity effect bridge and found the linewidth to be consistent with current fluctuations of the form

$$\langle i^2 \rangle \approx kT I_C / \phi_0$$

This expression incorporates Johnson noise in the bandwidth of the device, the normal resistance divided by the kinetic inductance.

Daym et al<sup>10</sup> have measured the linewidth of a Josephson tunnel junction. They found the linewidth to be consistent with the sum of the fluctuations in the quasiparticle current and those in the pair current as given by Eq. (4-4) and (4-5).

Kanter and Vernon<sup>13</sup> have directly investigated the power density of the fluctuations in a Nb-Nb point contact and conclude that the expressions for the fluctuations in the pair and quasiparticle currents Eq. (4-4) and (4-5) give an adequate fit to their data.

Parker and co-workers<sup>11</sup> have made careful measurements of the dc

current-voltage characteristics and the current-dynamic resistance characteristics and find generally good agreement with those predicted by the analysis of Ambegaokar and Halprin.<sup>2</sup> The agreement is particularly close in the case of a tunnel junction shunted by a resistor, for low critical currents.

Clarke and Hawkins<sup>9</sup> have investigated the voltage power density spectrum for very low frequencies. They find that for a shunted tunnel junction of very low heat capacity this spectrum has a strong  $1/f$  dependence for frequencies below 10 Hz. This dependence has been attributed to fluctuations in the critical current due to thermodynamic temperature fluctuations.

#### 4.5 Experimental Procedure

##### Effects of Noise in a Measurement System.

In performing a measurement upon any small signal it is vital for the experimenter to know how much noise his measurement system will add to the signal of interest.<sup>14</sup> Additional difficulties may arise from the presence of interfering signals. These considerations are particularly important in the case of noise measurements. For the moment let us concentrate upon the noise added by the measuring system and leave consideration of interfering signals until we discuss the particular experimental conditions encountered in this experiment. The noise added to an experimental signal is usually dominated by the first stage of the amplifier. Since different noise sources are generally regarded as random and uncorrelated, the individual noise powers add and the input noise at the first amplifier is most likely to have a power comparable to the signal power being processed.

The sum of the noise power from all the sources in an amplifier can be represented fairly accurately as the sum of an imaginary noise voltage source and an imaginary noise current source connected across the input of a noiseless infinite impedance amplifier of gain  $G$ . We denote these sources by  $i_n^2$  (amperes<sup>2</sup>/Hz) and  $e_n^2$  (Volts<sup>2</sup>/Hz). These sources may well be frequency dependent. For the moment, let us consider the source to have a resistance  $R_s$  at some temperature,  $T$ . This resistor produces Johnson noise  $\langle V^2 \rangle = 4kT \cdot R_s$ . The equivalent circuit is shown in Fig. 4.1. The noise current generator is considered to interact with the source impedance to produce a noise voltage  $i_n^2 R_s^2$ .

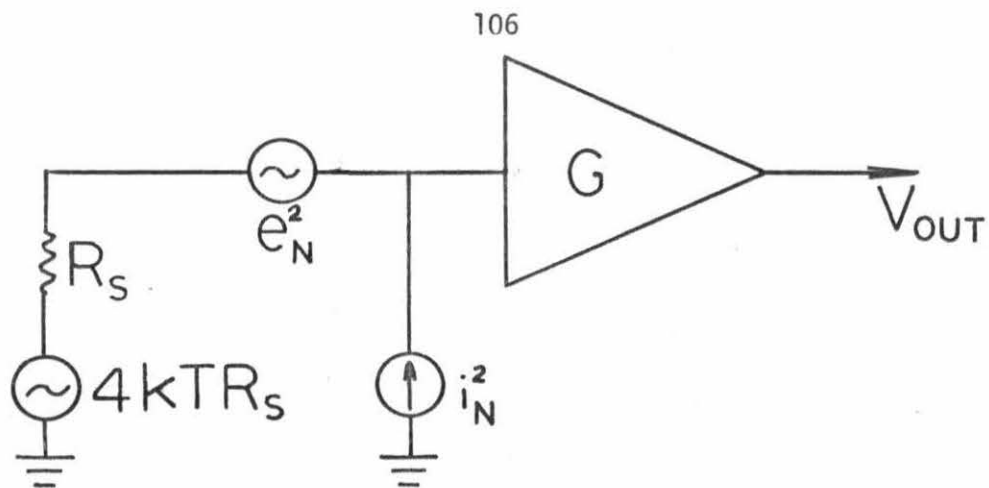


Fig. 4-1. Equivalent noise circuit of an amplifier. Noiseless amplifier of gain  $G$  is fed from a source impedance,  $R_s$ . Noise of amplifier is represented by noise current generator  $i_n^2$  and a noise voltage generator  $e_n^2$  connected across the input.

This gives a total noise voltage, referred to the input of the amplifier, given by

$$E_i^2 = 4kTR_s + i_n^2 R_s^2 + e_n^2 \quad (4-7)$$

The most commonly given specification for the noise characteristics of an amplifier is the noise figure. The noise figure is ten times the log of the ratio of the total noise power at the input to that of the thermal noise from the source.

$$N_F = 10 \log_{10} \left[ \frac{4kTR_s + i_n^2 R_s^2 + e_n^2}{4kTR_s} \right] \quad (4-8)$$

The noise figure is a function of temperature, frequency, and source resistance. The temperature of the source resistance is commonly taken to be room temperature, 290°K. For the preamplifier used in this experiment (PAR 185) the minimum noise figure is 0.01 dB for  $R_s \sim 5 \times 10^5 \Omega$ . It is instructive to calculate the noise power at the input due to the presence of the amplifier.

$$N_F = 10 \log_{10} \left[ 1 + \frac{e_n^2 + (i_n R_s)^2}{4kTR_s} \right] \quad (4-9)$$

$$E_A^2 = \left( 10 \text{ NF} / 10^{-1} \right) 4kTR_s = 2 \times 10^{-3} 4kTR_s$$

for a noise figure of 0.01 dB. This is insignificant compared to the thermal noise from the source resistance at room temperature. If the source resistance is not at room temperature, but is part of a cryogenic experiment, the thermal noise from the source impedance will be reduced

while the amplifier noise stays constant, becoming a larger fraction of the source noise. Therefore, the noise figures are no longer directly useful to calculate the noise added by the amplifier in this situation.

We can eliminate this difficulty by making use of the concept of equivalent noise temperature. The total noise power referred to the input then becomes

$$E_i^2 = 4kT_s R_s + 4kT_e R_s \quad , \quad (4-10)$$

$$4kT_e R_s = E_A^2 = i_n^2 R_s^2 + e_n^2 \quad . \quad (4-11)$$

where  $T_e$  is the equivalent noise temperature. The noise temperature is independent of source temperature as desired. We can relate this quantity to the noise figure by

$$T_e = 290 (10 \text{ NF}/10 - 1) \quad , \quad (4-12)$$

where 290 is the temperature (room temperature) used to calculate noise figure. A small change in noise figure will imply a large change in noise temperature. The noise temperature will depend upon source resistance in the same way that the noise figure does, except that the degradation as we stray from the minimum noise figure (optimum source impedance) is explicitly illustrated.

The optimum source impedance may be calculated from the noise figure.

$$\frac{dN_F}{dR_s} = 0$$

yielding

$$4kTR_s \left[ 2i_n^2 R_s \right] - 4kT i_n^2 + i_m^3 R_s^2 = 0 \quad (4-13)$$

$$R_s^2 = e_n^2 / i_n^2$$

This value of  $R_s$  yields the minimum noise figure and temperature.

In measurements of proximity effect bridges in these experiments the source impedance was much lower than optimum. One may use a transformer to match the low source impedance to the optimum by selecting the turns ratio  $A$  such that  $A^2 R_s = R_{opt}$ . In general a real (as opposed to perfect) transformer will add some noise to the source noise but generally the overall signal to noise ratio is improved. This noise is primarily due to the dc resistance of the windings.<sup>14</sup>

#### Noise Measurement System.

To measure the voltage noise density spectrum for the proximity effect bridges requires a system capable of measuring voltage on the order of the Johnson noise in the impedance characteristic of the devices, at liquid helium temperature;

$$V/\sqrt{Hz} = (RkT)^{1/2} \sim 5 \times 10^{-12}$$

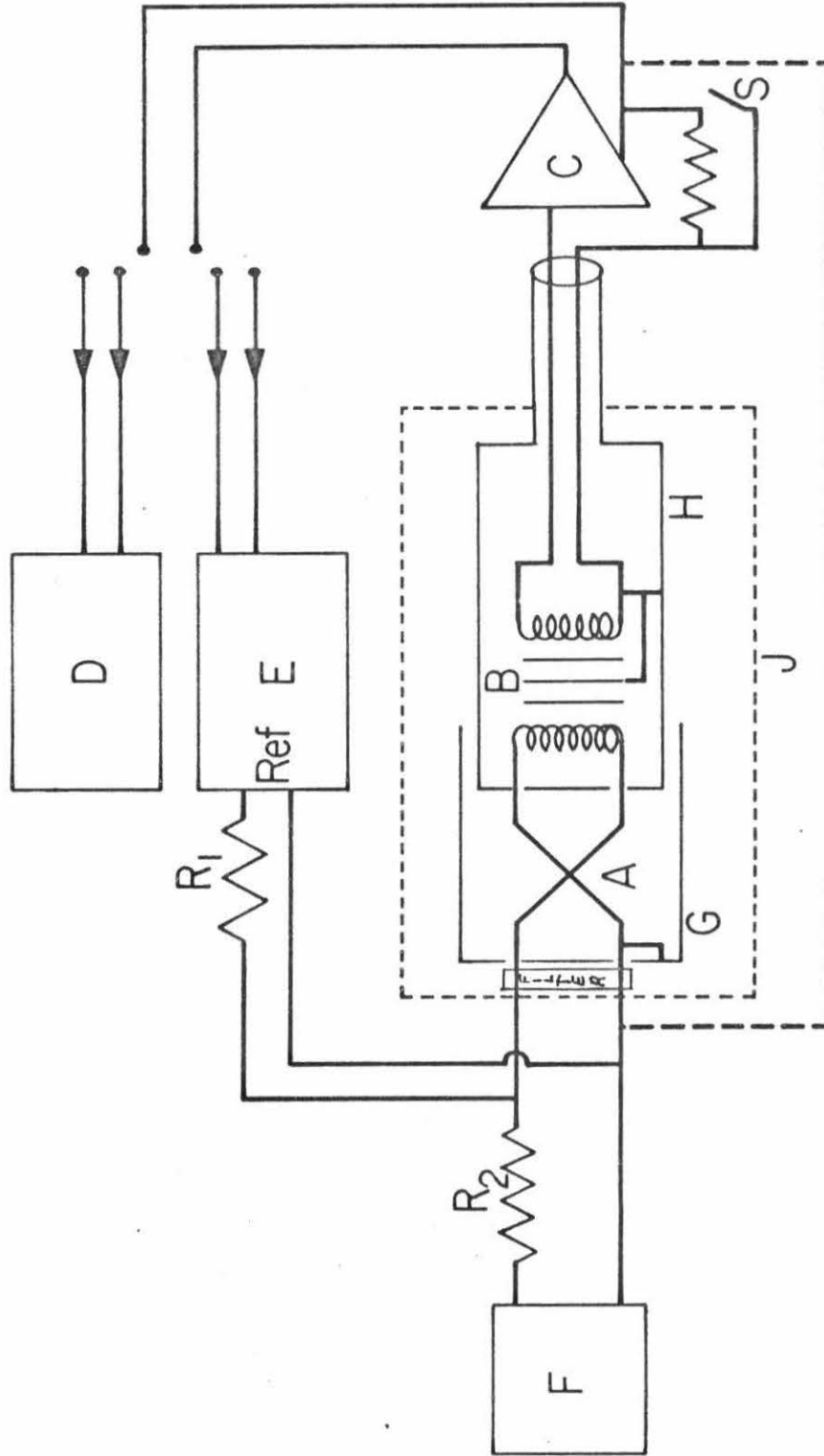
The measurements of the noise density in these bridges were carried out using a cooled transformer<sup>15</sup> and a room temperature low noise preamplifier. The preamplifier has its optimum noise performance for

source impedances far above the typical impedances of these junctions. The transformer is used to match the impedance of the source to the optimum source impedance of the amplifier. If the transformer is cooled to liquid helium temperatures, it will add almost no noise to that of the amplifier as the flux noise in the core and the resistive noise in the windings are reduced at low temperatures. The experimental configuration is detailed in Fig. 4.2. The bridge under test is mounted directly upon the input of a Triad G-4 Transformer, modified for use at helium temperatures. This transformer has a nominal gain at 4.2°K of 380 with a bandpass of 10-4000 Hz. The bridge is shielded from the transformer by copper,  $\mu$  metal, and superconducting lead shields. This shielding also reduces extraneous signals induced into the transformer. The signal from the transformer is carried to the preamplifier on shielded leads. The entire dewar assembly is housed in a  $\mu$  metal cylinder for magnetic shielding and an experiment is carried out in a shielded room capable of 80 dB rf shielding.

The preamplifier is a PAR 185, which, for a source impedance between  $3 \times 10^5$  and  $2 \times 10^6$  ohms and a frequency of  $10^3$  Hz, has a mean noise voltage of  $3\text{nv}/\sqrt{\text{HZ}}$ . The use of the transformer gives an optimum source impedance of  $\sim 5$  ohms for the combination. The preamplifier is housed in a PAR 114 amplifier which provides additional gain and signal conditioning. The output of the amplifier is fed into either an IRI Tunable Microvoltmeter or into a Hewlett-Packard 3590A Wave Analyzer for detection. If dynamic resistance rather than noise voltage is the quantity under measurement, then the output of the amplifier

Fig. 4-2. Schematic of Noise Measurement System. The proximity effect bridge, A, is mounted directly upon the input of a cooled transformer, B. The signal from the transformer is carried on shielded leads to the room temperature preamplifier, C. The signal is then fed into either a IRI tunable voltmeter, D, or a phase sensitive detector, E. Bias current is provided from a digital ramp generator, F. G and H indicate superconducting shields used to isolate the bridge and the transformer from external influences. Low pass filters are in the current leads. The dashed line indicates a grounding strap used to insure that the chassis grounds the various instruments are at the same potential. J indicates the limits of the cryogenic environment.

## NOISE MEASUREMENT SYSTEM



is fed into a PAR HR-8 phase sensitive detector which detects the alternating signal provided in its reference channel. This reference signal is, of course, not supplied during noise measurements.

Provision is made for bias current to be fed to the bridge from an external current source. This bias current passes through a low temperature, low pass filter which is mounted just external to an additional superconducting lead shield surrounding the bridge under test. Magnetic field is provided by a coil inside the lead shield surrounding the bridge.

#### 4.6 Noise Performance

The noise temperature performance of the system yields a measure of the efficiency of the shielding of the apparatus as described above.

The noise temperature consists of two parts

$$T_e = e_n^2 / 4kR_s + \frac{i_n^2 R_s^2}{4kR_s}$$

a measurement of the noise temperature for low values of  $R_s$  yields  $e_n^2$  directly. For this system  $e_n^2 = 1.20 \times 10^{-22} \text{ V}^2/\text{Hz}$ . Measuring the noise temperature at higher values of  $R_s$  and using  $e_n^2$  yields  $e_n^2 = 4.93 \times 10^{-23} \text{ A}^2/\text{Hz}$ . Using these values one can construct a noise temperature diagram for a center frequency of 1000 Hz. This is plotted in Fig. 4-3. The noise temperature is seen to have a minimum value of 2.8°K at  $R_s = 1.56\Omega$ . Also plotted in Fig. 4-3 is the noise temperature diagram for the PAR 185 preamplifier using the manufacturer's noise specifications and assuming an ideal transformer. The difference in the two curves is consistent with the noise power generated by the resistivity of the transformer windings at the bath temperature (2.5°K for the curve shown.) Further, the difference in the noise temperature characteristics increases linearly with bath temperature as expected for noise from this source. This indicates that all components of noise generated by the measuring system have been properly taken into account. The system may now be used to reliably measure the noise generated in the device under test.

When used with the lock-in amplifier to detect coherent signals, the system can easily detect a signal of  $10^{-11}$  volts across a one ohm

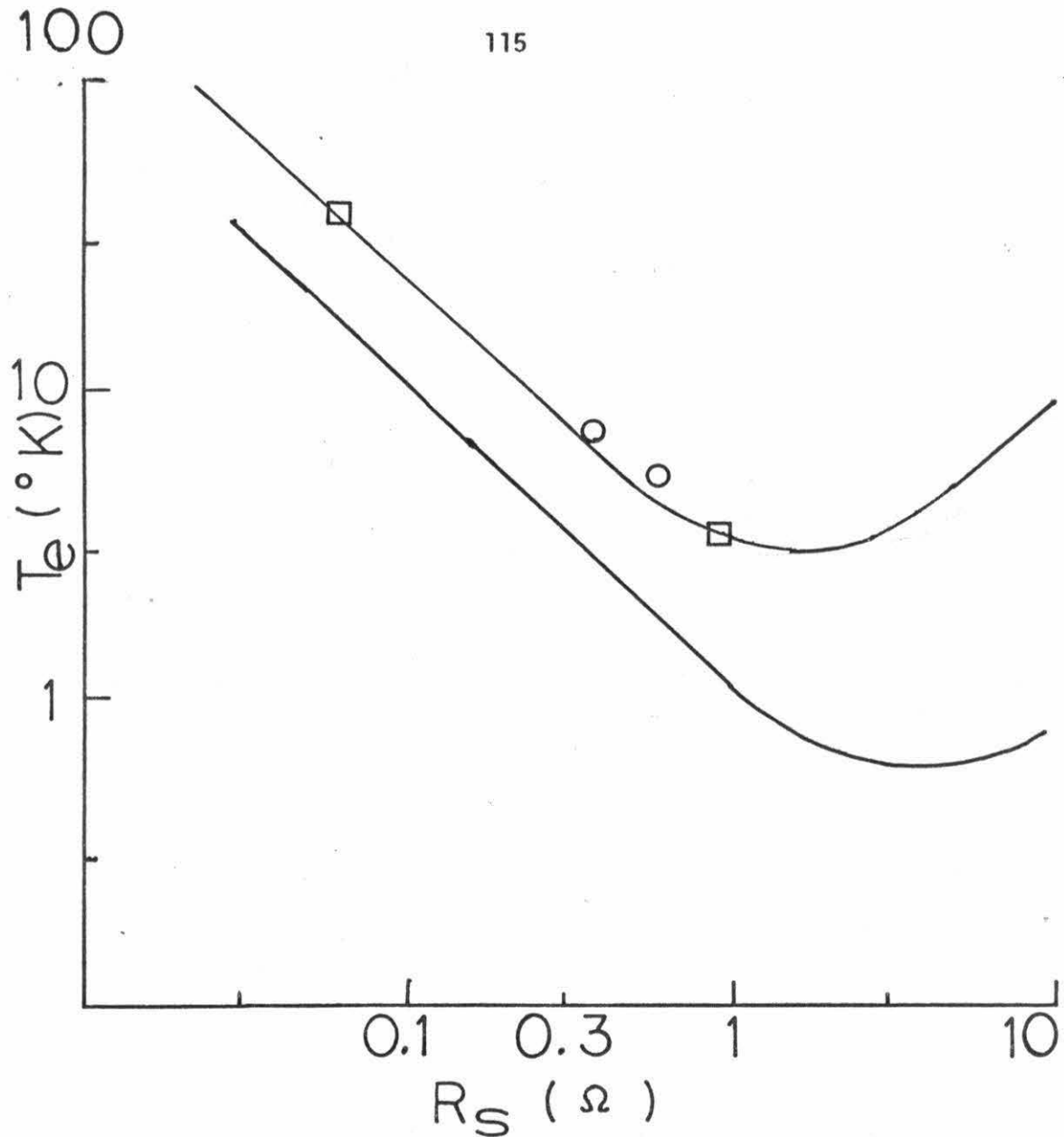


Fig. 4-3. Observed noise temperature characteristics of the measurement system at 1000 Hz and 2.44°K, upper trace. Calculated noise temperature assuming an ideal transformer, lower trace. The difference in characteristics is due to the resistivity of windings at the bath temperature. Squares denote noise temperature with a calibrated wire resistor as source. Circles denote noise temperature with a thin film source.

source resistor at 4.2°K using a time constant of one second. This is consistent with the above noise temperatures.

#### 4.7 External Noise and Interference

Modern civilization produces a host of electrical signals at a variety of frequencies which have the unfortunate property of interfering with a measurement of this sort. The ac power lines, local television and radio, microwave ovens, and many items of laboratory equipment all produce interfering signals of much greater magnitude than the signal of interest. Such external signals must be screened from the proximity effect bridge under test. In addition to signals directly interfering at the measurement frequencies, signals at other frequencies, television for example, will influence the quantum phase of the bridge thus influencing the low frequency operation of the device.

An important consideration is the magnitude and effect of the noise power produced in room temperature resistors and then introduced into the bridge via the measurement lead wires. As an approximation of these effects at low frequency, we imagine external noise as generated in a room temperature  $T_r$ , resistor  $R$ , connected in series with the bridge. Then the noise voltage density appearing across the bridge from external sources is,

$$S_{\text{ex}}^2 = \left(\frac{R_d}{R}\right)^2 4kT_r$$

if  $R$  is much larger than the dynamic resistance of the bridge,  $R_d$ . Similarly, the noise voltage density from the bridge resistance is  $S_j^2 = 4kT_b R_d$ . Thus, as long as  $R_d T_r \ll R T_b$ , external noise effects will be small relative to those originating within the bridge itself,

the bridge noise will dominate; this criterion was followed in the design of these measurements.

Another measure of the interfering signals produced in the bridges through external influences can be inferred from the temperature dependence of the dynamic resistance of the bridge. The energy of a noise signal, or interfering signal, will be most likely to disrupt the quantum phase coherence of the system when the binding energy of the two superconductors is equal to or less than the energy introduced by the interfering signal. This will be true for small zero voltage currents and within the normal to superconducting transition of the bridge. The calculation of Ambegaokar and Halprin<sup>2</sup> (see Sec. 4.2) for a resistively shunted tunnel junction indicates that the dynamic resistance at zero bias current is very sensitive to the noise energy present in the bridge. This has been confirmed experimentally by Parker.

Using measured values of the dynamic resistance as a function of bias current with bath temperature as a parameter one may extract an effective temperature for the bridge from published curves<sup>11</sup> predicting the behavior of the dynamic resistance calculated from the model discussed above. In all cases this effective temperature is within about 20% of the bath temperature. This measurement, although indirect, gives an excellent estimate of the integrated energy of the interfering signals compared to the energy of the fluctuations generated by the device under test.

Using published curves for the model of Ambegaokar and Halprin (see Sec. 4.2), the minimum zero resistance current<sup>5</sup> is approximately  $I_m \approx 0.1 I_c$  when  $\gamma = \frac{hI_c}{ekT} = 5$ , and where  $I_c$  is their fitting parameter, the "critical current." Using  $T = 4K$ , we calculate a value for  $I_{min} \sim 5 \times 10^{-8}A$  which is in very good agreement with the minimum zero resistance current we observe ( $4.5 \times 10^{-8}A$ ). If we remove the shielding precautions, this value increases to  $\sim 1.5 \times 10^{-6}A$  and does not occur until a much lower temperature. Thus, at least in I-V characteristics, this system performance is consistent with that expected from a simplified model of a resistively shorted junction at the bath temperature.

The above considerations give an indication of the levels of the total external interfering signals. The primary interfering signals in our frequency range are, of course, the multiples of the power line frequency. The amplitude of the 60 Hz signal is  $\sim 3 \times 10^{-10} V$ , after careful shielding.

#### Experimental Sample Configurations.

The noise density spectrum was measured on proximity effect bridges constructed upon three film-substrate combinations; niobium on tantalum on sapphire, tantalum on titanium on sapphire, and tantalum on titanium on glass. All bridges were constructed by techniques described in Chapter 2. All bridges had lengths  $< 1\mu$ .

Six bridges were constructed from the Nb/Ta/sapphire parent material. The transition temperature of all bridges was  $\pm 4.0^\circ K$ . Resistance of the bridges ranged from  $0.08\Omega$  to  $0.25\Omega$ .

Three bridges were constructed from the Ta/Ti/sapphire parent material. The transition temperature of these bridges ranged from 2.0°K to 2.5°K. The resistances of these bridges were 0.17 $\Omega$  , 0.33 $\Omega$  , and 0.42 $\Omega$ .

Two bridges were constructed on Ta/Ti/glass parent material. The transition temperatures were 2.17°K and 2.405°K. The resistance of these junctions were 0.8 $\Omega$  and 0.35 $\Omega$ .

#### 4.8 Measurements of Noise Density Spectrum.

With the system described earlier, the voltage fluctuations in a proximity effect bridge could be measured directly as a function of bias current. These measurements are possible with temperature, critical current, magnetic field, and radio frequency radiation as parameters. Measurements were possible in a range of frequencies greater than two decades, 20 Hz to 4000 Hz.

Several features were common to all the samples, except the bridges made from Ta/Ti/glass parent material. The distinctive features of these bridges will be discussed separately. At temperatures far above the transition temperatures of the bridge the device behaves as a resistor of value  $R_n$ . Above the bridge transition temperature the noise density scales with  $R$  and  $T$  as expected for Johnson noise. The noise density is independent of frequency in the range available for measurement and is independent of bias current for  $I_0 < 100 \mu\text{A}$ .

As the temperature is lowered through the transition region, the dynamic resistance slowly drops until a zero voltage current appears.<sup>2,11,16</sup> For these bridges, this temperature interval between resistance  $R_n$  and zero (for "zero" current) can be as large as  $1/2^\circ\text{K}$ . However, as soon as the dynamic resistance  $R_d$  at zero current falls below  $R_n$ , the device begins to show quantum interference effects, both the ac and dc Josephson phenomena, even though there may be no zero-voltage current. In this temperature region, the dynamic resistance also becomes a function of current  $R_d(I)$ . To within experimental accuracy, in this temperature regime the noise voltage at zero current remains Johnson

and scales with  $R_d(0)$ .

In Fig. 4-4, we see a typical trace of the output noise below the transition as a function of bias current at a temperature below the transition region. This voltage is proportional to the square root of the voltage output power density,  $E \propto [\langle V(f)^2 \rangle + E_A^2]^{1/2}$ . The lower trace is the dynamic resistance of the bridge for purposes of comparison. This figure illustrates several features common to all the data. In the limit of high currents (relative to the critical current), the voltage noise density approaches a constant value equal to that for the bridge in normal state above the transition.

Another feature common to all the data is that in the vicinity of the critical current the noise density  $\langle V^2(f) \rangle$  is much higher than at higher currents. In Fig. 4-4 the maximum is:

$$\langle V^2(f) \rangle = 4.9 \times 10^{-22} \text{ V}^2/\text{Hz}$$

This maximum in the noise density does not appear at the same bias current as the maximum in the dynamic resistance but always occurs at a slightly lower current. The noise voltage appears to initiate slightly below those bias currents at which the device becomes resistive.

Such a large maximum in the noise density near the critical current is, of course, very important to the understanding of the operation of the bridge. In Fig. 4-5 the effect of changes in the critical current and magnetic field is summarized. Again the output noise voltage is plotted against bias current. In the upper traces temperature is the parameter between curves; in the lower, magnetic field is the parameter.

Fig. 4-4. Upper trace is a plot of output noise voltage as a function of bias current. Noise voltage at the higher currents approaches the value observed in the normal state. Lower trace is  $dV/dI$  as a function of bias current for purposes of comparison. The asymptotic value approached by the noise voltage corresponds to a spectral power density of  $6.7 \times 10^{-23} \text{ V}^2/\text{Hz}$ .

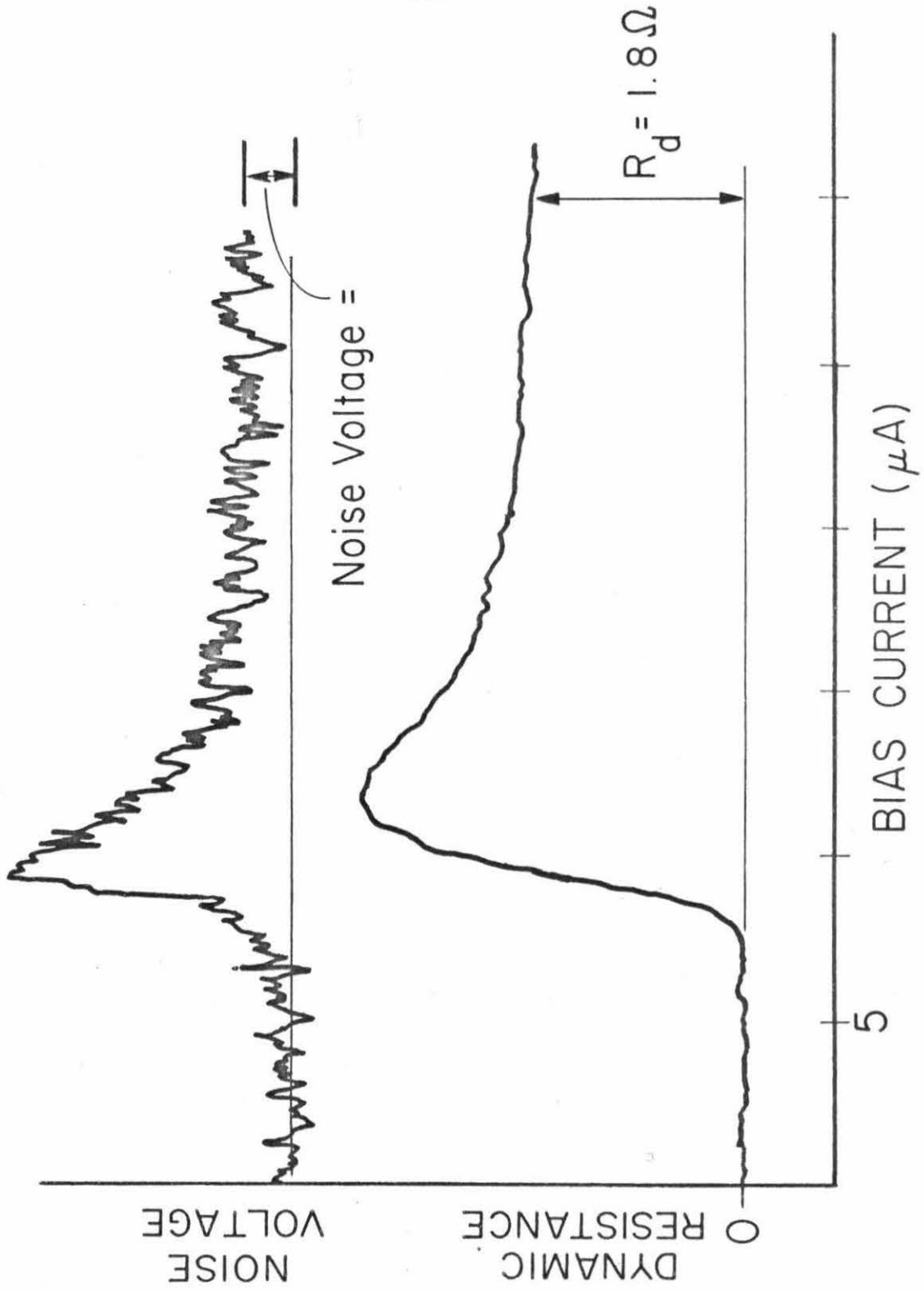
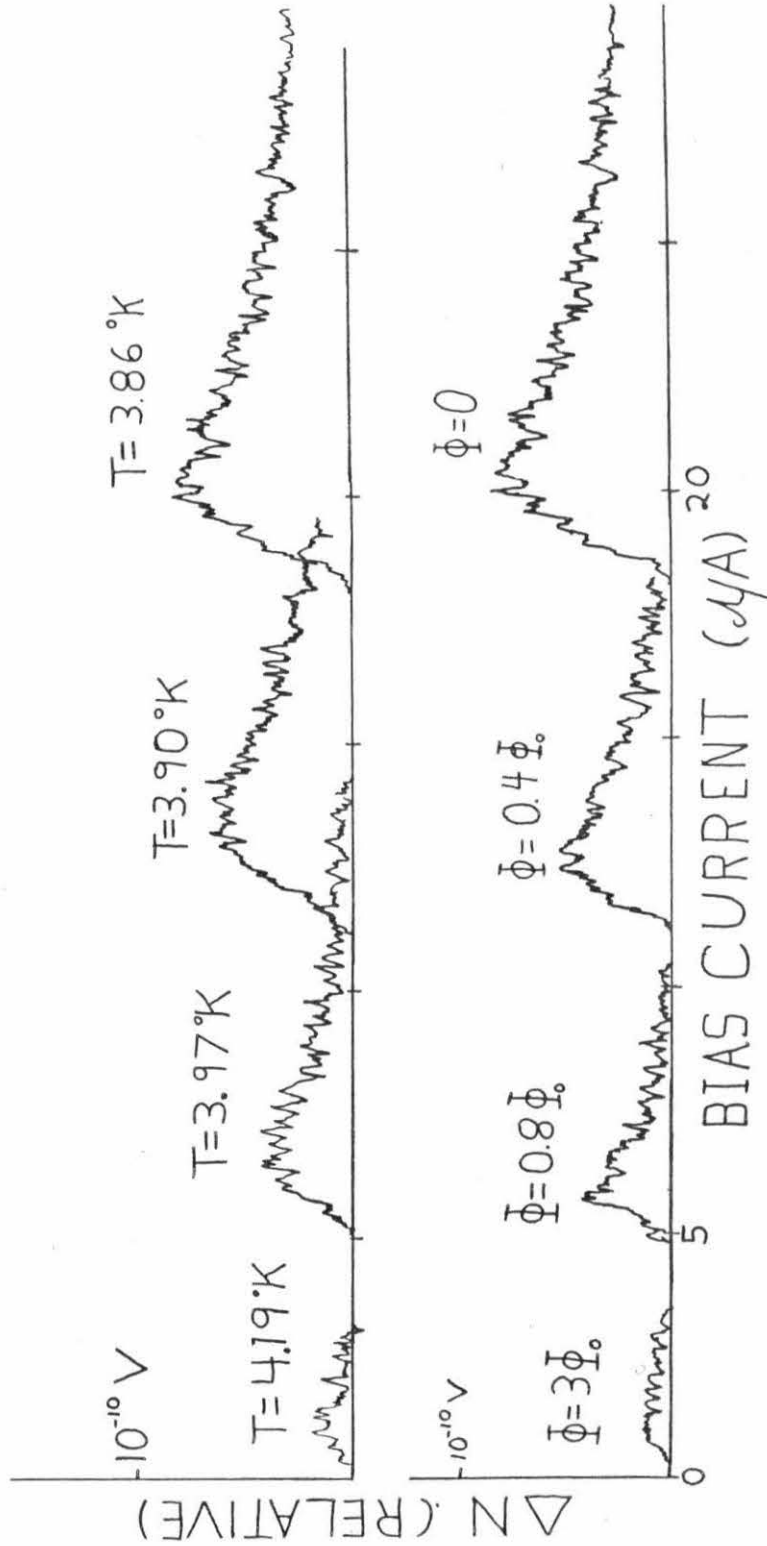


Fig. 4-5. Effect of temperature and magnetic field upon the noise voltage observed around the critical current. Noise voltage is plotted as a function of bias current for several critical currents. The baseline represents the noise voltage level corresponding to the amplifier noise plus that due to Johnson noise in the device.

The upper series of traces was taken at zero magnetic field temperature changes between curves.

In the lower series of traces the temperature is held at 3.86°K and the magnetic field upon the bridge is changed.

As plotted, these data are not intended for quantitative comparisons but rather to facilitate relative examinations. The data of the top traces will be presented in a quantitative way in Fig. 4-8.



As the critical current decreases due either to changes in temperature or magnetic field, the magnitude of the noise voltage near the critical current also decreases, indicating the noise voltage maxima scale as the critical current rather than B or T directly. Although the fluctuations predominately depend upon the critical current second order effects due to the difference between temperature suppression and magnetic field suppression of the critical current are observed. This indicates a possible dependence upon the detailed shape of the I-V characteristic as another parameter in addition to the critical current.

These measurements, carried out at 1000 Hz center frequency, have been repeated at 500 Hz, 285 Hz, 100 Hz with no change in magnitude or current dependence of the noise. By fixing the bias current at, for example, the noise maximum at one frequency, swept frequency measurements may be performed with the wave analyzer. These measurements yield a white power density spectrum down to 20 Hz as shown in Fig. 4-6.

In Fig. 4-7 is shown the effect of RF radiation upon the bridge noise. Again the dynamic resistance is plotted for comparison. The noise at the critical current is largely unchanged by radiation except to the extent that  $I_c$  is decreased, and again the noise decreases for the higher currents. However, there is excess noise also around the induced current "step" which is of comparable magnitude to that at the critical current. This noise again does not appear at the maxima of the dynamic resistance, but is offset on both sides towards the center of the step. The noise on the high current side of the step has a higher magnitude than the low current side. At the center of

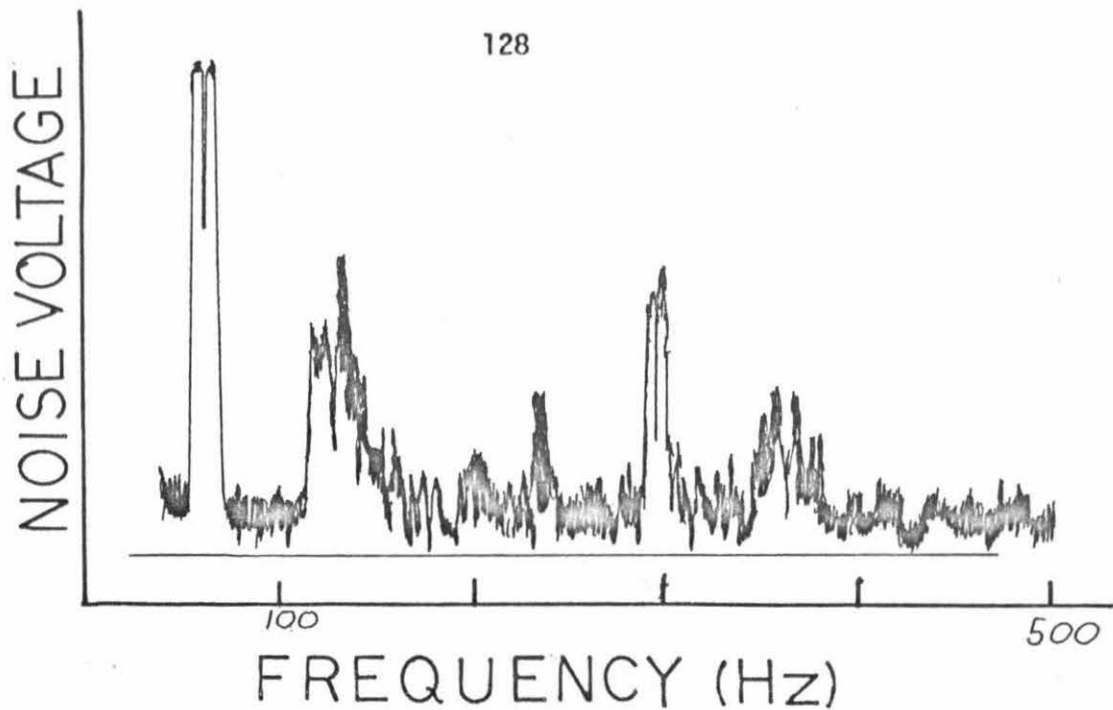
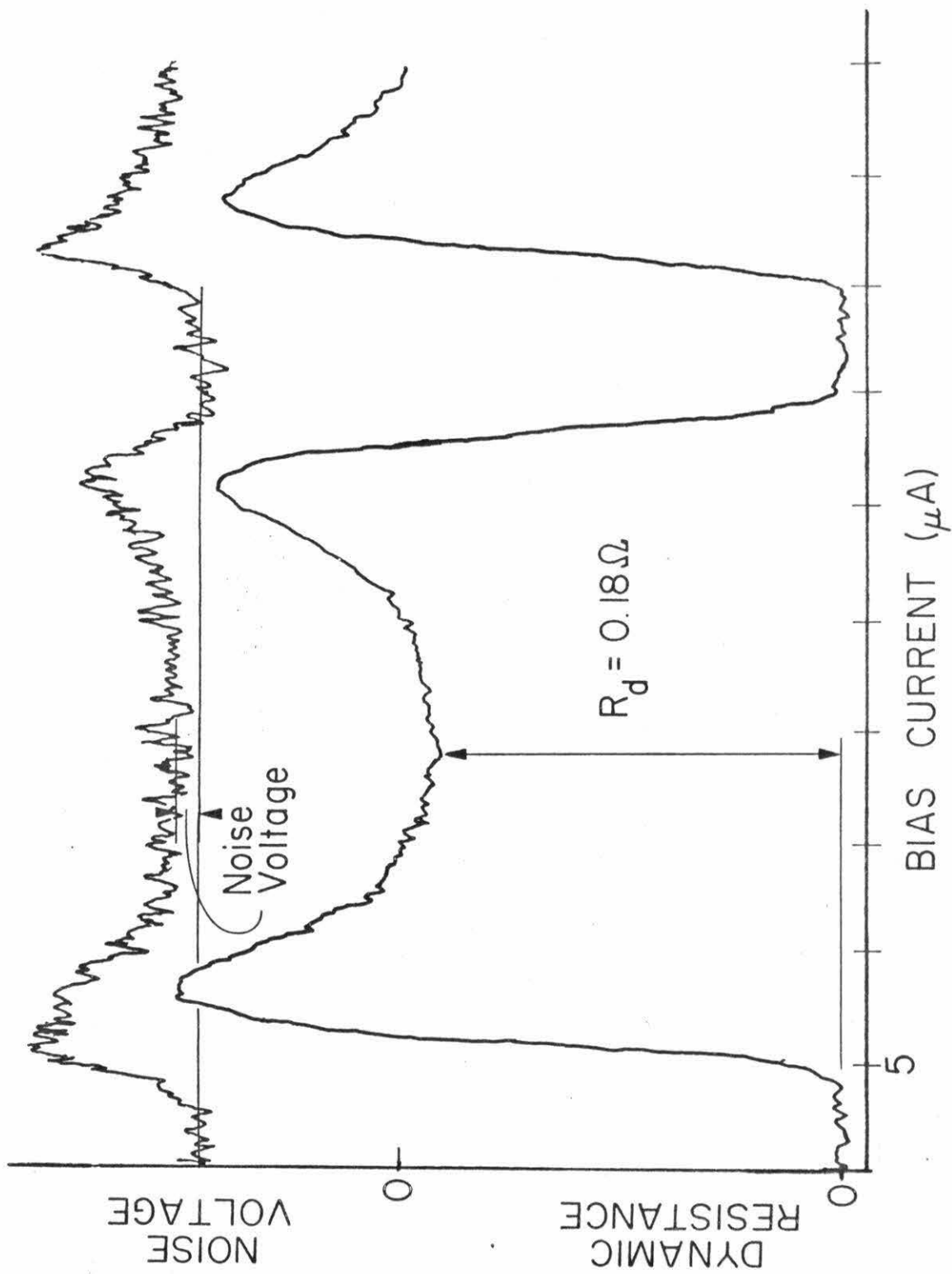


Fig. 4-6. Output noise voltage as a function of frequency for a Nb/Ta proximity effect bridge on sapphire. Bridge is biased to maximum in noise voltage and frequency is swept. Spectrum is seen to be flat except for peaks at harmonics of the line frequency. Flat spectrum extends to at least 2000 Hz. Horizontal line indicates the contribution of the amplifier to the observed noise. Vertical side is linear in observed noise voltage. Contribution from the bridge corresponds to a spectral density of  $\sim 6.7 \times 10^{-23} \text{ V}^2/\text{Hz}$

Fig. 4-7. Upper trace is output noise voltage as a function of bias current. Lower trace is the dynamic resistance for comparison. Electromagnetic radiation at 2 GHz is applied to the junction. Excess noise is seen above and below the step as well as near the critical current. Noise voltage at the indicated point corresponds to a spectral density of  $\sim 6.7 \times 10^{-23} \text{ V}^2/\text{Hz}$ .



the step the noise drops to a level characteristic of the measuring system noise, which is our zero level, implying that the noise voltage is zero, even at finite voltage, when the dynamic resistance, is zero.

#### 4.9 Discussion

The results presented in the previous section, and illustrated in Figs. 4-4, 4-5, 4-6, and 4-7, are typical of all measurements upon Nb/Ta/sapphire and Ta/Ti/sapphire bridges and may be put into perspective qualitatively and quantitatively with reference to the two fluid models presented in the first chapter. In this model the current through the bridge is presumed composed of a normal current and a superfluid current. If the fluctuations in each component of the flow are assumed to be uncorrelated, then the power densities of the voltage fluctuations produced by each will add to give the total power density of the fluctuations across the device. In what follows, the voltage fluctuations,  $S_n(f)$ , due to the normal current fluctuations will be seen to depend upon the transfer impedance representing the supercurrent fluid. The normal current fluctuations are still given by the Nyquist expression, Eq. 4.2. The voltage fluctuations due to the supercurrent flow,  $S_s(f)$ , will be seen to result from the passage of pairs across the bridge. The total expression for the voltage fluctuations across the device will then be found to be in excellent quantitative agreement with the observed fluctuations.

##### Effect of Transfer Impedance

The proximity effect bridge has been shown experimentally to behave as a normal resistance shunted by a non-linear, oscillatory, superconducting element. This element can be characterized by the expression for the supercurrent passing through it as developed in the first chapter:

$$I_s(t) = I_C/2 [1 + \cos \theta] \quad , \quad (4.13)$$

with

$$\dot{\theta} = 2eV(t)/\hbar \quad . \quad (4.14)$$

Interaction of the normal fluid with the lattice produces fluctuations in the normal current flow whose power spectrum is assumed to be given by the usual expression for Nyquist noise:

$$P_{I_N}(f) = 4kT/R \quad . \quad (4.15)$$

In the absence of the shunt element, this would give rise to a spectral density for the voltage fluctuations given by:

$$S_v(f) = \frac{4kTR_d^2}{R} \quad . \quad (4.16)$$

Where  $R_d$  is the dynamic resistance, the small signal response for the system. However, for these proximity effect bridges, this voltage fluctuation density will be modified by the presence of the non-linear shunt element representing the supercurrent flow. In the voltage sustaining state this element can be described as an oscillator whose frequency and impedance depend upon the voltage appearing across it. This combination of a resistively shorted non-linear oscillator will then function as a mixer with the superconducting oscillator acting as a local oscillator at frequency  $\omega = (2e/\hbar)\bar{V}$ . Energy from current fluctuations around the local oscillator frequency can thus appear as voltage fluctuations at other frequencies due to this mixing action.

Those fluctuations which appear near zero frequency are of most importance to this work. As demonstrated in the first chapter the oscillation in the bridge becomes particularly anharmonic for bias currents near the critical current. This implies that for bias currents slightly higher than the critical current, current fluctuations at several frequencies will be mixed down to the low frequency voltage fluctuations that we observe and thus we can expect the most pronounced low frequency noise effects to occur for current near critical.

Likharev and Semenov<sup>17</sup> have performed a calculation of this effect for a pure Josephson element. In their case the shunt element is characterized by

$$I_s(t) = I_c \sin \theta \quad , \quad (4.17)$$

and

$$\dot{\theta} = 2eV/\hbar \quad .$$

They obtain the voltage spectrum due to Nyquist fluctuations in the resistor R,

$$S_N(f) = \frac{4kTR_d^2}{R} \left[ 1 + \frac{1}{2} \frac{I_c^2}{I^2} \right] \quad . \quad (4.18)$$

We have performed (Appendix A) a similar calculation for the shunt element assumed for our junctions. The resulting voltage spectral density is given by

$$S_N(f) = \frac{4kTR_d^2}{R} \left[ 1 + \frac{1}{2} \frac{I_c^2}{(2I - I_c)^2} \right] \quad . \quad (4.19)$$

The voltage spectrum is composed of two terms; the first of which is produced by the fluctuations in the normal current (that expected from Nyquist noise) plus a second contribution from current fluctuations at frequencies near that of the oscillation in the proximity effect bridge. As anticipated from the physical arguments, the second term decreases as the bias current is increased above the critical current, reflecting the more nearly harmonic form of the oscillation in the proximity effect bridge at higher currents.

This expression for  $S_n(f)$ , is plotted in Fig. 4-8, and is compared with the observed noise density from the upper traces in Fig. 4-5. As indicated by the poor fit, this expression is not adequate to account for all of the observed fluctuations. The predicted values are too small by a factor of 3-5 near the critical current. More importantly the maxima values of this expression fall very near the maxima of the dynamic resistance rather than the maxima of the observed noise values, indicating that this analytic result is incorrect in both magnitude and functional form. See page 149 for Fig. 4-8.

#### Supercurrent Fluctuations.

Another possible source of noise in the proximity effect bridges arises from the transition of the superconducting pairs across the potential drop produced by the bridge. The pairs and electrons in a superconductor are normally in thermodynamic and chemical equilibrium. However, the phase slip process in the proximity effect bridge,<sup>18</sup> during which the amplitude of wave function collapses to zero and the phase slips by  $2\pi$  at the Josephson frequency, is an intrinsically time

dependent, irreversible, and non-equilibrium situation, which will be seen to give rise to a contribution to the voltage fluctuations across the bridge.

The following model has been developed as an analytic approximation to this effect and has some success in describing other properties of these conducting junctions. In what follows the model is applied to an analysis of pair noise.

For simplicity, consider the situation at a current carrying super-normal (s/n) boundary. The superconducting wave function must go to zero near the boundary and the supercurrent must be converted to a normal current. A detailed calculation<sup>19</sup> indicates that this complex process can be approximated by considering that the pairs and electrons are not in thermodynamic equilibrium with one another and that the electrons and pairs are each characterized by separate electro-chemical potentials,  $\mu_e$  and  $\mu_p$ . In an equilibrium situation the two potentials are equal. However, in a non-equilibrium situation characterized by a divergence of the supercurrent, the potentials are unequal and the difference in potentials is found to be proportional to the divergence of the supercurrent. Near a current carrying boundary between a superconductor and a normal metal the supercurrent must decay to give rise to the normal current. This causes a large divergence in the supercurrent and thus produces a difference in the chemical potentials of the pairs and the electrons. The pair potential is found to remain constant while that of the electrons must change to produce the gradient in the electron potential, or electric field, which gives rise to a normal current

flow.

$$j_n = -\sigma/e(\nabla\mu_e) \quad (4.20)$$

These results are illustrated in Fig. 4-9, which shows the calculated variations in  $\mu_e$ ,  $\mu_p$ ,  $j_n$ ,  $j_s$  and  $\psi$  near a (s/n) boundary. Notice in particular that  $\psi$  is seen to extend a relatively large distance into the normal material. The scale of variation in the horizontal direction is taken to be the coherence length -- typically a hundred angstroms in these films.

Yu<sup>20,21</sup> has confirmed these predictions experimentally. He was able to measure the difference between the pair potential,  $\mu_p$ , and the electron potential,  $\mu_e$ , on both sides of a superconducting-normal interface. He found excellent agreement with the theory but found the characteristic length to be longer than the expected coherence length in these films indicating that the two potential concept is correct but that the decay length is probably determined by a quasi-particle relaxation time.

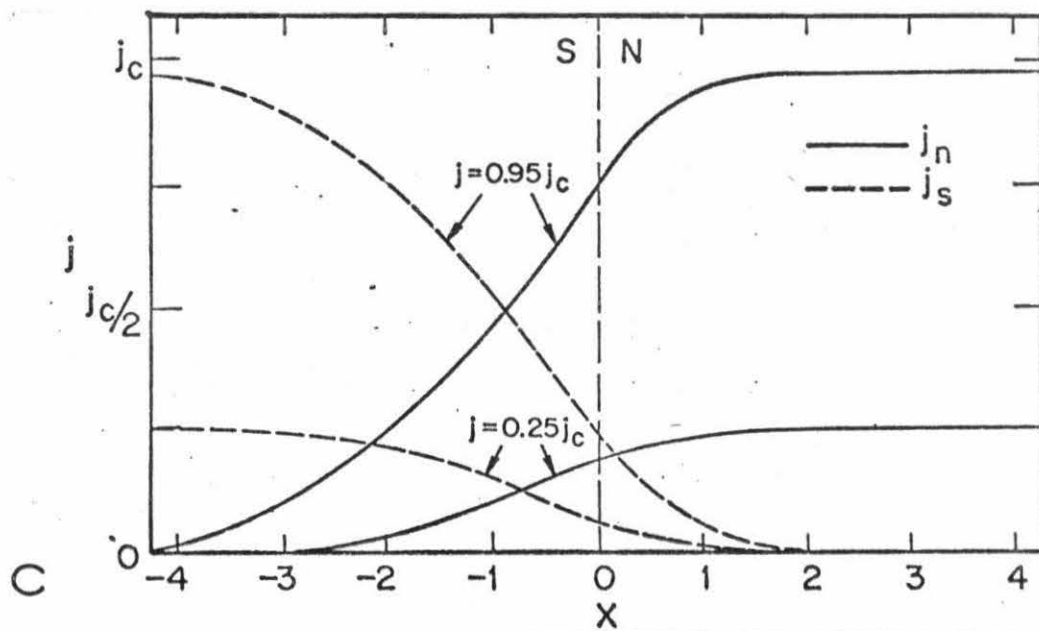
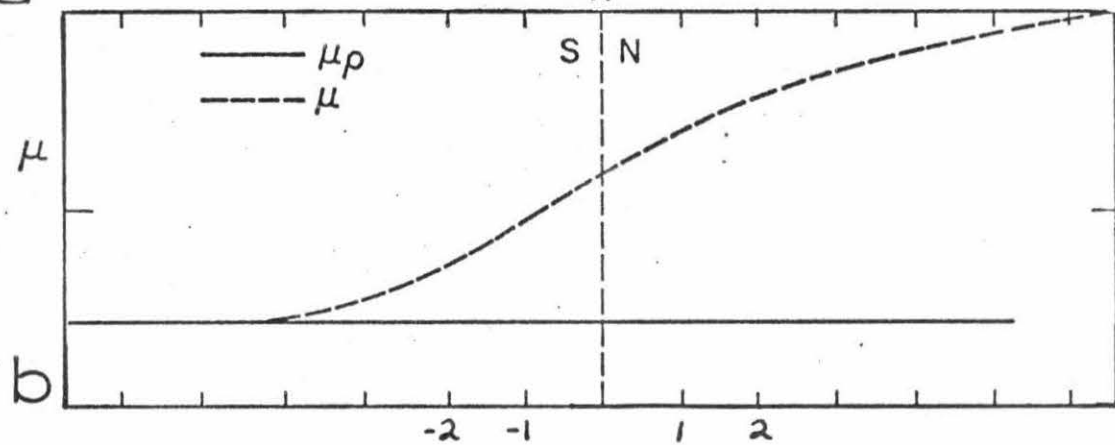
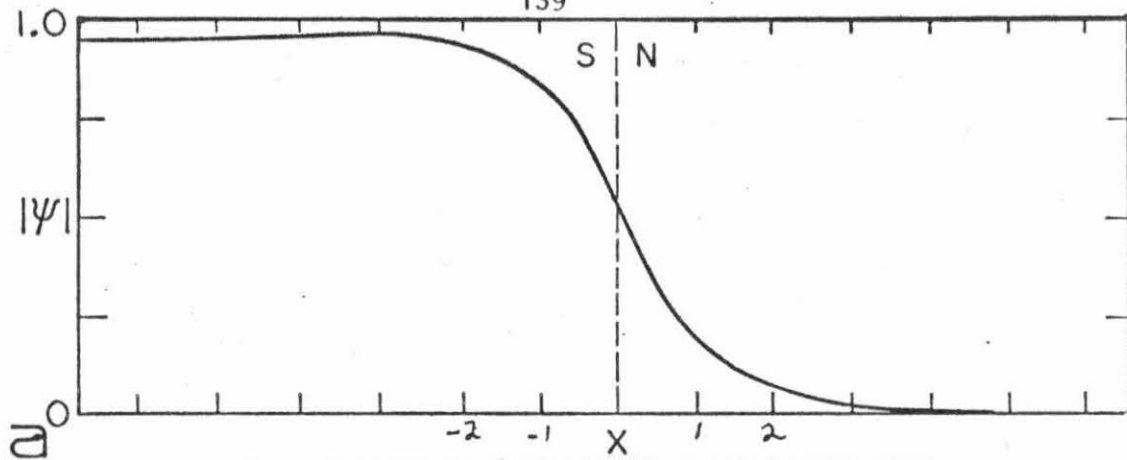
It has been proposed<sup>22</sup> that a weakly superconducting bridge may be viewed as two such boundaries "back to back", that is a super-normal interface followed closely by a normal metal-superconductor interface. The necessary feature is, of course, that the tails of the macroscopic wave functions, extending into the normal material will overlap. In the center of the bridge there will be a certain number of pairs whose phase and pair potential comes from the right side of the bridge, while the phase and pair potential for the remaining pairs will come

Fig. 4-9. Behavior of  $|\psi|$ ,  $\mu_e$ ,  $\mu_p$ ,  $j_s$  and  $j_n$  at a superconducting-normal interface. The units on the horizontal axes are the coherence length of the superconductor.

Fig. 4-9a indicates the wave function extends a considerable distance into the normal material, an example of the proximity effect.

Fig. 4-9b indicates the behavior of the chemical potential of the pairs,  $\mu_p$ , and that of the electrons,  $\mu_e$ , through the S-N boundary. The two chemical potentials are no longer in equilibrium due to the divergence of the supercurrent imposed by the boundary with the normal material.

Fig. 4-9c indicates the normal current generated by the gradient in the chemical potential of the electrons. The figure also shows the decay of the supercurrent near the boundary. These quantities are given for two values of  $j$ ;  $0.29 j_c$  and  $0.95 j_c$ .



from the left side of the bridge. This is illustrated in Fig. 4-10a.

The supercurrent due to the overlap of two such wave functions,  $\psi_1 e^{i\phi_1}$  and  $\psi_2 e^{i\phi_2}$  has been calculated.<sup>23,24</sup>

$$j_s = j \sin(\phi_1 - \phi_2) + \beta \nabla \phi (1 + \cos(\phi_1 - \phi_2)) \quad , \quad (4.21)$$

where  $\beta$  is a constant and where  $\nabla \phi = \nabla \phi_1 = \nabla \phi_2$ . The gradients of the phase on the two sides must be equal to conserve linear momentum. This supercurrent will exhibit quantum interference - the first term is the usual Josephson effect and the second is an interference term which originates from the phase dependent  $(\phi_1 - \phi_2)$  amplitude modulation of overlap wave function  $\psi_1 + \psi_2$ . Yu<sup>23,20</sup> has experimentally confirmed several aspects of this model. Of particular importance to this discussion, he found the chemical potential for electrons to vary smoothly across the junction.

For currents above the critical current of the junction the spatial variation of the wave function in the interior of a proximity effect junction will produce a strong divergence in the supercurrent,  $j_s$ , as discussed previously. And this divergence will result in a difference between the chemical potentials of pairs and electrons at each interface. The fundamental assumption is that as in the case of a single normal metal-superconductor interface, the pair retains the value of the potential associated with the superconductor of its origin. There is, however, a net potential difference between the superconductors,  $2eV$ . The pair potentials in the center region where the wave functions overlap are therefore separated by this amount.

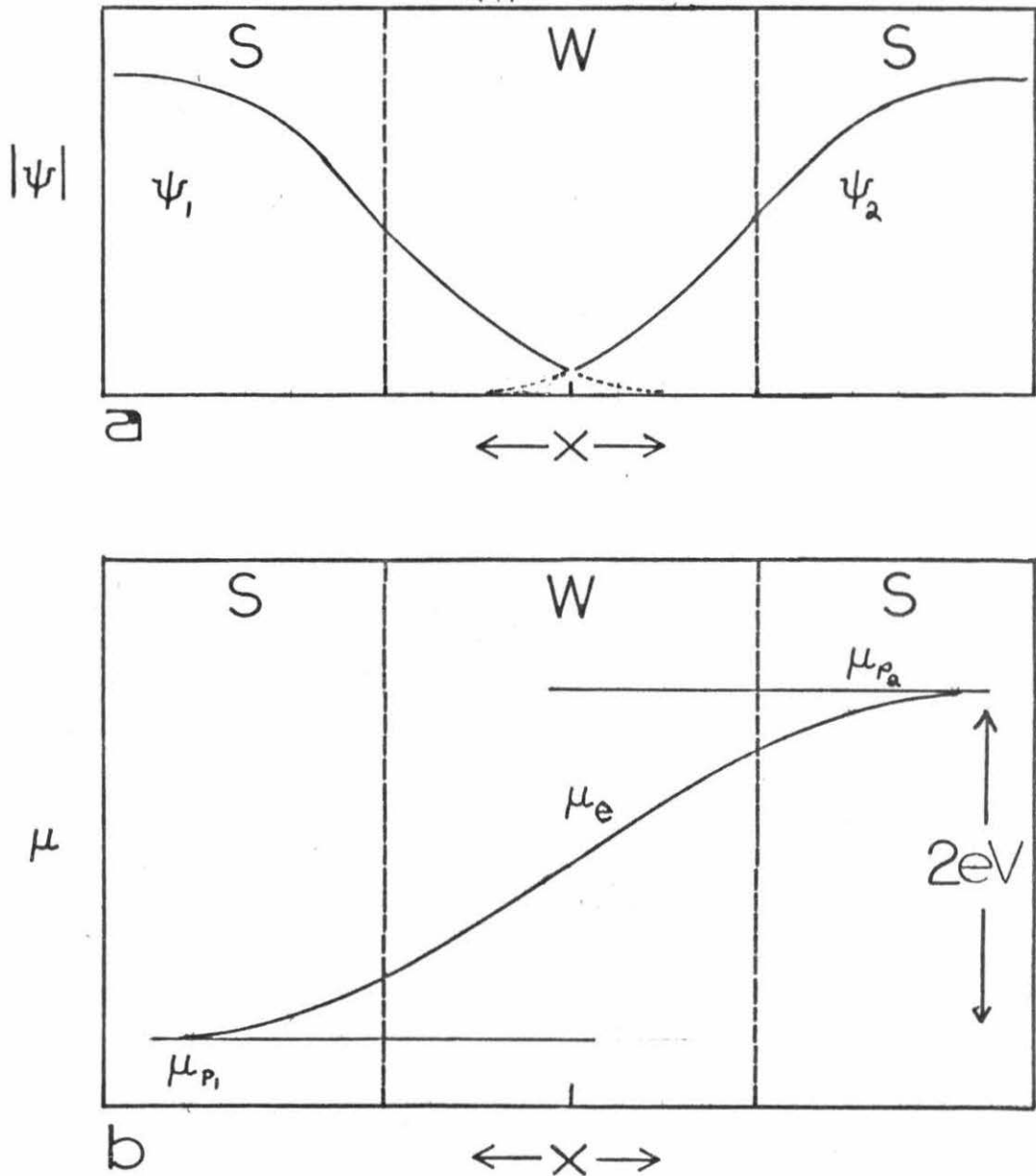


Fig. 4-10. A schematic representation of the behavior of a proximity effect bridge proposed in the text. The overlap of the two wave junctions  $\psi_1$  and  $\psi_2$  is shown in 4-10a, while the proposed existence of two pair potentials is shown in 4-10b.

This situation is pictured in Fig. 4-10b. Thus we have approximated an extremely complex physical situation as a single normal electronic state  $\mu_e$  and two pair states; one with phase  $\phi_1$  and potential  $\mu_1$  and another characterized by  $\phi_2$  and  $\mu_2$ . In the center region the current is composed of two parts: a normal electron flow proportional to  $\nabla\mu_e$  and a pair current earlier described in Eq. (4.21).

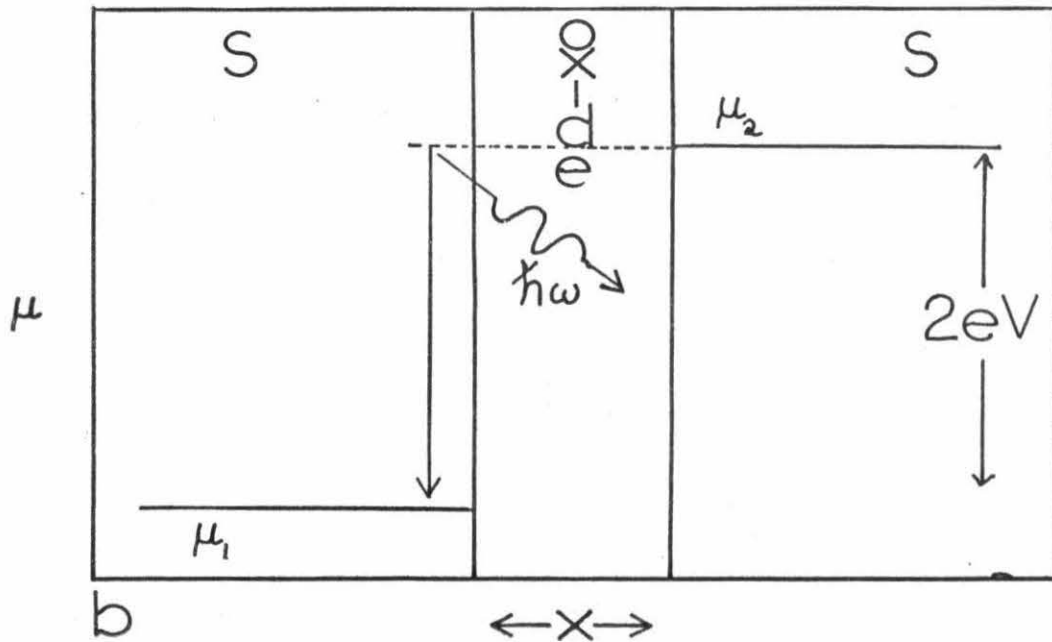
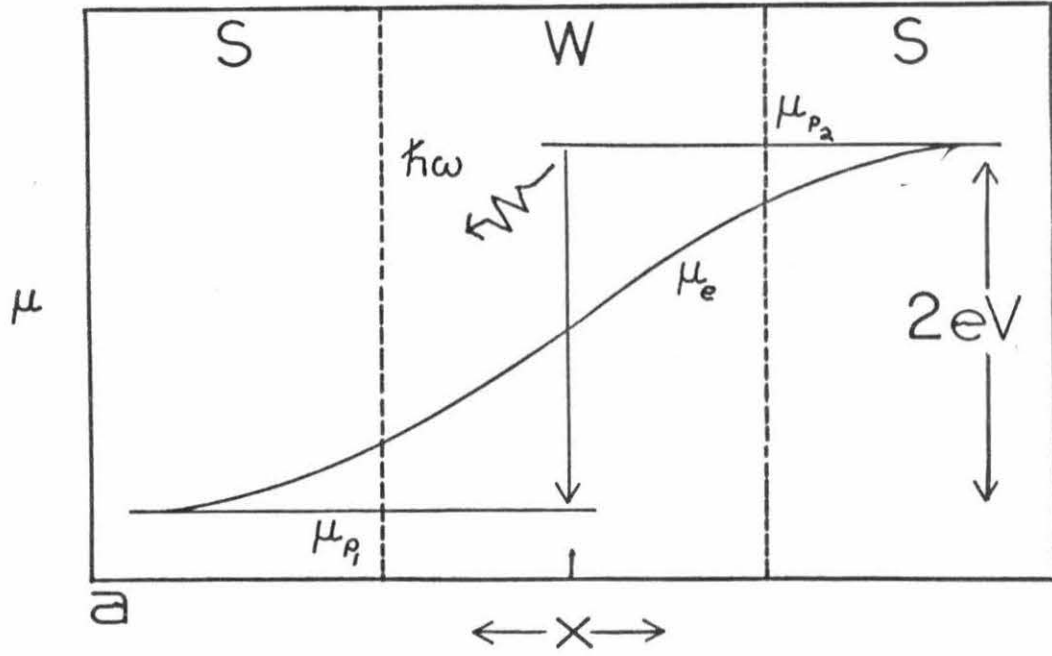
In this model the transit of a pair through the bridge then requires a transition between two pair states within the overlap region, one at potential  $\mu_1$ , to a second at potential  $\mu_2$ . Conceptually this situation is then somewhat similar to pair transfer processes occurring across insulating tunnel junctions except that in this case the transition is between two coincident pair states at different pair potentials (but identical chemical potential); while in the tunnel junction the two separate pair states are separated by an insulating barrier which supports a difference in chemical potential. To proceed, we adopt this model with no further justification and determine the experimental consequences (with regard to noise) in a manner similar to that used in the tunnel junction analysis. We assume that transition between pair states is direct and must be accompanied by the emission or absorption of a quantum of energy  $\hbar\omega = 2eV$ , probably a phonon. The supercurrent is the sum of pairs crossing the bridge per unit time. The probability that a pair makes a transition depends not only upon the density of initial and final pair states but also upon the density of states available for the phonon. Fluctuations in the number of phonons due to the finite temperature of the surrounding matter will be

reflected into fluctuations in the pair transition probabilities and hence into the supercurrent. The origin of the fluctuations in the supercurrent lies in the random decay, i.e. shot noise, of the phonons in the surrounding material on the same way as the random decay of photons causes supercurrent fluctuations (i.e. noise) in a superconducting tunnel junction.

For the Josephson tunnel junction a detailed calculation has been done by Stephen.<sup>6</sup> The pairs tunnel through the oxide barrier from one superconductor to the other. Upon tunneling they must emit or absorb a quantum of  $2eV$  (a photon in this case) to come into equilibrium with the potential of the superconductor on the other side. This is illustrated in Fig. 4-11. The dissipation of these photons is again a random process giving rise to fluctuations in the number of photons present. These fluctuations around the average value will again introduce noise into the supercurrent. Since the statistics of phonons and photons are the same if we adopt the Debye model for the density of phonon states, and if we assume the important parameter determining the pair transition is the energy difference,  $2eV$ , between the initial and final states (rather than the exact character of the state itself), then the fluctuations introduced into the supercurrents in both cases (tunnel junction and proximity effect bridge) will have the same functional form, in terms of experimental parameters. Stephen has performed an exact calculation for the fluctuations in the supercurrent in a tunnel junction which we will apply to the supercurrents in our conducting junctions due to the physical similarities discussed above. Stephen<sup>6</sup>

Fig. 4-11. Illustration of the pair transition process proposed in the text. Fig. 4-11a illustrates the process in a proximity effect bridge. A pair initially in the state characterizing the right hand superconductor  $\psi_2$ , has a pair potential  $\mu_2$ . As the pair passes through the bridge, it must come into equilibrium with the state  $\psi_1$  and potential  $\mu_1$  existing in the left hand superconductor. The pair must lose energy  $2eV$ , the difference in the pair potentials. The proposed process is for the pair to emit a phonon during this transition.

Fig. 4-11b illustrates the analogous situation for a tunnel junction. A pair tunnels through the oxide barrier to the other superconductor. Again it must emit or absorb an energy  $2eV$ , in this case in the form of a photon.



finds the power spectrum of the supercurrent fluctuations to be

$$P_S(f) = 4e I_S(V_0) \coth(eV_0\beta) \quad . \quad (4.22)$$

Where  $I_S$  is the time average supercurrent,  $\beta = kT$ , and  $V_0$  is the dc potential between final states and the device. Our data are all taken in the limit  $eV_0 \ll kT$ . In this limit the above expression reduces to:

$$P_S(f) = 4kT I_S/V_0 \quad . \quad (4.23)$$

The voltage spectrum  $S_S(f)$  produced by this current spectrum is:

$$\frac{4kTR_d^2 I_S}{V_0} \quad , \quad (4.24)$$

where  $R_d$  is just the dynamic resistance, the small signal response of the system. It is important to realize that while this fluctuation spectrum is calculated from a pair tunneling current model, the physics it represents, that of a transition rate between two pair potentials in equilibrium with the dissipation of the emitted quanta, is more general than the tunnel junction model.

To obtain the total power spectrum  $S_T(f)$  of the voltage fluctuations in the device we add the contributions of the superfluid and normal currents.

$$S_T(f) = S_S(f) = S_N(f) \quad , \quad (4.24)$$

$$S_T(f) = \langle V(f)^2 \rangle = 4kTR_d^2 \left[ \frac{I_S}{V_0} + \frac{I_N}{R} + \frac{I_C^2}{2R(2I-I_C)^2} \right] \quad . \quad (4.25)$$

The first term is the contribution from the superfluid flow; the second term is due to the interaction of the normal flow and the lattice and is given by the familiar Nyquist expression; the third term is due to the effect of the non-linear oscillatory shunt element on the normal fluid flow. In the two fluid model, the voltage across the device is just the normal current times the resistance of the bridge.

$$V = I_N R = (I_T - I_S) R$$

Making this substitution we obtain:

$$\langle V^2(f) \rangle = 4kT R_d^2 \left[ \frac{I_T}{V_0} + \frac{I_c^2}{2R(2I_T - I_c)^2} \right] \quad (4.26)$$

As we saw in the first chapter the solution of the phase slip model, Eq. (1.21), gives an analytic form for the I-V characteristics of the device.

$$V_0 = R(I_T^2 - I_T I_c)^{1/2} \quad (1.21)$$

Making this substitution for  $V_0$  in Eq. (4.26) and expanding both terms in  $I/I_c$  allows a comparison of the magnitudes of the two terms. For currents above the critical current, to second order in  $I_c/I$ :

$$I_T/V = \frac{I}{R} \left( 1 + \frac{1}{2} \frac{I_c}{I_T} + \frac{3}{8} \frac{I_c^2}{I_T^2} + \dots \right) \quad (4.27)$$

$$\frac{I_c^2}{2R(2I_T - I_c)^2} - \frac{I}{R} \left( \frac{1}{8} \frac{I_c^2}{I_T^2} + \dots \right) \quad , \quad (4.28)$$

we see that the term due to the mixing of the normal noise by the non-linear shunt is always much smaller than the term due to fluctuations in the currents

$$\frac{I}{V} > \frac{I_c^2}{2R(2I - I_c)} \quad . \quad (4.29)$$

We shall neglect the term on the right in what follows. The total voltage power density spectrum becomes

$$\langle V^2(f) \rangle = 4kT \frac{R_d^2}{V/I} \quad . \quad (4.30)$$

It should be noted that this expression has no adjustable parameters; all quantities are measurable. The temperature of the bridge is taken to be the bath temperature since Palmer<sup>22</sup> has shown that for these bridges on sapphire the temperature is elevated only 0.01°K for 100  $\mu$ A of bias current.

In Fig. 4-8 we compare this expression to the noise data presented in the upper traces of Fig. 4-5 using measured values for  $R_d$ ,  $I$ ,  $V$ ,  $T$ . The fit is seen to be excellent. Error bars are indicated for the noise points. Since the predictions depend upon separate measurements of  $I$ ,  $V$ , and  $R_d$ , there are error bars associated with the prediction

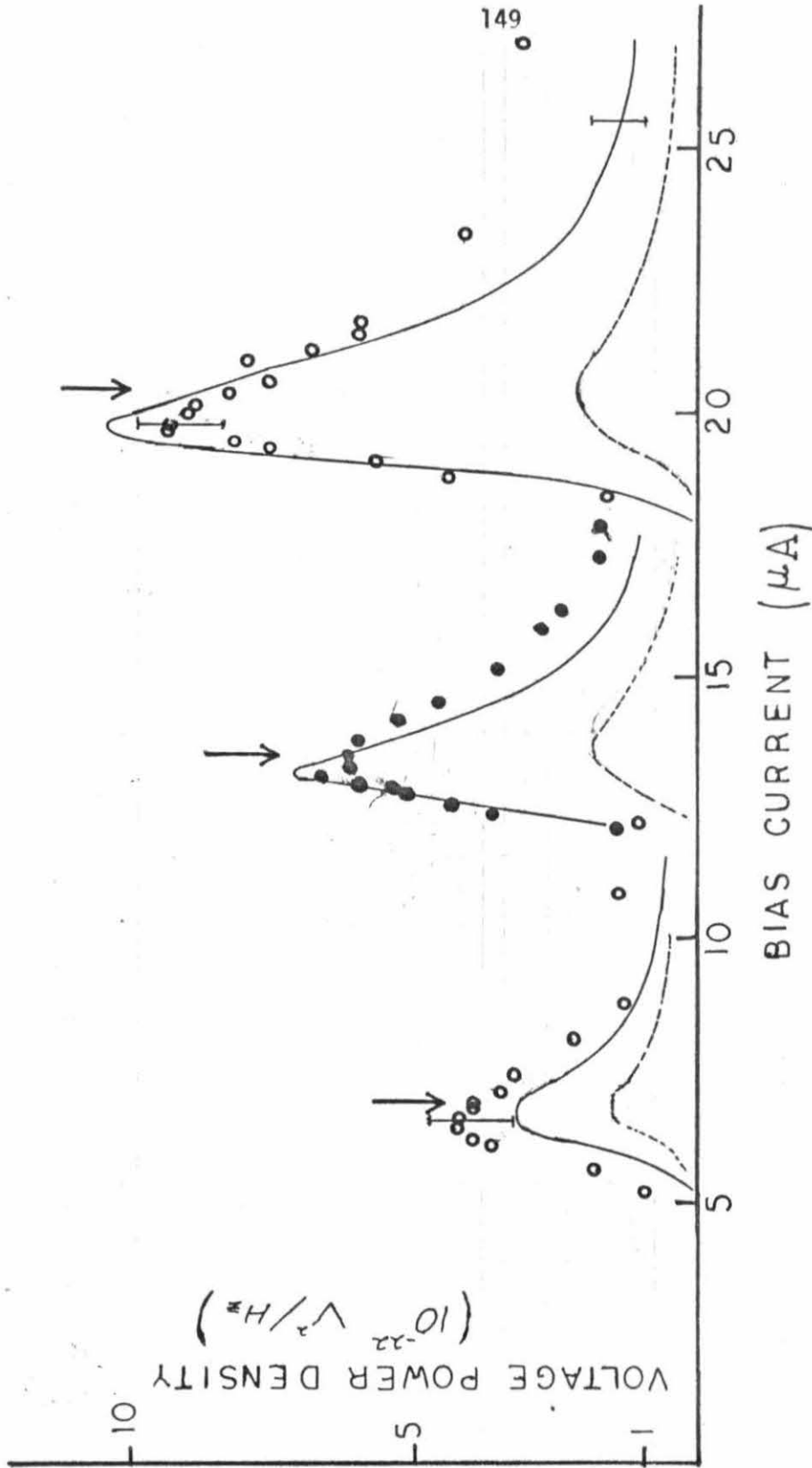


Fig. 4-8. Voltage power density as a function of bias current. The points are experimental data taken from the upper traces of Fig. 4-5. The solid traces are predicted on the basis of noise in the normal and supercurrents. The dashed curves are the predictions based on noise mixing in the normal currents and do not match the experimental data in magnitude or functional form. The arrows indicate the peaks in the corresponding dynamic resistance characteristics. Error bars are indicated for the points and the predictions.

as well.

The predicted maxima in the noise power density are seen to match the measured values quite well. The corresponding maxima in the dynamic resistance measurements are indicated by the arrows. In the high current limit  $R_d$  goes to  $R$ , the normal state resistance, while  $V/I$  approaches this limit from below. This behavior yields a noise power of

$$S_T(f) = 4kTR \quad , \quad (4.31)$$

at currents large compared to the critical current.

With reference to Fig. 4-12, the observed features of the noise power around a step may be qualitatively examined. The peaks in the dynamic resistance are reflected into the noise power in the same way as was the case at the critical current. In the center of the step the dynamic resistance is zero, yielding zero noise voltage. Since the voltage is constant across the step, the quantity  $V/I$  decreases as current is increased across the step and will be smaller at the peak in the noise power on the high current side, making this peak larger in noise power than the corresponding peak on the low current side, as was seen in Fig. 4-7.

The excellent qualitative and quantitative agreement between our noise data and the expression for the voltage fluctuations Eq. (4.30) substantiates the concept of noise in the supercurrent flow through the device. This expression is the sum of fluctuations in the normal current flow and the supercurrent flow. As indicated in Fig. 4-8

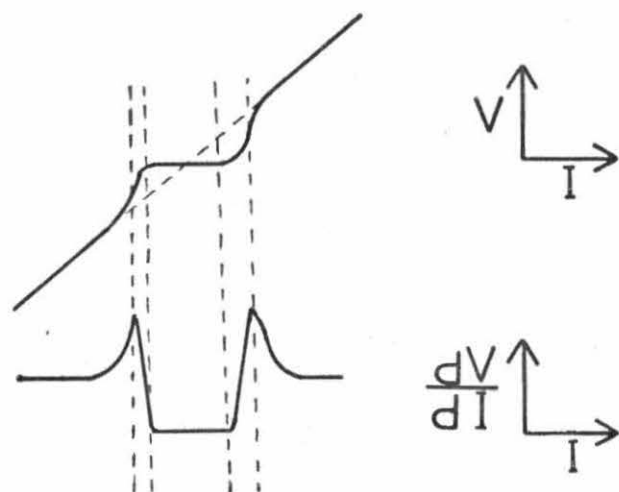


Fig. 4-12. Detail of an rf induced step in the characteristics of a proximity effect bridge. Upper trace is the step as it appears in the current voltage characteristic. Lower trace is the dynamic resistance as a function of bias current for the same step. The center of the step corresponds to zero dynamic resistance.

the fluctuations in the normal currents are not sufficient to account for the observed fluctuations, either in magnitude or in functional form. The agreement achieved by utilizing the supercurrent fluctuations derived for the case of tunneling supercurrent may, in turn, help support the physical arguments used to justify the procedures. In particular, the agreement between experimental evidence and predicted fluctuations may be viewed as additional experimental in favor of the overlapping wave function model of a proximity effect bridge.

The expression for our current fluctuations is the same as Kirschman's <sup>12</sup> in the limit of currents high compared to the critical current. However our large noise peak near the critical current is not in agreement with his expression. The measurements however are not inconsistent with a small increase in noise power (a factor of two in linewidth) near the critical current. His measurements involved junctions of very low impedance (1-10 m $\Omega$ ) for critical currents of 30  $\mu$ A to 300  $\mu$ A. In this range, the quantity  $R_d^2 \left[ \frac{4kTI}{V} \right]$  will yield expected values for the noise maxima of magnitude less than or equal to those observed in Fig. 4-8.

#### 4.10 Effect of Substrate

Clarke and Hawkins<sup>9</sup> have measured the low frequency ( $10^{-2}$  Hz - 10 Hz) voltage fluctuations across a shunted tunnel junction on a glass substrate. They find a strong  $1/f$  dependence in the power spectrum and show that it can be described by considering the effect of equilibrium temperature fluctuations  $\langle \Delta T^2(t) \rangle = kT^2/C_V$ , on the critical current. These temperature fluctuations will cause voltage fluctuations through the temperature dependence of the critical current. The voltage fluctuations are given

$$\langle V^2(f) \rangle = \left( \frac{\partial V}{\partial I_c} \right)^2 \left( \frac{\partial I_c}{\partial T} \right)^2 \frac{kT^2}{GC_V} 1/f, \quad (4.32)$$

where  $I_c$  is the critical current,  $C_V$  is the total heat capacity associated with the junction, and  $G$  is a geometrical factor of roughly three. Since the characteristic volume of a proximity effect bridge is approximately  $10^4$  times smaller than that of such a tunnel junction, such an effect would produce a very large  $1/f$  contribution to the noise spectrum that extended to much higher frequencies. As discussed above for the Nb/Ta/sapphire and Ta/Ti/sapphire bridges the observed fluctuation spectrum was white and with magnitude

$$\langle V^2(f) \rangle = 4kT R_d^2 \frac{V}{I} \quad (4.30).$$

No evidence of  $1/f^n$  fluctuations was seen.

The absence of  $1/f$  noise can be attributed to the excellent thermal

contact between film and substrate  $(1 - 8 \text{ watts/cm}^2 \text{ } ^\circ\text{K})^{22}$  and the very high thermal conductivity of the sapphire

$$\left( \frac{5 \times 10^{-2} \text{ cal}}{\text{sec-cm } ^\circ\text{K at } 2^\circ\text{K}} \right)$$

for our devices. To test this hypothesis two bridges were constructed from Ta/Ti/glass parent material. These bridges showed strong  $1/f^n$  behavior with  $1.5 < n < 2.0$ . These measurements are summarized in Fig. 4-13.

The set of points labeled, (a), is the noise power for the bridge on glass at a critical current  $I_c$  of  $5 \mu\text{A}$ . The line (b) is the predicted noise power due to Eq. (4.30) in this junction at this temperature and critical current. The data fit a  $1/f^2$  dependence quite well until near the predicted shot noise level.

The data labeled (c) are the measured frequency spectrum and the noise prediction from Eq. (4.30) for the Ta/Ti/sapphire bridge, showing a flat spectrum and reasonable agreement for a critical current of  $4 \mu\text{A}$ . At higher critical currents for the Ta/Ti/glass bridge both the data and the shot noise prediction are increased: (d) and (e). The effect of substituting glass substrates for sapphire is to generate a strong  $1/f^n$ , excess noise spectrum with  $n \sim 1.5-2$ , extending well into the audio frequencies ( $\sim 1000 \text{ Hz}$ ), possibly due to the effect of temperature fluctuations in the volume of the device. This noise is obviously of limited bandwidth and contributes little total energy to the device, although the low frequency measurements will obviously be adversely affected.

Fig. 4-13. Effect of substrate upon voltage fluctuations in proximity effect bridges. Voltage spectral power density is plotted as a function of frequency.

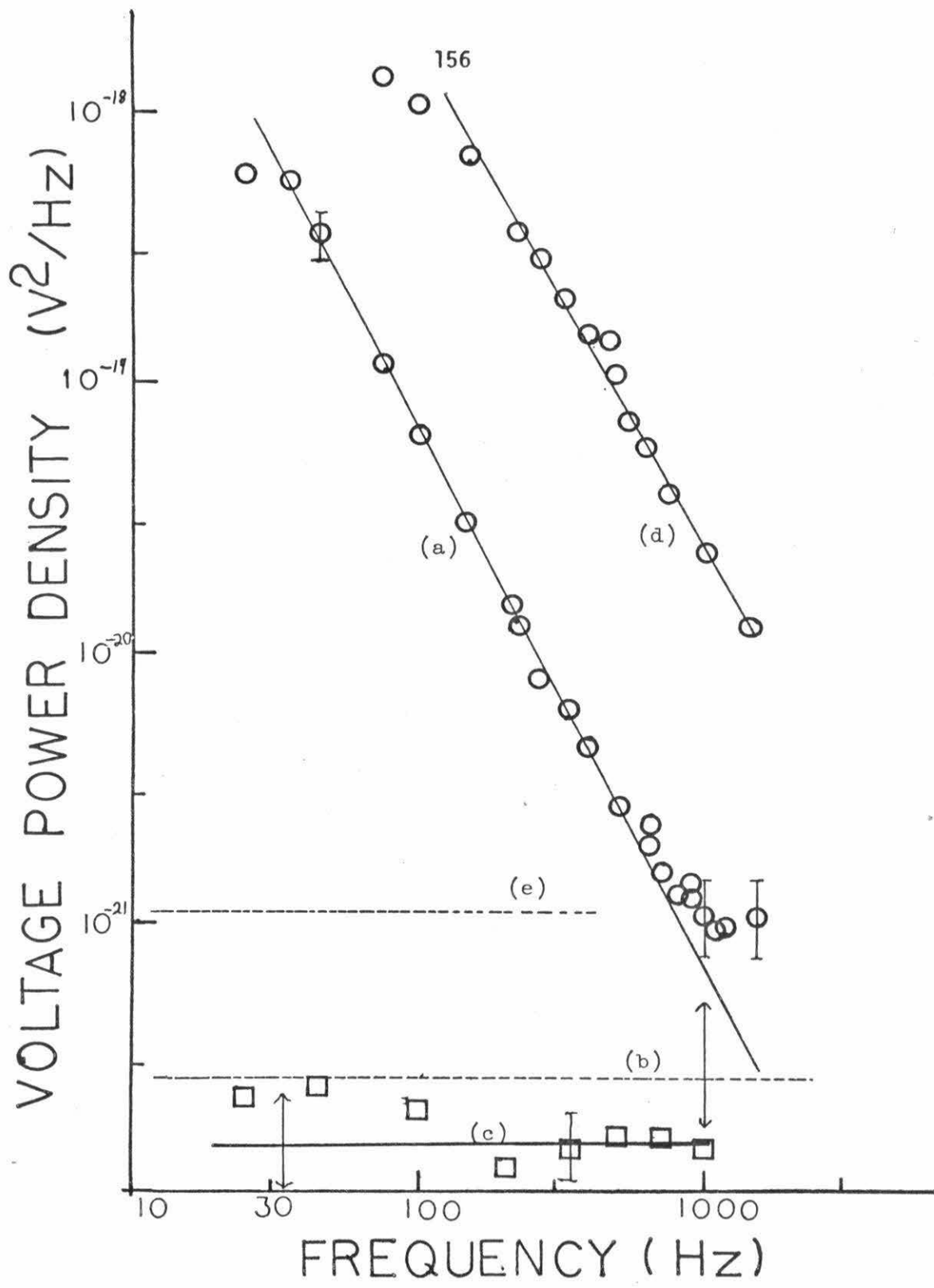
The points of trace (a) are the power spectrum measured on a Ta/Ti/glass bridge biased to the maximum in the noise power. Trace (b) is the predicted value for the fluctuations in the normal and supercurrents for this bridge  $\langle V^2(f) \rangle = 4kTR_d^2 \frac{I}{V}$ . The experimental points are seen to be approximately given by the sum of (b) and line (a).

The experimental points (d) are the power spectrum for the same bridge at a higher critical current. The prediction for this case is given by (e).

The square data points are the measured spectrum for a Ta/Ti/sapphire bridge. The predicted spectrum from the expression  $\langle V^2(f) \rangle = 4kTR_d^2 I/V$  is indicated by trace (c).

In all cases uncertainties in data are indicated by bars and uncertainties in the predictions by arrows.

The change of substrate from sapphire to glass is seen to introduce an additional noise source with a  $1/f^n$  dependence. In this case  $n \sim 2$ .



#### 4.11 Summary

We have investigated the spectral density of the voltage fluctuations across proximity effect bridges, as a function of bias current with temperature, critical current, magnetic field, and incident radiation as parameters. The spectral density is found to be flat in the frequency range investigated (20 - 2000 Hz). The voltage fluctuations were found to be material independent for the two proximity effect systems examined, Nb/Ta and Ta/Ti. The voltage fluctuations at a given frequency depend strongly upon the bias current through the device, exhibiting a pronounced maxima for currents slightly larger than the critical current.

The measured voltage fluctuations have been found to be in excellent agreement, qualitative and quantitative with the power density spectrum obtained by considering fluctuations in both the normal current and the supercurrent through the bridge. The fluctuations in the normal current, due to the interaction with the lattice are given by the usual expression for Nyquist noise. The fluctuations in the supercurrent were found to be governed by a process by which a pair changed from a quantum state characteristic of one of the strong superconductors to a quantum state characterizing the other.

The spectral density of the voltage fluctuations in the proximity effect bridges were found to match those predicted by

$$\langle V(f)^2 \rangle = 4kTR_d^2 I/\bar{V} \quad (4.30)$$

where  $I$  is the total current,  $V$  the time average voltage across the device, and  $R_d$  the dynamic resistance.

The above results hold as long as the proximity effect bridge is well anchored thermally to the sapphire substrate. If the bridges are fabricated on glass substrates, effectively reducing their specific heats, then a strong contribution to the fluctuations with a  $1/f^2$  dependence is observed. This additional term in the voltage power spectrum at low frequencies is the result of thermodynamic temperature fluctuations producing fluctuations in the critical current of the bridge.

## Appendix A

DERIVATION OF TRANSFER IMPEDANCE AND NOISE MIXING FOR A  
RESISTIVELY SHUNTED PROXIMITY EFFECT BRIDGE

We wish to calculate the transfer impedance for the circuit shown in Fig. A1, consisting of a normal resistor R shunted by a non-linear oscillatory, superconducting, element whose characteristics are given by the equations

$$I_S = \frac{I_C}{2} (1 + \cos \phi) \quad , \quad (A-1)$$

and

$$\hbar \dot{\phi} = 2eV \quad , \quad (A-2)$$

where V is the voltage across the device,  $I_C$  is the critical current, and  $\phi$  is the quantum phase difference across the device. We will follow the calculations of Likharev and Semenov.<sup>†</sup>

Initially, we wish to know the transfer impedance for small signals,  $Z_{kk'}$ , that is, the voltage response of the system at frequency k to a small current of frequency k'.

$$V_k = i_{k'} Z_{kk'} \quad . \quad (A-3)$$

†

The author gratefully acknowledges the guidance of notes provided by Dr. D. J. Scalapino on this problem and the assistance of Dr. R. H. Wang in performing this calculation.

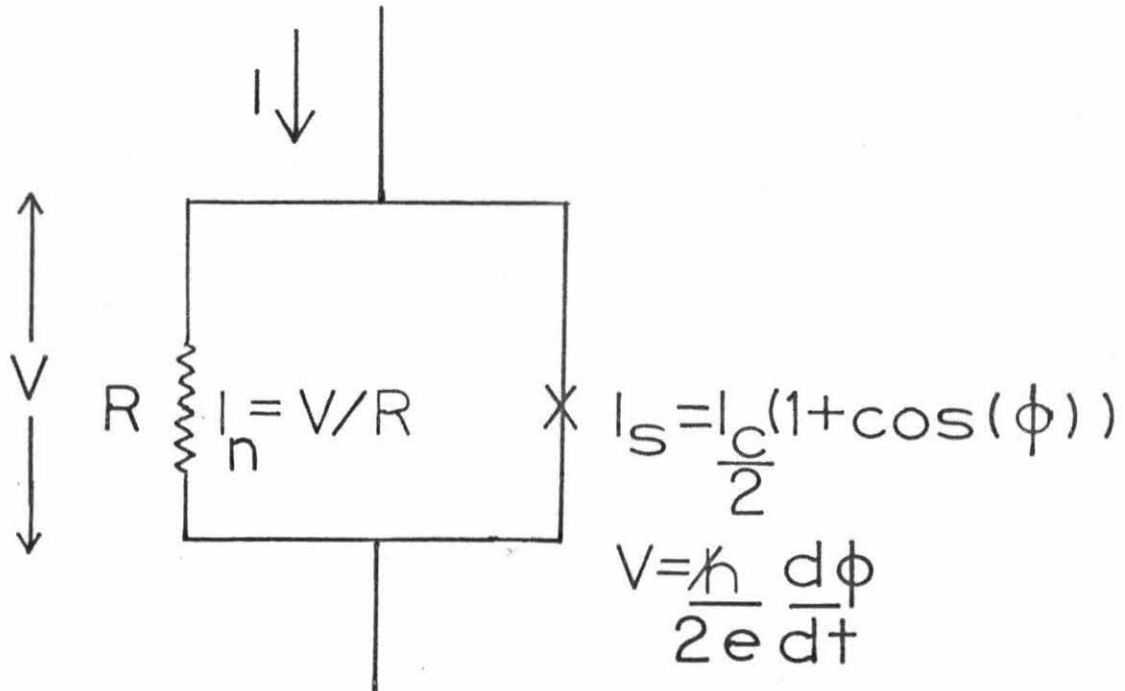


Fig. A-1. Equivalent circuit of proximity effect bridge utilized for calculation of noise mixing.

To find the effects of noise mixing we will sum the square of Eq. (A-3) over all frequencies assuming the current noise source uncorrelated at all frequencies and phases. This will yield the voltage power spectrum as a function of the current power spectrum.

If the total current through the circuit is  $I$  then

$$\frac{V}{I} + \frac{I_C}{2} (1 + \cos \phi) = I \quad , \quad (A-4)$$

where we have expressed the current as the sum of the super and normal flows. We transfer to reduced units to facilitate the calculation,

$$i = \frac{I}{I_C}$$

and  $t$  measured in units

$$t_0 = \frac{\hbar}{2eRI_C}$$

Equation (A-4) becomes

$$\dot{\phi} + \frac{1}{2} (1 + \cos \phi) = i \quad , \quad (A-5)$$

Since we are interested in small deviations from the dc current bias we first solve for the response  $\phi_0$  to the direct current  $i_0$ ,

$$\dot{\phi}_0 = \frac{2v^2}{(2i_0 - 1) - \cos vt} \quad , \quad (A-6)$$

where

$$v = \sqrt{i_0(i_0 - 1)} = \dot{\phi}_0 \quad . \quad (A-7)$$

$V$  is just the dc time average voltage across the device in reduced units  $v = \bar{V}/I_C R$ . The I-V characteristics given by Eq. (A-7) fit the experimentally measured characteristics of a proximity effect bridge very well. In Eq. (A-6) the phase choice resulting in the  $\cos vt$  term is made for convenience in determining the harmonic content of this expression. This harmonic analysis is given by

$$\dot{\phi}_0 = v \left[ 1 + 2 \sum_{m=1}^{\infty} (2i_0 - 1 - 2v)^m \cos mvt \right] \quad . \quad (A-8)$$

Now we let  $i = i_0 + i_1$  which will cause a response  $\phi = \phi_0 + \phi_1$ . The initial equation becomes

$$\dot{\phi}_0 + \dot{\phi}_1 + \frac{1}{2} \left( 1 + \cos(\phi_0 + \phi_1) \right) = i_0 + i_1 \quad ,$$

expanding for small values of  $\phi_1$  we obtain an equation for  $\phi_1$ .

$$\dot{\phi}_1 - \frac{1}{2} \phi_1 \sin \phi_0 = i_1 \quad . \quad (A-9)$$

This is a first order differential equation and may be solved by use of an integrating factor which yields

$$\phi_1(t) = \dot{\phi}_0(t) \int_{t_0}^t \frac{i_1(t')}{\dot{\phi}_0(t')} dt' \quad (A-10)$$

We first wish to investigate the linear response of  $\phi_1(t)$  to  $i_1 = i\omega e^{-j\omega t}$ . Substituting this into (A-10) and combining with (A-6) and (A-8)

$$\phi_1(t) = \frac{-ji\omega}{2v} \sum_{k=-\infty}^{\infty} e^{-j(\omega+kv)t} \left[ \frac{\beta}{\omega} \alpha^{|k|} + \frac{a^{|k-1|}}{2(\omega+v)} + \frac{a^{|k+1|}}{2(\omega-v)} \right] \quad (A-11)$$

where

$$\beta = 1-2i_0 \quad \text{and} \quad \alpha = (2i_0 - 1 - 2v)$$

What we are truly interested in is the sum of such responses to currents at many frequencies. That is, we want the linear response to  $i_1 = \sum_{\omega} i\omega e^{-j\omega t}$ . Summing the expression (A-11) over  $\omega$  and making the substitution  $\Omega = \omega + kv$  we obtain after taking a time derivative, an expression for the voltage response

$$v_{\Omega} = -j\Omega\phi_{\Omega} = \frac{\Omega}{2v} \sum_{\phi} i_{\Omega-kv} Z_k \quad (A-12)$$

with

$$Z_k = \frac{\beta}{\Omega - kv} \alpha^{|k|} + \frac{\alpha^{|k-1|}}{2(\Omega - (k-1)v)} + \frac{\alpha^{|k+1|}}{2(\Omega - (k+1)v)} \quad (A-13)$$

Take the square of this expression to get the noise power density. We assume that the  $v_\Omega$  and  $i_\omega$  are all uncorrelated

$$\begin{aligned} P_V(\Omega) &\equiv |v_\Omega|^2 = \left(\frac{\Omega}{2V}\right)^2 \sum_{k=-\infty}^{\infty} |Z_k|^2 |i_{\Omega - kv}|^2 \\ &\equiv \sum |Z_k|^2 P_i(\Omega - kv) \end{aligned} \quad (A-14)$$

If we are interested in the low frequency spectrum of the fluctuations, the limit  $\Omega \rightarrow 0$ , only three terms,  $k = 0$ ,  $k = 1$ ,  $k = -1$  in  $Z_k$  remain as they go as  $\Omega^{-1}$  rather than  $[\Omega + \text{const}]^{-1}$

$$P_V(\Omega \sim 0) = \left(\frac{1}{2V}\right)^2 \left[ P_i(0)(1 - 2i_0)^2 + P_i(v) \frac{1}{2} \right] \quad (A-15)$$

To convert this into real units we recognize

$$i_0 = I_0/I_C, \quad v = \frac{V}{I_C R}, \quad P_i(\Omega) = \frac{2eR P_I(\Omega)}{\hbar I_C}, \quad \text{and } P_V(\Omega) = P_I(\Omega) \frac{2e}{\hbar R I_C}$$

Substituting into (A-15) and making the approximation

$$P_I(0) \sim P_I(\Omega) = \frac{4kT}{2\pi R}$$

that is, the noise currents are due to Nyquist noise in the resistor R

$$P_V(\Omega \sim 0) = \frac{4kTR}{2\pi} \left[ 1 + \frac{3}{8} \frac{I_C^2}{I_0(I_0 - I_C)} \right] \quad , \quad (A-16)$$

but

$$V_0 = R \sqrt{I_0(I_0 - I_C)}$$

$$\frac{dV_0}{dI_0} = R_d = \frac{R^2(2I_0 - I_C)}{2V_0}$$

Substituting into (A-16) we obtain

$$P_V(\Omega \sim 0) = \frac{4kTR_d^2}{2\pi R} \left[ 1 + \frac{I_C^2}{2(2I_0 - I_C)^2} \right] \quad . \quad (A-17)$$

This is the power spectrum of the voltage fluctuations in a resistor in parallel with superconducting element which characterizes the supercurrent flow in a proximity effect bridge. We see that the voltage spectrum is modified from the case of a resistor without such a shunt element. It should be emphasized, however, that in this model the shunt element representing the supercurrent flow, does not contribute to the fluctuations but causes current fluctuations near the frequency of bridge  $\omega = \frac{2eV}{\hbar}$  to appear as voltage fluctuations at the low frequencies of our measurements.

## REFERENCES

Chapter 1

1. F. London, Superfluids, Vol. 1, New York, John Wiley & Sons (1950).
2. J. E. Mercereau, Superconductivity, Vol. I (Parks, Ed.) p. 393 (1969).
3. R. P. Feynman, Lectures on Physics, Vol. III, Chapter 21, Addison-Wesley (1965).
4. J. Bardeen, L. N. Cooper, and J. R. Schrieffer, Phys. Rev. 108, 1175 (1957).
5. D. J. Scalapino, Tunneling Phenomena in Solids, (Burstein and Lundquist, Ed.) p. 477 (1969).
6. R. Meservey and B. B. Schwartz, Superconductivity, Vol. I (Parks, Ed.) p. 174 (1969).
7. W. Meissner and R. Ochsenfeld, Naturwiss, 21, 787 (1933).
8. R. Doll and M. Nábauer, Phys. Rev. Letters, 7, 51 (1961).
9. B. S. Deaver, Jr. and W. M. Fairbank, Phys. Rev. Letters, 7, 43, (1961).
10. B. D. Josephson, Phys. Lett. 1, 251 (1962).
11. J. E. Mercereau, Tunneling Phenomena in Solids, (Burstein, Ed.) p. 461 (1969).
12. D. N. Langenberg, Tunneling Phenomena in Solids, (Burstein, Ed.) p. 519 (1969).
13. John Clarke, Proc. IEEE, 61, 8 (1973).

14. John Clarke, Proc. Roy. Soc., Ser. A, 308, 447 (1969)'
15. C. L. Huang and T. van Duzer, Applied. Super. Conf. Paper M-6, Oakbrook, Ill., Sept 30-Oct. 2, 1974.
16. H. A. Notarys and J. E. Mercereau, J. Appl. Phys. 44, 1821 (1973).
17. David William Palmer, H. A. Notarys, and J. E. Mercereau, Appl. Phys. Lett. 25, 526 (1974).
18. M. A. Janocko, J. R. Gavales and C. K. Jones, Applied S. C. Conf., Paper R-12, Oakbrook, Ill., Sept 30-Oct. 2, 1974.
19. E. P. Harris, Applied Super. Conf. paper M-12, Oakbrook, Ill. Sept. 30-Oct. 2, 1974.
20. T. J. Reiger, D. J. Scalapino, and J. E. Mercereau, Phys. Rev. B, 6, 1734 (1972).
21. R. K. Kirschman, H. A. Notarys, and J. E. Mercereau, Phys. Letters, 34A, 209 (1971).
22. G. Deutscher and P. G. de Gennes Superconductivity Vol. II (Parks, Ed.) 1005 (1969).
- 23. John Clarke, Jour. de Phys., Supplement 2-3, Vol. 29, C2-3 (1968).

## Chapter 2

1. G. Deutscher and P. G. de Gennes, Superconductivity, Vol. II (Parks, Ed.) 1005 (1969).
2. John Clarke, Jour de Phys. 29, Supplement 2-3, C2-3 (1968).
3. C. A. Neugebauer, J. Appl. Phys. 35, 3599 (1964).
4. H. A. Notarys, unsolicited private communication.
5. J. D. Franson, private communication.

6. L. Young, Anodic Oxide Films, (Academic, London, 1961)

### Chapter 3

1. R. C. Jaklevic, J. J. Lambe, A. H. Silver, and J. E. Mercereau  
Phys. Rev. Letters, 12, 159 (1964).
2. R. C. Jaklevic, J. J. Lambe, A. H. Silver, and J. E. Mercereau  
Phys. Rev. Letters, 12, 274 (1964).
3. F. London, Superfluids, Vol. 1, New York, Wiley (1950).
4. R. P. Feynman, Lectures on Physics, Vol. III, Chapter 21, Addison-  
Wesley (1965).
5. J. E. Mercereau, Superconductivity, Vol. I, (Parks, Ed.), 393  
(1969).
6. John Clarke, Proc. IEEE 61, 8 (1973).
7. J. E. Mercereau, Rev. de Phys. Appl. 5, 13 (1970).
8. J. E. Zimmerman, Cryogenics 12, 19 (1972).
9. P. W. Anderson and A. H. Dayem, Phys. Rev. Letters, 13, 195 (1964).
10. J. E. Zimmerman and A. H. Silver, Phys. Rev. 141, 367 (1966).
11. R. K. Kirschman, H. A. Notarys, and J. E. Mercereau, Phys. Letters  
34A, 209 (1971).
12. H. A. Notarys, R. H. Wang, J. E. Mercereau, Special Issue IEEE  
Proc. 61, 79 (1973).

13. David William Palmer, Applied Superconductivity Conference, Paper E-1, Oakbrook, Ill. Sept. 30-Oct. 2, 1974.
14. John Clarke, Proc. IEEE, 61, 8 (1973).
15. John Clarke and J. L. Paterson, Appl. Phys. Letters, 19, 469 (1971).
16. D. L. Steuhm and C. W. Wilmsen, Appl. Phys. Letters, 20, 456 (1972).
17. T. A. Fulton, Solid State Commun. 8, 1353 (1970).
18. John Clarke, W. E. Tennant, and D. Woody, J. Appl. Phys. 42, 3859 (1971).
19. R. H. Wang, private communication.

#### Chapter 4

1. John Clarke, Revue de Phys. Appl. 9, (1974).
2. V. Ambegaokar and B. I. Halprin, Phys. Rev. Letters 22, 1364 (1969).
3. D. K. C. MacDonald, Noise and Fluctuations, Wiley, New York (1962).
4. F. Reif, Fundamentals of Statistical and Thermal Physics, Chapter 15, McGraw-Hill, New York (1965).
5. H. B. Callen and T. A. Welton, Phys. Rev. 83, 34 (1951).
6. M. J. Stephen, Phys. Rev. 182, 531 (1969).
7. D. Rogovin and D. J. Scalapino, Annals of Physics, 86, 1 (1974).
8. John Clarke and R. F. Voss, Phys. Rev. Letters, 33, 24 (1974).
9. John Clarke and G. Hawkins, Applied Superconductivity Conference, Paper R-3, Oakbrook, Ill., Sept. 30-Oct. 2, 1974.

10. A. Daym, A. Denestein, D. N. Langenberg, W. H. Parker, D. Rogovin, and D. J. Scalapino, *Phys. Rev. Letters* 22, 1416 (1969).
11. C. M. Faleo, W. H. Parker, S. E. Trullinger, and P. K. Hansma, *Phys. Rev.*
12. R. K. Kirschman and J. E. Mercereau, *Phys. Lett.* 35A, 177 (1971).
13. H. Kanter and F. L. Vernon, *Phys. Rev. Letters*, 25, 588 (1970).
14. S. Letzter and N. Webster, *IEEE Spectrum*, August 1970, p. 67.
15. D. E. Prober, *Rev. Sci. Instr.* 45, 848 (1974).
16. M. Simmonds and W. H. Parker, *Phys. Rev. Letters* 24, 876 (1970).
17. K. K. Likharev and V. K. Semenov, *JETP Lett.* 15, 442 (1972).
18. T. J. Reiger, D. J. Scalapino, and J. E. Mercereau, *Phys. Rev. B*, 6, 1734 (1972).
19. T. J. Reiger, D. J. Scalapino, and J. E. Mercereau, *Phys. Rev. Letters*, 27, 1787 (1971).
20. M. L. Yu, PhD Thesis, California Institute of Technology (1973).
21. M. L. Yu and J. E. Mercereau, Low Temperature Physics, LT-13 (Ed. by Temimerhaus, O'Sullivan, and Hammel) Vol. III, p. 799.
22. David William Palmer, Ph.D. Thesis, California Institute of Technology (1975).
23. A. A. Notarys, M. L. Yu, and J. E. Mercereau, *Phys. Rev. Letters* 30, 743 (1973).
24. L. G. Aslamazov and A. I. Larkin, *Pis'ma Zh. Eksp. Teor. Fiz.* 9 150 (1969) [*JETP Letters* 9, 87 (1969)].

Appendix A

1. K. K. Likharev and V. K. Semenov, JETP Letters 15, 442 (1972).